ΕΘΝΙΚΟ ΜΕΤΣΟΒΙΟ ΠΟΛΥΤΕΧΝΕΙΟ
ΣΧΟΛΗ ΜΗΧΑΝΟΛΟΓΩΝ ΜΗΧΑΝΙΚΩΝ
ΤΟΜΕΑΣ Μ.Κ. & Α.Ε.
Εργαστήριο Αυτομάτου Ελέγχου

Διπλωματική Εργασία

**Upper-limb Implant Prototype Miniaturization
Employing Biomechatronic EPP Control Topology**

**Ελαχιστοποίηση Μεγέθους Πρωτότυπου Εμφυτεύματος Άνω Άκρου
με Χρήση της Τοπολογίας Ελέγχου Βιομηχανοτρονικού EPP**

Παναγιώτης Πασπαλίδης

Επιβλέπων Καθηγητής: Ε. Γ. Παπαδόπουλος

ΑΘΗΝΑ 2023

Περίληψη

Η τεχνολογία των προσθετικών άνω άκρων έχει ως κύριο μέλημα τη βελτίωση της ποιότητας ζωής των ατόμων που έχουν υποστεί ακρωτηριασμό. Παρά τη σημαντική πρόοδο που έχει σημειωθεί τα τελευταία χρόνια, ο στόχος της δημιουργίας πλήρως λειτουργικών υποκατάστατων των φυσικών άκρων δεν έχει ακόμη επιτευχθεί. Το βασικότερο εμπόδιο στην προσπάθεια αυτή έγκειται στη δυσκολία παροχής ικανοποιητικής ανάδρασης στο χρήστη.

Η Εκτεταμένη Φυσιολογική Ιδιοδεκτικότητα (Extended Physiological Proprioception) αποτελεί μία τοπολογία ελέγχου προσθετικών άνω άκρων η οποία επικεντρώνεται στην επαναφορά της ιδιοδεκτικής ικανότητας του χρήστη. Μέσω σημάτων ανάδρασης προσφέρει τη δυνατότητα ασυναίσθητου ελέγχου θέσης του προσθετικού προσεγγίζοντας έτσι τη λειτουργία ενός φυσιολογικού άκρου. Παρ' όλα αυτά, η εφαρμογή της εν λόγω τοπολογίας ελέγχου συνοδεύεται από αρκετά μειονεκτήματα, μεταξύ των οποίων η ανάγκη χειρουργείου κινησιοπλαστικής και το αντιαισθητικό τελικό αποτέλεσμα λόγω της χρήσης ντιζών για την απευθείας μηχανική σύνδεση των μυών με το προσθετικό.

Η αναγνώριση της αξίας της ιδιοδεκτικής ανάδρασης σε συνδυασμό με την ανάγκη παράκαμψης των παραπάνω μειονεκτημάτων, οδήγησε στην πρόταση μίας νέας τοπολογίας ελέγχου ονόματι Biomechatronic EPP. Η προτεινόμενη τοπολογία είναι εμπνευσμένη από την κλασσική EPP μέθοδο και παράλληλα βασίζεται στην αρχιτεκτονική master-slave από τον τομέα της τηλερομποτικής και του τηλεχειρισμού. Πιο συγκεκριμένα, περιλαμβάνει την τοποθέτηση γραμμικών επενεργητών χαμηλής ισχύος σε σειρά με επιλεγμένους εναπομείναντες μύες του ακρωτηριασμένου κατά την αρχική χειρουργική επέμβαση ακρωτηριασμού. Τα εμφυτεύματα αυτά διαδραματίζουν το ρόλο των κύριων (master) ρομπότ και καταγράφουν εντολές δυνάμεων από τους μύες μέσω αισθητήρων δύναμης. Η πληροφορία αυτή αποστέλλεται ασύρματα στο προσθετικό άκρο που αποτελεί το ρομπότ υπηρέτη (slave), το οποίο και εκτελεί κατάλληλη κίνηση με βάση τις εντολές δύναμης που παραλαμβάνει. Τελικός στόχος είναι η γραμμική μετατόπιση των εναπομεινάντων μυών από τους γραμμικούς επενεργητές η οποία αντιστοιχεί στην κίνηση του προσθετικού άκρου. Με αυτόν τον τρόπο εξασφαλίζεται η δυναμική σύζευξη μεταξύ master και slave προσφέροντας ιδιοδεκτική ανάδραση στον χρήστη ανά πάσα χρονική στιγμή.

Στο πλαίσιο προηγούμενων εργασιών, για τη μελέτη της προτεινόμενης τοπολογίας ελέγχου, είχαν χρησιμοποιηθεί γραμμικοί επενεργητές master μεγάλων διαστάσεων. Σκοπός της παρούσας εργασίας ήταν ο επανασχεδιασμός των εμφυτευμάτων με κύριο γνώμονα την ελαχιστοποίηση διαστάσεων και ισχύος. Αντικείμενο της εργασίας ήταν ο προσδιορισμός των προδιαγραφών του μηχανισμού, η επιλογή των κατάλληλων εξαρτημάτων και εν τέλει η κατασκευή πρωτότυπου μηχανισμού εμφυτεύματος που θα μπορούσε να αξιοποιηθεί ως ρομπότ master για τη συγκεκριμένη εφαρμογή. Τέλος, πραγματοποιήθηκαν πειραματικές δοκιμές προκειμένου να διαπιστωθεί η επάρκεια των εξαρτημάτων του πρωτοτύπου και να διερευνηθούν ορισμένες από τις δυνατότητες που παρέχει η Biomechatronic EPP τοπολογία.

Τα συμπεράσματα που προέκυψαν από τις δοκιμές ήταν ότι παρά τις μικροσκοπικές τους διαστάσεις, οι νέοι γραμμικοί επενεργητές μπορούν να ανταπεξέλθουν στις απαιτήσεις της εφαρμογής. Παράλληλα, φαίνεται ότι η κατανάλωση ισχύος των πρωτοτύπων εμπίπτει στα επιθυμητά επίπεδα. Επιπλέον, τα αποτελέσματα υποδηλώνουν ότι η προτεινόμενη τοπολογία ελέγχου μπορεί να προσφέρει ικανοποιητική ανάδραση στο χρήστη σχετικά με τη θέση καθώς και με την αλληλεπίδραση του προσθετικού άκρου με το περιβάλλον. Τα παραπάνω, ενισχύουν την πεποίθηση ότι η Biomechatronic EPP τοπολογία μπορεί να έχει εφαρμοστεί στην πράξη και ότι είναι ικανή να ενεργοποιήσει την ιδιοδεκτική αισθητικότητα του χρήστη.

Abstract

Upper-limb prosthesis technology is primarily concerned with improving amputees' quality of life. However, despite significant progress in recent years, the aim of creating prostheses equipped with the complete functionality of a human limb has not yet been achieved. The main obstacle to this endeavour lies in providing adequate sensory feedback to the users.

Extended Physiological Proprioception (EPP) is an upper-limb control topology that focuses on restoring the proprioception of the user. Feedback signals enable the user to control the prosthesis position subconsciously, thus resembling the function of a normal limb. However, the implementation of this control topology is accompanied by several drawbacks, including the need for cineplasty surgery and the unaesthetic view of Bowden cables used for mechanically connecting the amputee's muscles to the prosthetic limb.

The paramount importance of proprioceptive feedback and the need to overcome the above shortcomings led to the proposal of a new control topology called Biomechatronic EPP. The proposed topology is inspired by the classical EPP method and is also based on the master-slave architecture from the field of Telerobotics and Teleoperation. More specifically, it involves the implantation and connection of low-power linear actuators with selected residual muscles of the amputee during the initial amputation surgery. These implants correspond to the master robots of the teleoperation scheme, and they measure forces exerted by the residual muscles via force sensors. This information is sent wirelessly to the prosthetic limb, which plays the role of the slave robot. Subsequently, the prosthetic performs a movement according to the received force commands. The final goal is the appropriate translational displacement of the residual muscles by the linear actuators, depending on the prosthetic limb's movement. This closed-loop control scheme ensures the dynamic coupling between master and slave, thus providing proprioceptive feedback to the user at all times.

In previous works, large-scale linear actuators have been used as master implants to study the proposed control topology. This thesis aimed to redesign the implants focusing mainly on minimizing their dimensions and power consumption. This involved determining the mechanism's specifications, selecting appropriate components, and ultimately, constructing an implant mechanism prototype that could be utilized as a master robot for this application. Finally, experimental tests were conducted to establish the adequacy of the prototype's components and to explore some of the possibilities provided by the Biomechatronic EPP topology.

The conclusions drawn from the tests were that despite their tiny dimensions, the new linear actuators could cope with the application's requirements. At the same time, it appears that the power consumption of the prototype falls within the desired specifications. Furthermore, the results suggest that the proposed control topology can provide satisfactory feedback to the user regarding the position as well as the interaction of the prosthetic limb with the environment. The above supports the belief that the Biomechatronic EPP topology can be realistically implemented and that it can activate the user's proprioceptive sensation.

Ευχαριστίες

Καταρχάς, θα ήθελα να ευχαριστήσω θερμά τον επιβλέποντα Καθηγητή Ευάγγελο Παπαδόπουλο, διευθυντή του Εργαστηρίου Αυτομάτου Ελέγχου της Σχολής Μηχανολόγων Μηχανικών του Εθνικού Μετσόβιου Πολυτεχνείου, για την πολύτιμη καθοδήγηση, προθυμία και υποστήριξη του καθ' όλη τη διάρκεια εκπόνησης της διπλωματικής εργασίας, καθώς και για την ευκαιρία που μου προσέφερε να αποκομίσω γνώσεις και εμπειρίες ως μέλος του Εργαστηρίου.

Επιπλέον, θα ήθελα να ευχαριστήσω το μεταδιδακτορικό ερευνητή Γεώργιο Μπέρτο για τη στήριξη και συνεισφορά του σε όλα τα στάδια της εργασίας.

Ακόμη, θα ήθελα να εκφράσω τις ευχαριστίες μου στα μέλη του εργαστηρίου Πέτρο Κωνσταντινέα, Νίκο Τουντουλίδη, Γιώργο Μπολανάκη και Γιάννη Νταβλιάκο για την άψογη και εποικοδομητική συνεργασία που είχαμε στα πλαίσια εκπόνησης της εργασίας.

Επιπρόσθετα, θα ήθελα να ευχαριστήσω τον κύριο Νικόλαο Μελισσά από το Τεχνικό Προσωπικό του Εργαστηρίου Τεχνολογίας και Κατεργασιών του ΕΜΠ, καθώς και τον ωρολογοποιό Σταμάτιο Καματσέλο για τη συνεισφορά τους στο κατασκευαστικό στάδιο της εργασίας.

Τέλος, θα ήθελα να ευχαριστήσω την οικογένεια μου και τους φίλους μου για την αμέριστη συμπαράστασή και την υπομονή τους καθ' όλη τη διάρκεια των σπουδών μου.

Αφιερώνεται στους γονείς μου, Ντίνο και Ελένη,
τον αδερφό μου, Χρίστο
και την κοπέλα μου, Λουίζα.

Table of Contents

List of Figures

List of Tables

1 Introduction

1.1 Purpose

Upper limb prosthesis control methods have progressed significantly in recent years. Nevertheless, human upper limb's complex anatomy and dexterity pose a challenging scientific task regarding its replacement. The mechanical demands and constraints of such an endeavour are considerable; however, the most crucial factor concerning the proper function of an upper limb is its control.

The human body can effortlessly control its upper limbs through a large number of sensory receptors located mainly in the muscles, joints and tendons. These sensors are called mechanoreceptors and are responsible for providing information to the neural system on any changes concerning the state of the upper limb. The ability to sense using these mechanoreceptors is called proprioception, and its absence renders the control of the limbs impossible.

In the field of prosthetics thus far, Myoelectric Control Systems have been the preferred control method, mainly due to their non-invasive nature. Such systems utilize electromyographic signals (EMG) detected by surface electrodes placed on the residual limb's skin to control the prosthesis. Myoelectric control constitutes an open loop velocity control configuration and visual feedback is the only feedback that informs the amputee regarding the state of the prosthesis. However, as demonstrated by Doubler, J.A.& Childress, D.S. (1984b) [5], velocity control has been proven to be inferior to position control in positioning tasks. In addition, as in many other prosthesis control methods, the lack of adequate feedback and more specifically of proprioceptive feedback, substantially limits the quality of prosthesis control.

The paramount importance of providing proprioceptive feedback through a closed-loop position control led D.C. Simpson, in 1974 [14], to be the first to suggest a novel prosthesis control approach known as Extended Physiological Proprioception (EPP). According to Simpson's proposal, Bowden cables would connect an amputee's residual muscles to the prosthetic. Through this physical mechanical link, information regarding the position, velocity, and forces could be transferred between the prosthetic device and the amputee's neural receptors, thus enabling the user's proprioception. However, the implementation of EPP also entailed certain negative aspects. Some of the drawbacks were that complex plastic surgery was required, which inherited future dangers regarding limb infections, while also the end result was not aesthetically pleasing to the human eye. In addition, this method often carried control constraints, mainly related to the direction of movement and the magnitude of the muscle's force capabilities.

Based on the EPP control notion and in an attempt to overcome the limitations mentioned above, since 2015 [10], [16], at the Control Systems Lab (NTUA), an innovative control proposal coined Biomechatronic Extended Physiological Proprioception (EPP) was introduced. This novel control topology aims to activate the proprioception of the amputee, and its architecture is based on the field of Telerobotics – Teleoperation. In particular, as shown in Figure 1-1, a master–slave control scheme is designed, employing an implantable device meant to be attached to the amputee's residual muscles and activate the receptors of the limb. The implant, which represents the master system in this configuration, is intended to

communicate wirelessly with the transradial prosthesis, which plays the role of the slave system. The main advantage of the proposed method is that it provides proprioceptive feedback to the amputee through the implantable device by implementing a closed-loop position control.
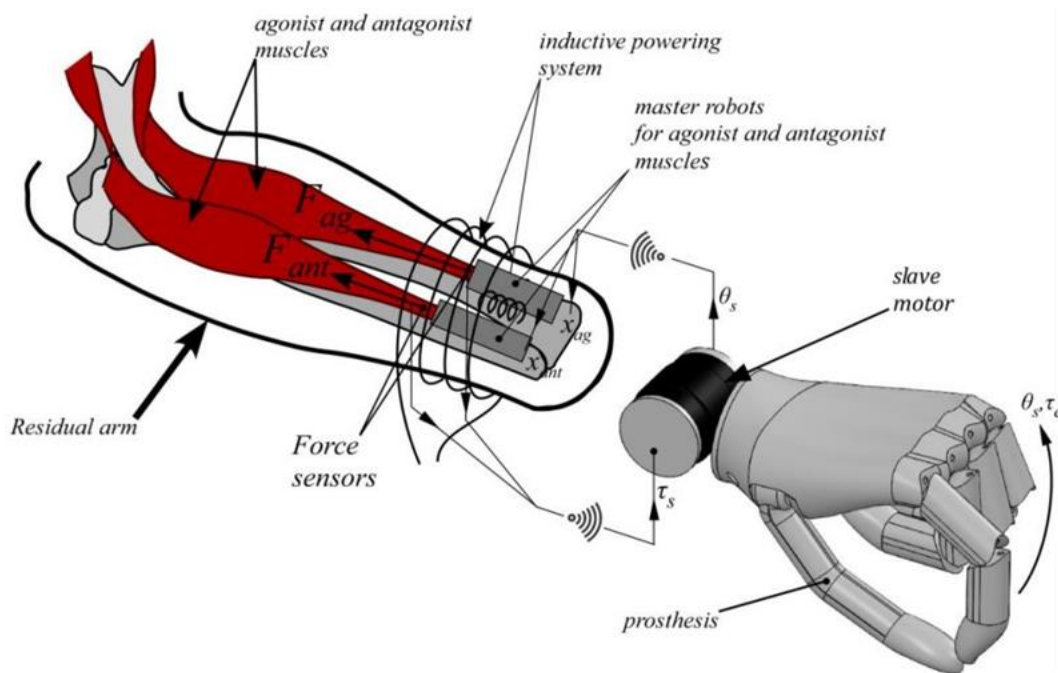
Figure 1-1.   Biomechatronic EPP Control Topology [10].

Six Diploma and MSc students have previously worked on this demanding project. The theoretical foundations of the proposed control topology were set by Mamblekos-Alexiou Anestis [10] and an initial large-scale experimental setup was constructed and examined by Vaggelatos Zaharias [15]. In addition, MSc students Koukoulas Nikolaos and Petros Konstantineas worked on the design and implementation of the wireless communication between the master and slave system [9], [7] while Spiros Kontogiannopoulos experimentally compared the control performance of Biomechatronic EPP to other control topologies, including EMG [8].

The results of the above extensive previous work suggested that the proposed method is able to compete with commonly used upper-limb control methods and even surpass them [8]. However, even though these results indicated that the concept of Biomechatronic EPP is definitely promising, the experiments were performed using a large-scale implant prototype.

Therefore, the next step was to design and construct a miniature version of the implantable system that could realistically fit inside a human amputated arm. This led to the purpose and work of the current Diploma Thesis. More specifically, this thesis focuses on creating the smallest possible implant prototype mechanism in terms of dimensions and power consumption that simultaneously fulfils the specifications defined by the Biomechatronic EPP configuration in order to achieve the desired level of prostheses control. The end goal is to examine if the miniaturized implant prototype can provide satisfactory results and, therefore, not only give rise to the concept of Biomechatronic EPP but also demonstrate that it can be practically implemented.

1.2 Literature Review

The desirable characteristics of upper limb prostheses control systems were listed by Childress D.S. in 1992 [4] as follows:

1. Low mental loading or subconscious control.
2. User-friendly or simple to learn to use.
3. Independence in multifunctional control.
4. Simultaneous, coordinated control of multiple functions.
5. Direct access and instantaneous response.
6. No sacrifice of human functional ability.
7. Natural appearance.

Considering all the above, it is evident that a prosthetic system must provide the user with the sensation of a normal upper limb, thus creating the impression that the prosthetic is an extension of the amputated body rather than a foreign apparatus. The most crucial factor in achieving the above desirable attributes, is the choice of the prostheses control configuration.

1.2.1 Body-powered systems and Extended Physiological Proprioception (EPP)

Body-powered systems constitute a type of prosthesis for patients with upper limb amputation. Their distinguishable trait among other types of prostheses is that they require muscular effort by the amputee to operate the prosthetic limb.

Extended Physiological Proprioception (EPP) is a control topology that belongs to the family of body-powered prostheses. In the case of EPP, control is achieved by the use of Bowden cables, serving as a mechanical connection between the amputees' remaining muscles and the prosthetic limb. This configuration allows the user to be subconsciously aware of the prosthetic's state, thus enabling the amputee's proprioceptive ability. The core concept of EPP constitutes the basis of the proposed Biomechatronic EPP control topology presented in this thesis.
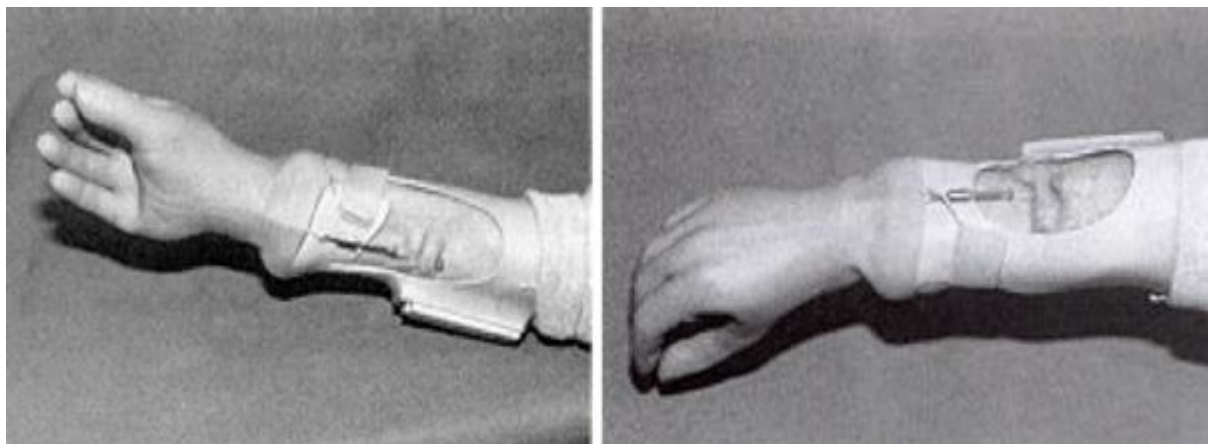
Figure 1-2. EPP body-powered prosthesis - Modified Otto-Bock hand to be driven by exteriorized tendons built at Northwestern University Prosthetics Research Laboratory [1].

1.2.2 Teleoperation - Telerobotics

Teleoperation refers to the control of a machine or an actuator that is located in a distant area. A system based on the principles of Teleoperation generally consists of the following:

•A master device that is controlled by the user.

•A slave device whose function depends on the commands given by the master device.

•A controller responsible for the dynamic correlation between the master and the slave devices by transferring the appropriate information concerning their displacement and applied forces.

It has to be noted that the degrees of freedom of both the master and the slave devices must be the same. This topology is considered a successful one if the impedance of the environment is the same for the user as if he or she was controlling the slave motor without the master. In this case, the control system is called transparent [19], [15].

1.3   Thesis Structure

The present thesis is structured as follows.

In the first chapter, the purpose of the Diploma Thesis and a brief literature review are presented.

The second chapter presents the design process of the proposed miniaturized implant prototype, laying out the specifications and the final design of the implant's mechanism.

In the third chapter, the selection and assembly process of the hardware components from which the master system consists is thoroughly explained. This chapter also gives detailed information on the experimental setup, including the FSR Circuit and the slave system.

The fourth chapter describes the procedure for identifying the master system parameters. It also includes the design of the implemented control scheme, used to control both the master and the slave system.

The fifth chapter illustrates the implementation stage and how the communication between the master and slave system was achieved using the dSPACE platform DS1103. This chapter also includes the complete hardware connection map.

In the sixth chapter, the setup utilized to perform the experimental tests is displayed. Two experiments concerning the verification of the transparency of the proposed configuration and the adequacy of the selected hardware components are presented and discussed. Moreover, in an attempt to examine the capabilities of the Biomechatronic EPP control topology, two additional experiments are presented, namely target and sense experiments.

The seventh chapter summarizes the conclusions of this thesis and includes recommendations for the next steps in future work.

Appendix A presents the datasheets of all the hardware components used for the setup.

2   Implant Prototype Design

2.1   Introduction

This chapter presents the selection and design process of the linear motion mechanism that will eventually be part of the miniaturized implantable device (master system). In the end, the final design proposal will be displayed and compared to the existing large-scale solution used in previous works.

First of all, to fully comprehend the decision process regarding the linear motion mechanism selection, the main functions that the implant (master system) is expected to perform should be explained.

As mentioned before, the implantable device or master system (these two terms will be used interchangeably throughout the thesis) is intended to be permanently attached to a remaining pair of agonist and antagonist muscles, as shown in Figure 1-1. This establishes a mechanical linkage between the amputee's mechanoreceptors and the implantable device. Each connection to a muscle pair enables the user to control and receive proprioceptive feedback regarding one corresponding degree of freedom of the prosthetic. In this work, a specific scenario is examined, under which the implantable device is connected to a pair of agonist and antagonist muscles, with the corresponding degree of freedom being the flexion/extension of the wrist (see Figure 2-1). This degree of freedom refers to the movement capability of the prosthetic, which plays the role of the slave robot in the Biomechatronic EPP configuration.

It has to be noted that the selected degree of freedom could have represented a different motion of a human upper limb, for example, a grasping motion. However, this does not affect the implant's operation in any way, and consequently, for purposes of simplicity, it was decided that the rotation of the wrist should be examined.
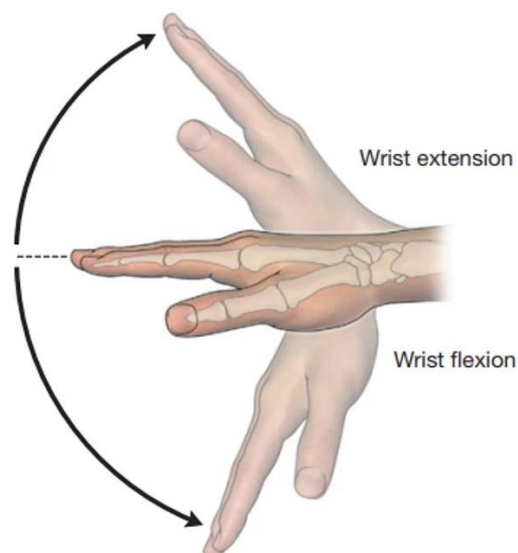
Figure 2-1.   Wrist flexion and extension [13].

The next thing that must be clarified is why a linear motion mechanism is required in the first place. The answer has to do with the working principles of the agonist and antagonist muscle pairs.

In the human body, skeletal muscles work together by contracting or relaxing in order to move a joint. This could be illustrated by a simplified example, visualized in Figure 2-2. Human joints are connected to antagonistic muscle pairs; in the case of the elbow joint, to the biceps and triceps. If a person wants to perform, for example, a flexion of the elbow joint, the biceps (agonist) contract while the triceps (antagonist) relax to allow the desired motion to be accomplished (Figure 2-2 (a)). Reversely, in the case of the elbow extension, the two muscles exchange roles, with the triceps (agonist) having to contract while the biceps (antagonist) enter a relaxing state (Figure 2-2 (b)).
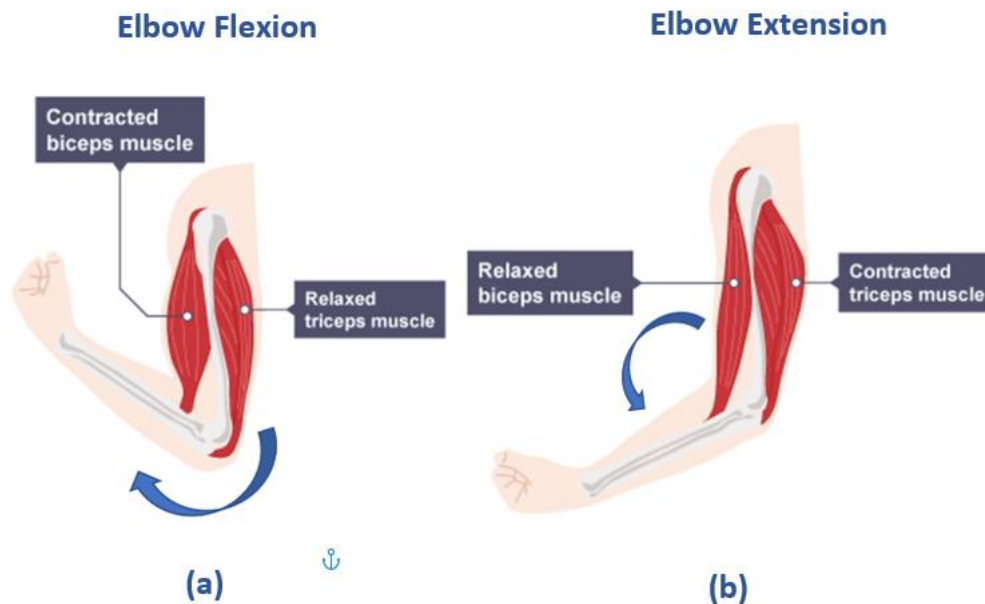
Figure 2-2.   Elbow Joint Motion (a) Elbow Flexion (b) Elbow Extension (Modified from [3]).

It has to be noted that the above constitutes a simplified explanation that provides the core idea behind the motion mechanics of joint motion in the human body and not an in-depth detailed description of how a real elbow joint works. The critical thing to remember is that to move a joint, a displacement (change of length) of the corresponding muscles is observed. More specifically, during contraction, muscles shrink, thus reducing their overall length, while during relaxation, muscles lengthen.

In the case of customary upper limb amputation, after the surgery, amputees are often still able to exert forces through their remaining muscles; however, these are no longer connected to a movable joint. This unutilized opportunity is precisely what the Biomechatronic EPP control topology seeks to take advantage of through the placement of the implantable device. The contraction and extension of the muscles that an upper limb could normally perform can be artificially achieved through the help of the implantable device.

The proposed implant mainly consists of two linear actuators, and each one would be separately connected to an agonist and an antagonist remaining muscle of the amputee (see Figure 2-3). With the help of the linear motion mechanisms, the implant is able to linearly displace the muscles, thus replicating the normal function of a human joint.
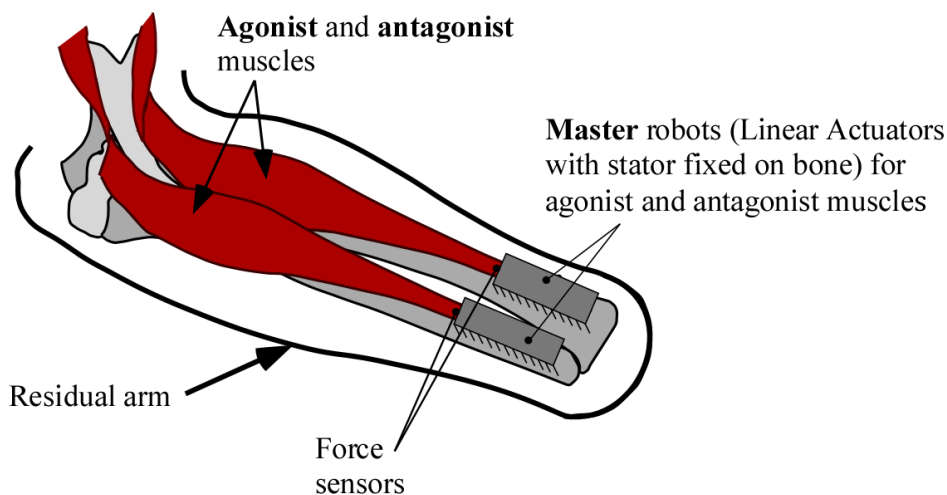
Figure 2-3. **Master System: Linear Actuators attached to the agonist and antagonist muscles.**

More specifically, the working principle of the Biomechatronic EPP configuration is as follows (see Figure 2-4): First, the amputee exerts forces through the muscles attached to the implant. These forces are measured by force sensors located between the muscles and the master robots and are used as input for the motion of the prosthesis. This is achieved by wirelessly transmitting the force measurements from the implant's microcontroller (master) to the microcontroller of the prosthesis (slave). Subsequently, the prosthetic performs a motion that corresponds to the input measurements. Then, the angular position of the prosthetic is transmitted back to the implant, which translates the information to the linear position and velocity that the muscles of interest should have in the case that the muscles were mechanically linked to the prosthetic limb. The displacement of the muscles is then accomplished through the actuation of the linear motion mechanisms for the agonist and antagonist muscles respectively. This closed-loop position control process is continuously repeated as long as the amputee exerts forces indicating the intention to move the prosthetic. This way, Biomechatronic EPP establishes an inextricable correlation of force, velocity and position between the prosthetic limb and the muscles of the amputee, thus providing the desired proprioceptive feedback.
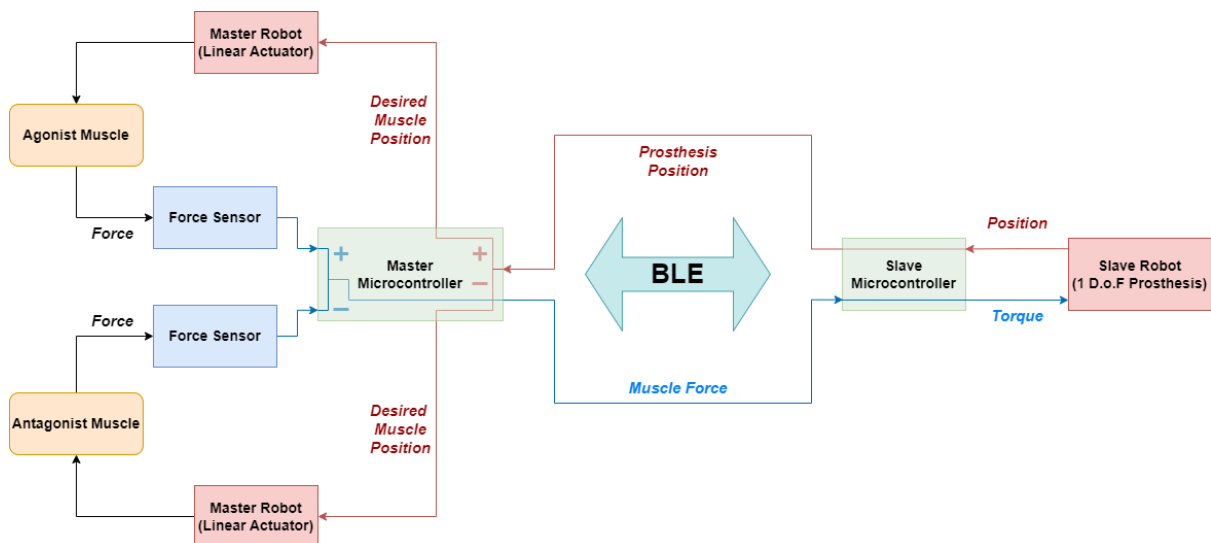
Figure 2-4. **Biomechatronic EPP Control Topology Architecture.**

2.2 Linear Motion Mechanism Selection Process

Now that the purpose and primary functions of the implant are explained, the linear motion mechanism selection process is presented.

In previous works [10], the linear motion was achieved using a linear actuator setup (see Figure 2-5). As can be seen from the Solidworks assembly in the figure, in that configuration, two lead screws (one for the agonist and one for the antagonist muscle) are placed in series with their respective master motors. Figure 2-6 displays the actual experimental setup used in the lab next to a human forearm for comparison purposes. The maximum dimensions of each linear actuator system (excluding the force sensor housing) were 132.9 mm in length, 33.3 mm wide, and 19.8 mm in height. It is evident that these dimensions are prohibitive in terms of fitting inside a human arm that has undergone transradial amputation surgery.
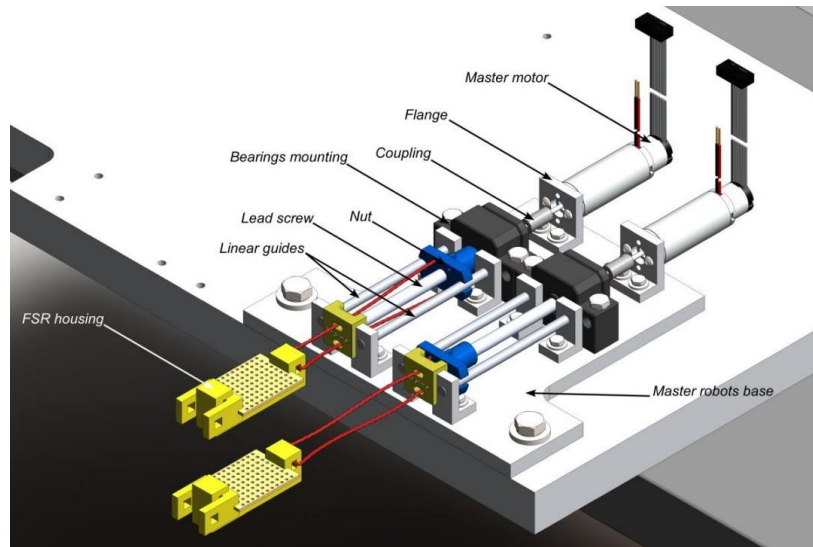
Figure 2-5.   Solidworks Assembly of the previous Master System.
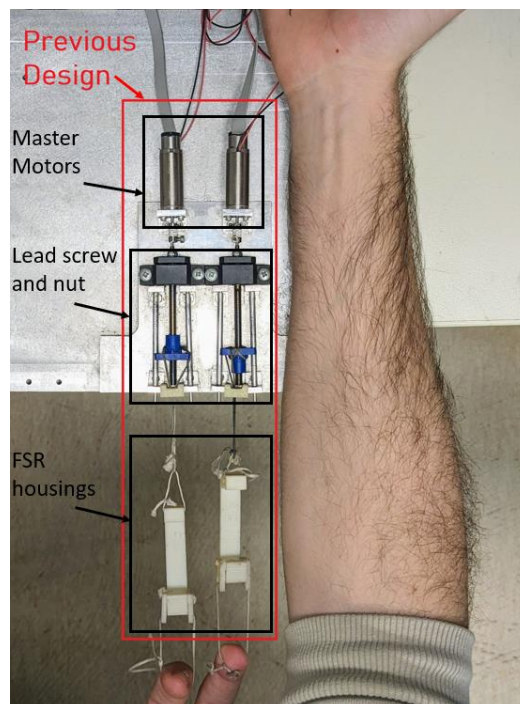
Figure 2-6.   Previous Master System next to a human forearm.

Therefore, as is the purpose of this thesis, a new, miniaturized linear actuator configuration had to be designed to support the idea that the Biomechatronic EPP can be realistically implemented.

For this reason, various types of linear motion mechanisms were considered and examined based on design constraints and specifications. Specifications of hardware components such as the required torque and angular velocity of the master motors or the energy consumption limit, will be thoroughly examined in the next chapter. This chapter will only focus on the main criteria that contributed to determining the *type* of the selected linear motion mechanism and the configuration of the final design. Those criteria are presented next.

2.2.1   Dimensions / Volume distribution

The anatomy of the antebrachium is highly complex and cannot be accurately described by simple geometric shapes, as shown in Figure 2-7. As a result, the exact dimension limitations were difficult to be determined since no precedent-related research was found. Therefore, it was decided to set a dimensional boundary of 40x20x20 mm, which was based on the smallest estimated linear motion mechanism that could realistically be designed and constructed in the lab, while simultaneously fulfilling all other specifications. This dimensional restriction concerns each linear motion mechanism, and the implant requires two. Figure 2-8 illustrates a human forearm next to a 3D-printed rectangular box with the exact dimensions of the dimensional boundary.
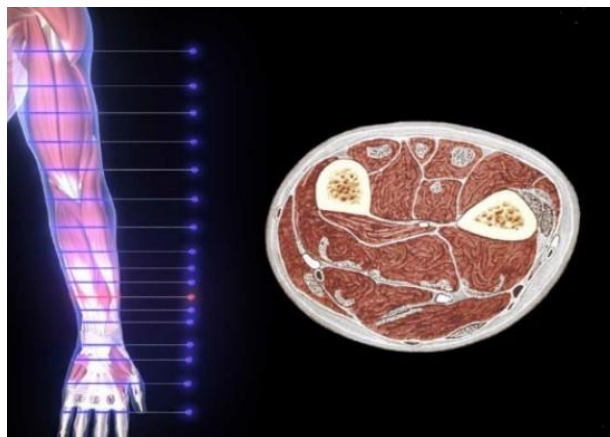
Figure 2-7.   Cross Section of Antebrachium [11].
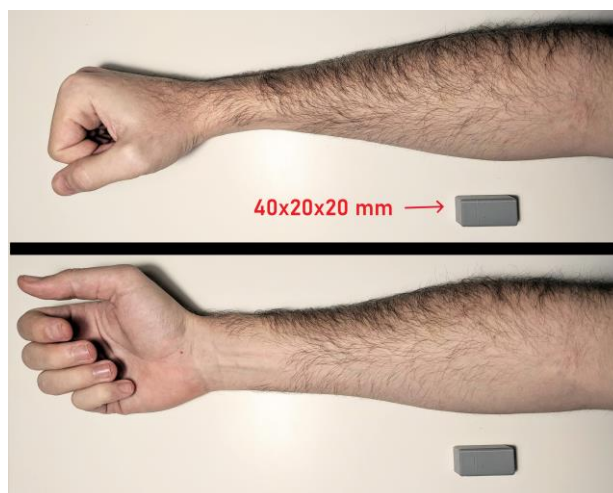
Figure 2-8.   3D-printed box with maximum dimensions next to a human forearm.

2.2.2 Non-backdrivability

This feature was one of the most crucial specifications for finalizing the mechanism selection process. A transmission mechanism is considered *non-backdrivable* when motion can be transmitted only from the input to the output axis and not vice-versa [6]. This means that the linear actuator should be driven only by the actuation of the mechanism's motor (input) and not by the forces exerted on it by the amputees' muscles (output).

From [1], it is given that muscle cineplasty and exteriorized tendons amputees were able to produce a maximum force between 0.6–2.5 kg, which roughly translates to 5.9–24.5 N. During the prosthesis operation, there are some cases in which the mechanical system should oppose the movement of the muscle; for example, when the prosthetic comes in contact with an object from the environment. Previous works indicated that the miniaturized components used in this application could not directly match the power of the muscle. This issue was overcomed by ensuring that the linear motion mechanism would be non-backdrivable. The significance of this non-backdrivable characteristic will become apparent in the following chapters and especially during the sense experiment, where it played a decisive role in the outcome. Since many linear motion mechanisms are backdrivable, this essential feature narrowed the range of possible options considerably.

2.2.3 Durability

The mechanical system will be attached to the muscles, and it will be regularly subjected to dynamic loading. This means that the system should be durable enough to withstand the forces exerted on it daily for a lifespan of many years.

2.2.4 Cost and lead time

There was no specific cost or time limitation set. However, the general approach was to look for off-the-shelf components rather than custom-made ones since this would prove costly and time ineffective.

2.2.5 Linear Motion Mechanism Types

Considering all of the above criteria, the two main contender types of linear motion mechanisms were the lead screw (see Figure 2-9) and the worm gear (see Figure 2-10). These two options are also the preferred choices for miniature linear actuators, especially in the field of prosthetics. Other options, such as rack and pinion mechanisms, bevel gears, or various pulley configurations, were mainly eliminated due to the fact that, in general, they constitute backdrivable mechanisms.

Unfortunately, after conducting an extensive market search, neither off-the-shelf lead screw nor worm gear linear actuators were able to meet all the specifications required for the application in question. Consequently, it was decided that the mechanism should be designed and constructed in the lab from scratch.
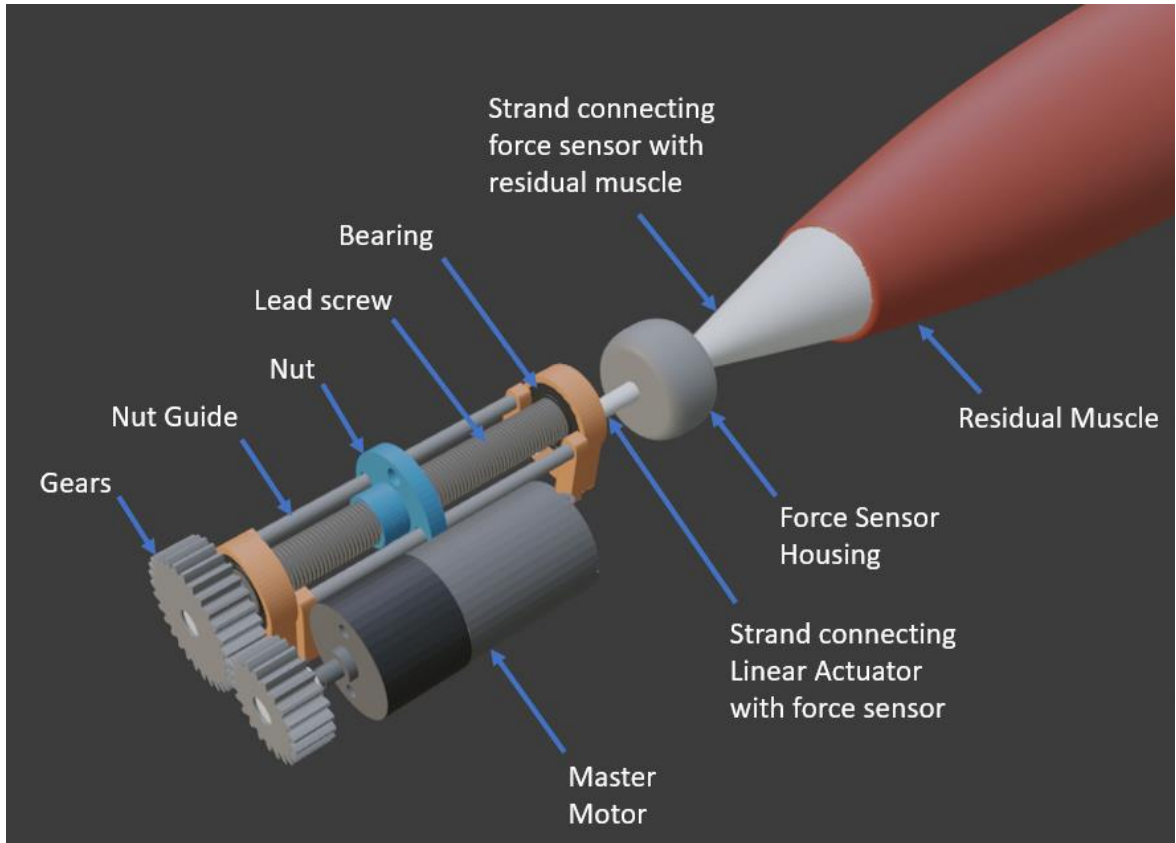
Figure 2-9.   Initial conceptual design of a lead screw mechanism made in Blender.
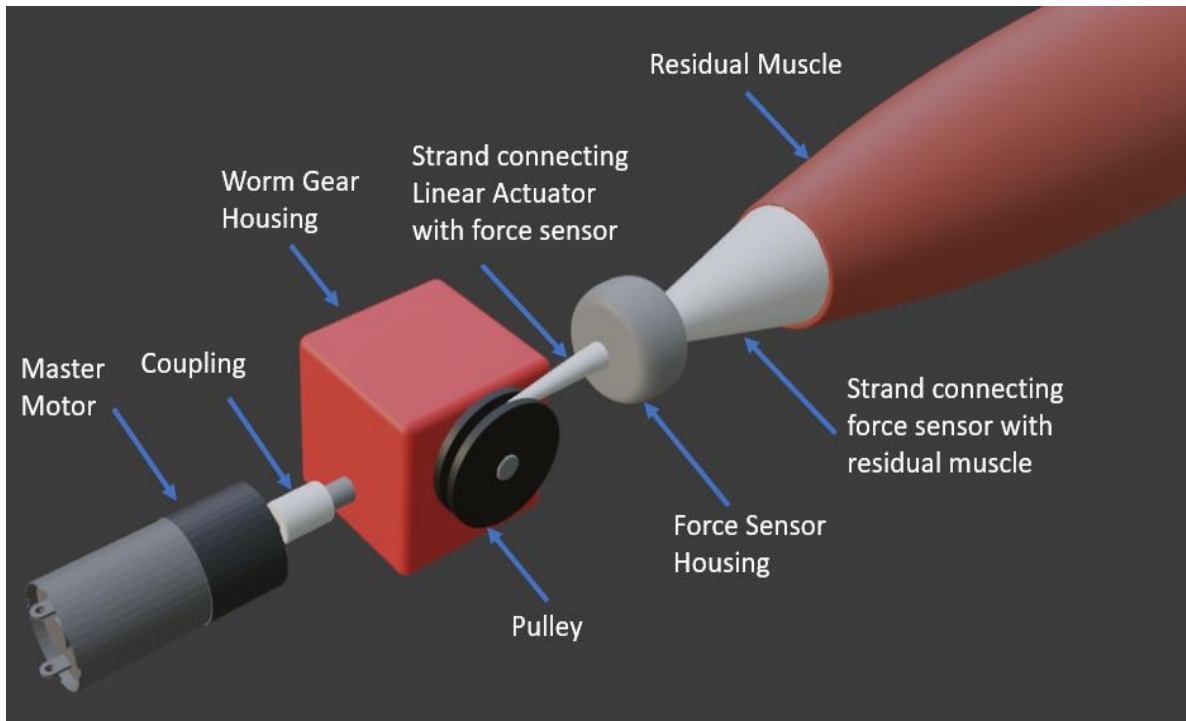
Figure 2-10. Initial conceptual design of a worm gear mechanism made in Blender (based on the miniature worm gear reducers of ondrives.us [20]).

After much consideration, it was concluded that the creation of a lead screw mechanism would prove to be a more feasible endeavour compared to the worm gear. The simple

assembly process and the plethora of available individual parts regarding lead screw mechanisms would enable the fine-tuning of several parameters in order to achieve the desired characteristics. The final design proposal is presented in the following section.

2.3   Final Design

Figure 2-11 presents the configuration of the linear motion mechanism intended to be embedded in the implantable device.
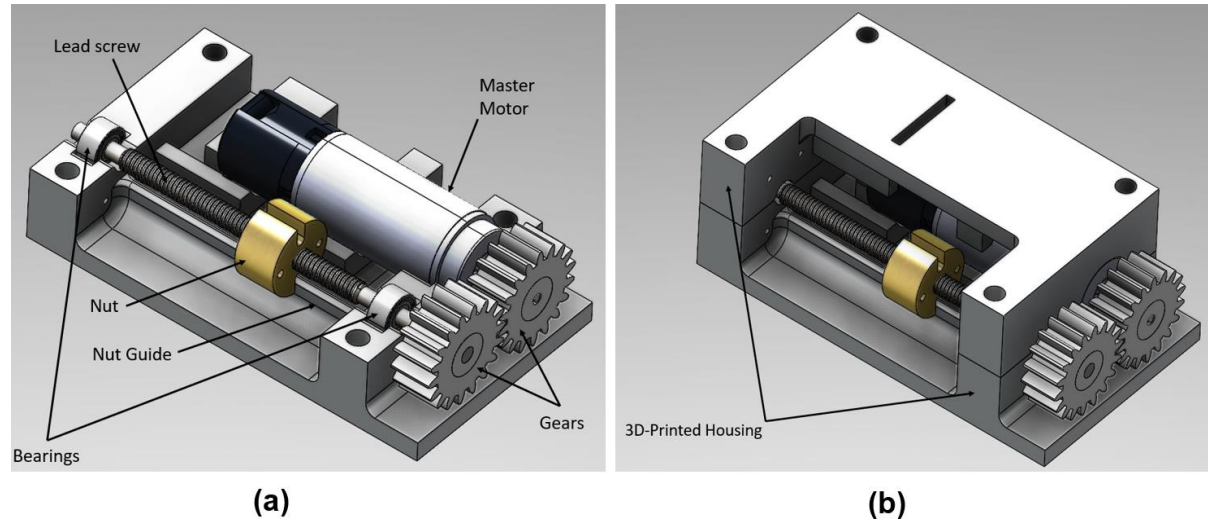
Figure 2-11. Master System Linear Actuator Final Design – Solidworks Assembly.

The total dimensions of the structure are 39x21x15 mm which was considered satisfactory based on the dimensional restrictions. The proposed mechanism consists of a motor, two gears, a lead screw with a nut, and two bearings. All of those mechanical components have miniature dimensions, and in the next chapter, the selection procedure for each part will be presented in detail.

It must be clarified that Figure 2-11 presents the linear motion mechanism proposal that will be used in the experimental setup in lab conditions, to examine the adequacy of the selected mechanical components, and not a complete proposal intended to be used as the actual implant. The latter can be part of a separate Thesis where a hermetically sealed enclosure for the whole implant setup (including the linear mechanism, the microcontroller, the rechargeable battery, the FSRs etc.) will be designed and examined for biocompatibility.

The holes in the 3D-printed housing and its rectangular shape facilitate the mounting of the structure on the base of the experimental setup, while the various uncovered places in the housing structure ease the optical observation of the mechanism operation during the experiments.

Figure 2-12 and Figure 2-13 show the two master linear actuators as they were mounted in the experimental setup, while Figure 2-14 and Figure 2-15 offer a clearer view of the parts inside the housings.
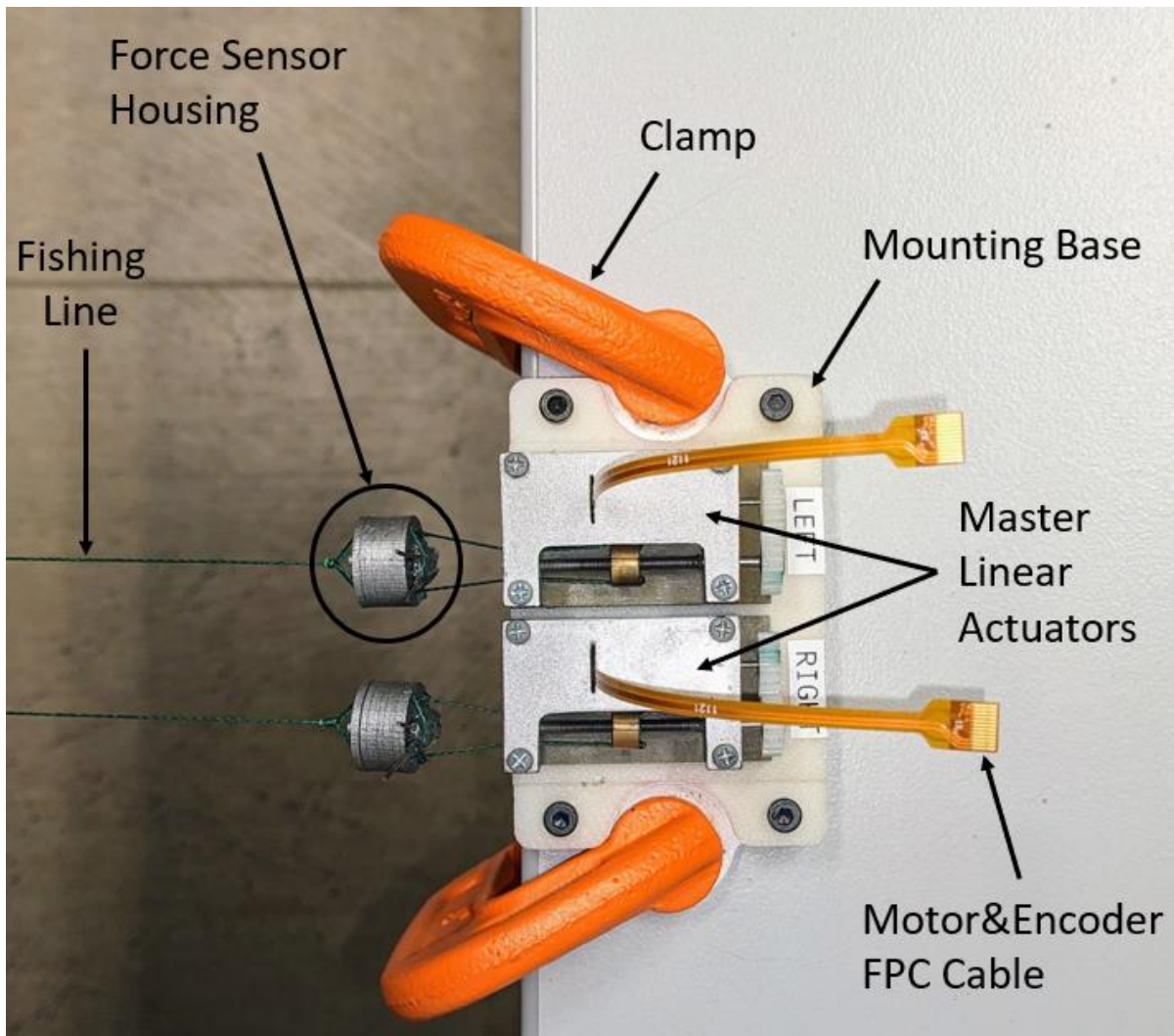
Figure 2-12. New master system that was constructed in the lab (top view).
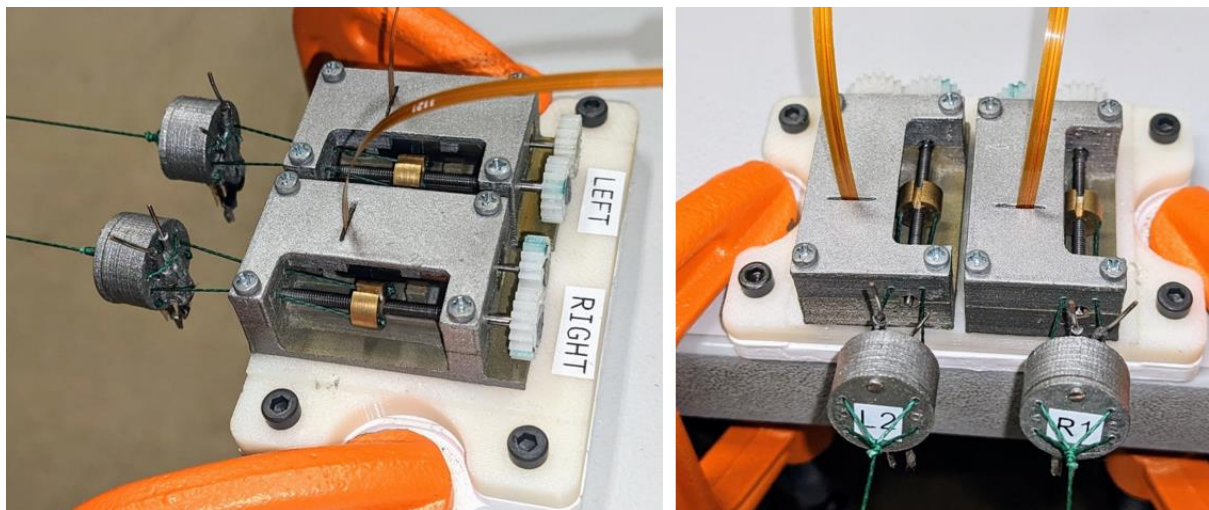
Figure 2-13. New master system that was constructed in the lab (close up).
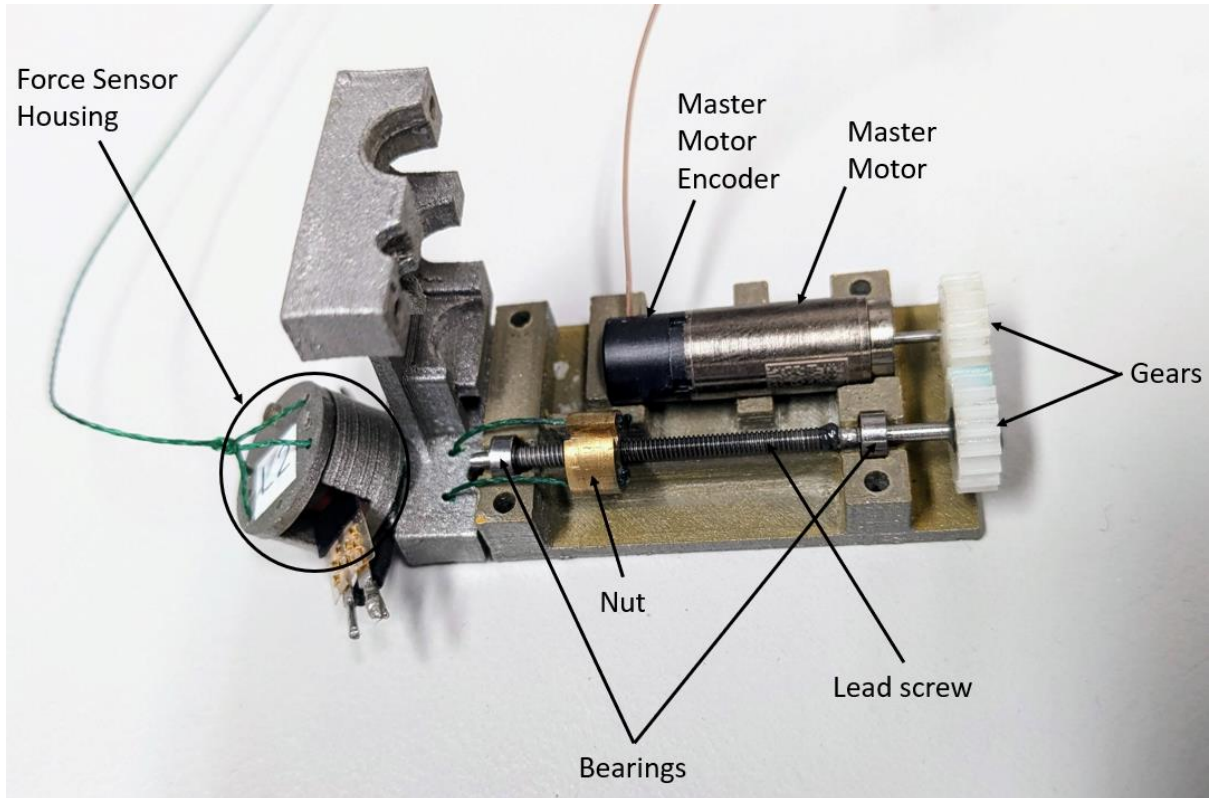
Figure 2-14. New master system with semi-opened housing revealing parts inside (side view).
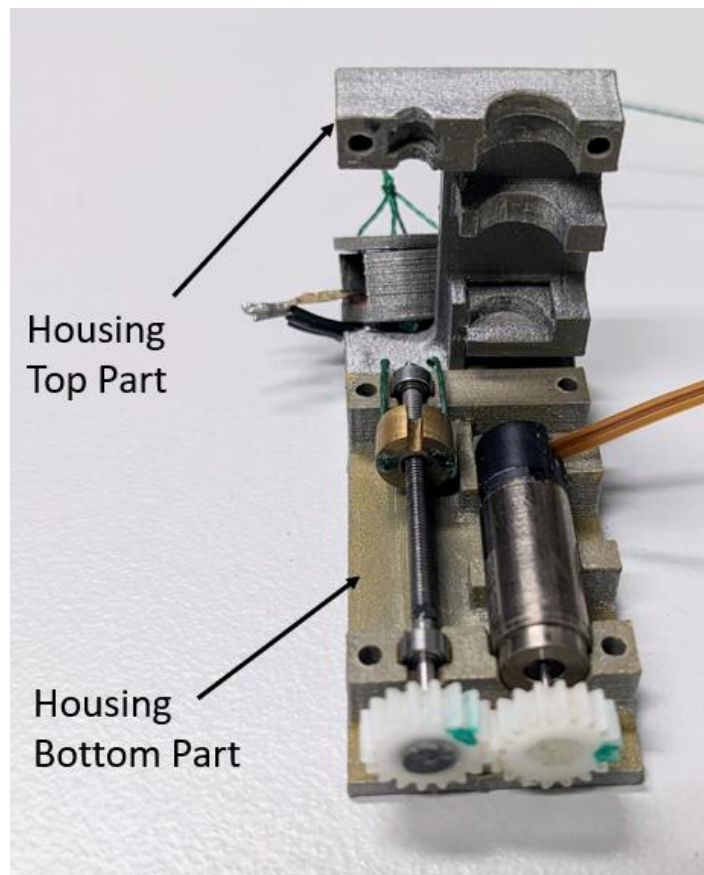
Figure 2-15. New master system with semi-opened housing revealing parts inside (front view).

To put matters in perspective, the previous and the new master systems are compared side by side.
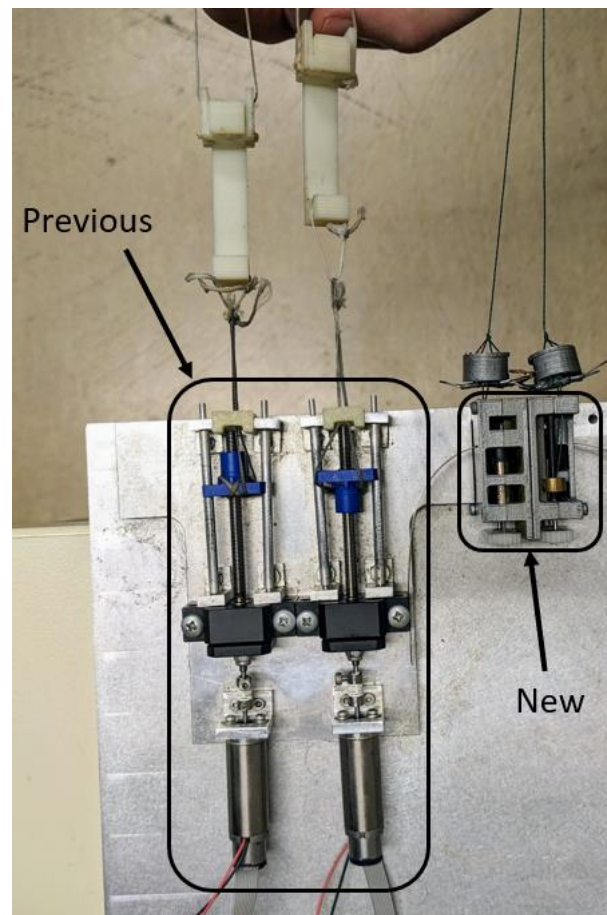
Figure 2-16. Previous and New linear actuators of the master system side by side.

Figure 2-16 illustrates the reduction achieved in terms of dimensions compared to the linear actuator of the master devices that were used in previous works.

More precisely, an 85.9% reduction in volume was accomplished. Moreover, the overall volume distribution was improved by placing the lead screw and the master motor in a parallel configuration instead of an in-series configuration that was used in the previous setup. This reduces the length of the overall implant, which would prove essential in the case of fitting inside an amputated forearm.

In addition, the new master system weighs significantly less. Specifically, the mechanical components comprising each of the new master mechanisms add up to just 11 g (this includes the motor, encoder, lead screw, nut and bearings). This is an enormous improvement compared to the previous system, where each mechanism weighed beyond 100 g.

Lastly, the selection of smaller master motors led to a considerable decrease in power consumption. Unfortunately, no power consumption measurements were taken with the previous setup to directly compare the two systems in question. However, it can be stated that the previous system was equipped with a master motor with a power rating of around 3 W, while the new system employs motors rated at 0.5 W. More details about the matter will be presented in Chapter 6 since, during the experimental phase of this thesis, a power consumption test was conducted to obtain the estimated consumption of the new system.

3   Hardware Selection

3.1   Master System - Mechanical Parts Selection Process

This chapter describes the selection process of each of the mechanical components that comprise the proposed master linear actuator which was presented in the previous chapter.

3.1.1   Modelling

The hardware selection procedure begins with the modelling of the linear actuator. A theoretical model of the mechanism is necessary to estimate the required torque and angular velocity of the master motor and the geometric characteristics that each of the other components should have.

Firstly, the mathematical symbols used in the equations to follow must be explained. In Figure 3-1 the mechanical parts of the master system are identified.
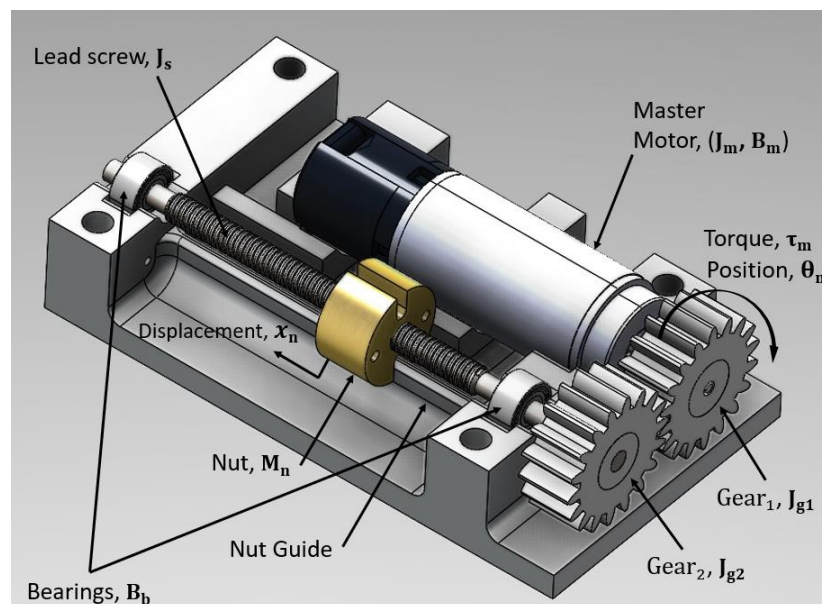
Figure 3-1.   Linear Actuator Components Notation.

The symbols displayed in Figure 3-1 are explained in Table 3-1.

Table 3-1.   Symbol description for Figure 3-1.

Description	Symbol	Unit
Inertia of the motor	J_m	$kg m^2$
Inertia of the gear attached to the motor	J_{g1}	$kg m^2$
Inertia of the gear attached to the lead screw	J_{g2}	$kg m^2$
Inertia of the screw	J_s	$kg m^2$
Damping of the motor	B_m	$kg m^2 s^{-1}$
Damping of the bearings	B_b	$kg m^2 s^{-1}$
Mass of the nut	M_n	kg
Gear ratio	n	$-$
Torque of the motor	τ_m	Nm
Angular position of the motor	θ_m	rad
Linear displacement of the nut	x_n	m

Further details regarding the lead screw geometry are displayed in Figure 3-2.

(a)   (b)
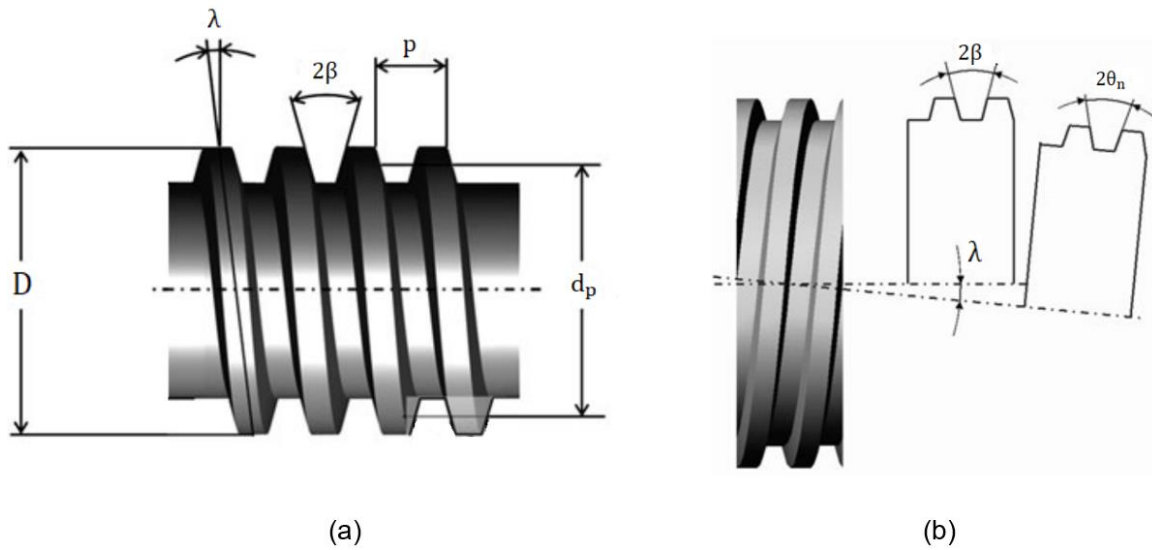
Figure 3-2.   Lead Screw Notation – Modified from [12].

The descriptions of the mathematical notations seen in Figure 3-2 are given in Table 3-2. Next, the equations that correlate the quantities of interest are presented.

Table 3-2.   Symbol description for Figure 3-2.

Description	Symbol	Unit
Pitch of the lead screw	p	m
Number of thread starts	n_s	–
Lead of the lead screw	l	m
Major diameter of the thread	D	m
Pitch diameter of the screw	d_p	m
Thread angle as measured on a section through the axis of a screw	β	deg
Lead angle (or helix angle)	λ	deg
Thread angle as measured on a section perpendicular to the helix	θ_n	deg

From theory, it is known that the lead l of the screw is defined as

$$l = n_s p \qquad (3\text{-}1)$$

where p is the screw pitch (distance between identical points of two consecutive threads) and n_s is the number of starts [12]. In the current project, n_s is equal to 1 and therefore the lead is the same as the pitch of the screw.

The lead angle λ, is defined as

$$\tan \lambda = \frac{l}{\pi d_p} = \frac{p}{\pi d_p} \qquad (3\text{-}2)$$

where, as stated in [12], the pitch diameter d_p can be obtained approximately by

$$d_p = D - \left(\frac{p}{2} \right) \qquad (3\text{-}3)$$

Lastly, the thread angle θ_n can be calculated from the following equation.

$$\theta_n = \arctan\left(\tan\beta\cos\lambda\right)$$
(3-4)

A lead screw mechanism is generally examined by unwrapping a lead screw and a nut thread on a flat surface, as shown in Figure 3-3. Nevertheless, it is crucial to comprehend that depending on the direction of the nut's velocity and the direction of the exerted force by the residual muscle, two distinct loading cases are observed.

Loading Case 1: The force F_{mu} exerted by the muscles of the amputee has the same direction as the velocity of the nut $\dot{x}_n$. The forces developed in this scenario are illustrated in Figure 3-3.
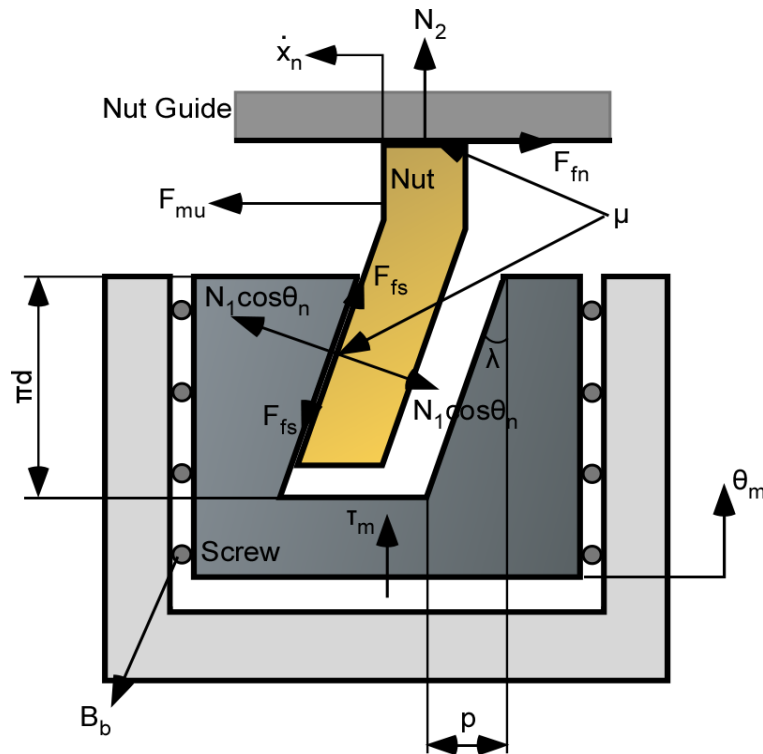
Figure 3-3.   Loading Case (1) Modified from [10].

The symbols shown in Figure 3-3 are described in Table 3-3.

Table 3-3.   Symbol description for Figure 3-3.

Description	Symbol	Unit
Coefficient of friction	μ	–
Perpendicular force generated due to the contact between the nut and screw	N_1	N
Perpendicular force generated due to the contact between the nut and guide	N_2	N
Friction force between nut and guide	F_{fs}	N
Friction force between nut and screw	F_{fn}	N
Muscle force	F_{mu}	N
Linear velocity of the nut	$\dot{x}_n$	m/s

From Figure 3-3, the following equations concerning the friction forces can easily arise.

$$F_{fs} = \mu N_1 \tag{3-5}$$

$$F_{fn} = \mu N_2 = \mu \left(F_{fs} \cos \lambda - N_1 \cos \theta_n \sin \lambda \right) \tag{3-6}$$

Consequently, the *screw* dynamics can be expressed through Equation (3-7).

$$J_{eq} \ddot{\theta}_m + B_{eq} \dot{\theta}_m = \tau_m + \frac{d_p}{2} N_1 \left(\cos \theta_n \sin \lambda - \mu \cos \lambda \right) \frac{1}{n} \tag{3-7}$$

where the equivalent moment of inertia J_{eq} is given by

$$J_{eq} = J_m + J_{g1} + (J_s + J_{g2}) \frac{1}{n^2} \tag{3-8}$$

and the equivalent viscous friction coefficient B_{eq} by

$$B_{eq} = B_m + B_b \frac{1}{n^2} \tag{3-9}$$

On the other hand, the equation that describes the dynamic behaviour of the *nut* is the following:

$$M_n \ddot{x}_n = F_{mu} - \mu N_1 \left(\mu \cos \lambda - \cos \theta_n \sin \lambda \right) - N_1 \left(\cos \theta_n \cos \lambda + \mu \sin \lambda \right) \tag{3-10}$$

Dividing Equations (3-10) and (3-7), the dynamics of the linear actuator system can arise

$$\frac{M_n \ddot{x}_n - F_{mu}}{J_{eq} \ddot{\theta}_m + B_{eq} \dot{\theta}_m - \tau_m} = \frac{-\mu \cancel{N_1} \left(\mu \cos \lambda - \cos \theta_n \sin \lambda \right) - \cancel{N_1} \left(\cos \theta_n \cos \lambda + \mu \sin \lambda \right)}{-\frac{d_p}{2} \cancel{N_1} \left(\mu \cos \lambda - \cos \theta_n \sin \lambda \right) \frac{1}{n}} => \tag{3-11}$$

$$\frac{M_n \ddot{x}_n - F_{mu}}{J_{eq} \ddot{\theta}_m + B_{eq} \dot{\theta}_m - \tau_m} = \frac{\mu}{\dfrac{d_p}{2} \dfrac{1}{n}} + \frac{1}{\dfrac{d_p}{2} \dfrac{1}{n} \xi_1} => \tag{3-12}$$

$$J_{eq} \ddot{\theta}_m + B_{eq} \dot{\theta}_m - \tau_m = \left(M_n \ddot{x}_n - F_{mu} \right) \left(\frac{d_p}{2} \frac{1}{n} \frac{\xi_1}{1 + \mu \xi_1} \right) \tag{3-13}$$

where the term ξ_1 is equal to

$$\xi_1 = \frac{\mu \cos \lambda - \cos \theta_n \sin \lambda}{\cos \theta_n \cos \lambda + \mu \sin \lambda} \tag{3-14}$$

The conversion of the linear acceleration of the nut $\ddot{x}_n$ to the angular acceleration of the screw $\ddot{\theta}_m$ is given by

$$\ddot{x}_n = \ddot{\theta}_m \left(\frac{d_p}{2} \tan \lambda \right) \frac{1}{n} \tag{3-15}$$

Therefore, by substituting Equation (3-15) in (3-13), the final equation of motion that describes the system is obtained:

$$\left(J_{eq} - \left(\frac{\xi_1 \tan \lambda}{1 + \mu \xi_1} \right) \left(\frac{d_p}{4} \frac{1}{n} \right)^2 M_n \right) \ddot{\theta}_m + B_{eq} \dot{\theta}_m = \tau_m - \left(\frac{\xi_1}{1 + \mu \xi_1} \right) \left(\frac{d_p}{2} \frac{1}{n} \right) F_{mu} \tag{3-16}$$

Equation (3-16) can be rewritten in the following condensed form as

$$\left(J_{eq} - J_1\right)\ddot{\theta}_m + B_{eq}\dot{\theta}_m = \tau_m - \tau_{f1} \qquad (3\text{-}17)$$

where

$$J_1 = \left(\frac{\xi_1 \tan\lambda}{1 + \mu\xi_1}\right)\left(\frac{d_p}{4}\frac{1}{n}\right)^2 M_n \qquad (3\text{-}18)$$

and the term τ_{f1} being equal to

$$\tau_{f1} = C_1 F_{mu} \qquad (3\text{-}19)$$

where

$$C_1 = \left(\frac{\xi_1}{1 + \mu\xi_1}\right)\left(\frac{d_p}{2}\frac{1}{n}\right) \qquad (3\text{-}20)$$

Loading Case 2: The force F_{mu} exerted by the muscles of the amputee has the opposite direction compared to the velocity of the nut $\dot{x}_n$. This scenario is displayed in Figure 3-4.
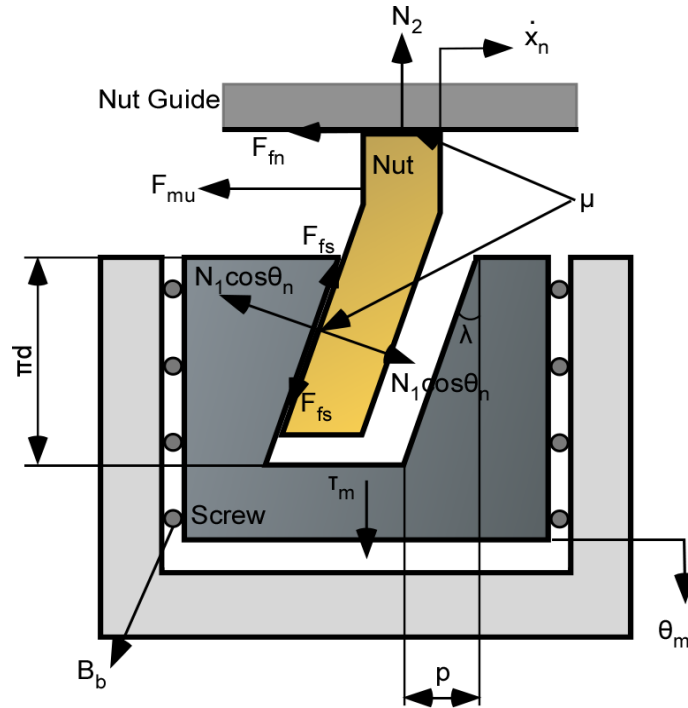
Figure 3-4.   Loading Case (2) Modified from [10].

Following the exact same rationale as in Case 1, the resulting system equation of motion can be written as follows:

$$\left(J_{eq} + \left(\frac{\xi_2 \tan\lambda}{1 - \mu\xi_2}\right)\left(\frac{d_p}{4}\frac{1}{n}\right)^2 M_n\right)\ddot{\theta}_m + B_{eq}\dot{\theta}_m = \tau_m + \left(\frac{\xi_2}{1 - \mu\xi_2}\right)\left(\frac{d_p}{2}\frac{1}{n}\right)F_{mu} \qquad (3\text{-}21)$$

In case 2, the term ξ_2 is equal to

$$\xi_2 = \frac{\mu\cos\lambda + \cos\theta_n \sin\lambda}{\cos\theta_n \cos\lambda - \mu\sin\lambda} \qquad (3\text{-}22)$$

Equation (3-21) can be rewritten in the following condensed form as

$$\left(J_{eq} - J_2\right)\ddot{\theta}_m + B_{eq}\dot{\theta}_m = \tau_m - \tau_{f_2} \tag{3-23}$$

where

$$J_2 = \left(\frac{\xi_2 \tan \lambda}{1 - \mu\xi_2}\right)\left(\frac{d_p}{4}\frac{1}{n}\right)^2 M_n \tag{3-24}$$

and with the term τ_{f2} being equal to

$$\tau_{f2} = C_2 F_{mu} \tag{3-25}$$

where

$$C_2 = -\left(\frac{\xi_2}{1 - \mu\xi_2}\right)\left(\frac{d_p}{2}\frac{1}{n}\right) \tag{3-26}$$

After modelling the mechanical system, to acquire an estimation of the required torque $\tau_{m,req}$, angular velocity $\dot{\theta}_{m,req}$ and power from the master motor $P_{m,req}$, it was necessary to emulate the loading scenarios that the implantable device would be subjected to during the actual application. In other words, the need was to accurately represent the force signals that would be received by the force sensors that would be connected to the residual muscles of the amputee in reality.

For this reason, a model that imitates the behaviour of human muscles had to be created. Fortunately, this work was done in a previous Diploma Thesis by the Diploma Student Anestis Mablekos-Alexiou, who built a Simulink model in Matlab that provides an estimation of the response of the human muscles depending on the input of the neuromuscular system [10]. This model was based on the lumped parameters model that was developed by Winters and Stark [16], [17], [18]. The logic behind the inner workings of the model is displayed in Figure 3-5.
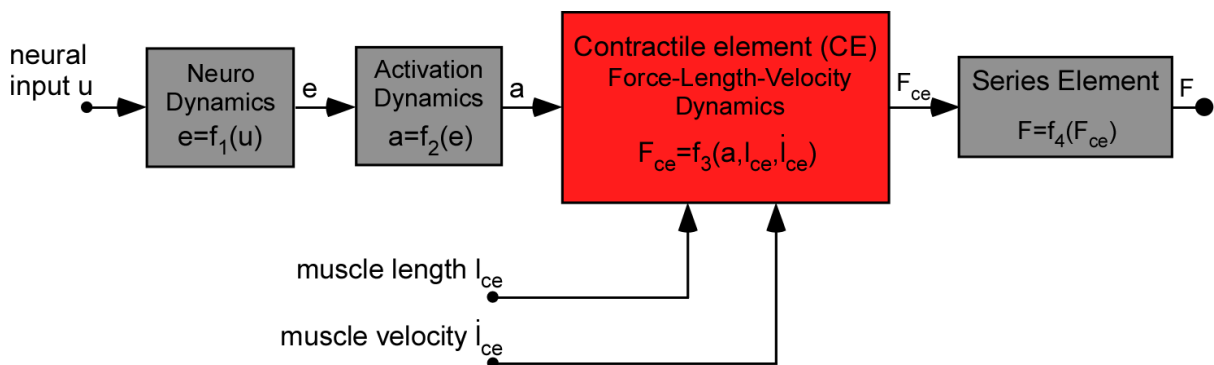
Figure 3-5.   Neuromuscular model block diagram [10].

More precisely, the Simulink model accepts a neural signal '*u*' as the input, representing the human intention to perform a specific motion using the upper limb. By also selecting proper parameters (e.g. the length of the muscles, the range of motion of the limb, etc.) and through the equations of the model that are listed and carefully explained in [10], the model provides an estimation of the forces F_{mu} and velocities $\dot{x}_{mu}$ of the agonist and antagonist muscles that are required for the limb to perform the desired movement path indicated by the neural signal input.

Since the linear displacement of the lead screw nut has to follow the motion of the muscle, using Equation (3-2), the direct correlation between the required angular velocity of the motor $\dot{\theta}_{m,req}$ and the muscle's velocity $\dot{x}_{mu}$ can be expressed by Equation (3-27).

$$\dot{\theta}_{m,req} = \dot{x}_{n,req}\left(\frac{2}{d_p \tan \lambda}\right)n = \dot{x}_{mu}\left(\frac{2}{d_p \tan \lambda}\right)n \qquad (3\text{-}27)$$

Also, the required torque $\tau_{m,rea}$ that the master motor should be able to provide to the master mechanism can be obtained by writing Equations (3-17) and (3-23) in the following form:

$$\tau_{m,req} = (J_{eq} - J_{1,2})\ddot{\theta}_{m,req} + B_{eq}\dot{\theta}_{m,req} - \tau_{f1,2} \qquad (3\text{-}28)$$

From (3-28) it is obvious that if the required angular velocity of the motor is known through (3-27), the only thing left to acquire an estimation for the required torque is to assign appropriate values to all other parameters of the model regarding geometric (D, p, β, n), inertial (J_{eq}) and dynamic friction (B_{eq}) characteristics. The values selected to complete the theoretical simulation are listed in Table 3-4.

Subsequently, the necessary power requirements $P_{m,req}$ from the master motor could be calculated by Equation (3-29).

$$P_{m,req} = \tau_{m,req}\dot{\theta}_{m,req} \qquad (3\text{-}29)$$

Table 3-4.   Selected values for the parameters of the linear actuator.

Description	Symbol	Value	Unit
Equivalent moment of inertia	J_{eq}	$1.05e-8$	kgm^2
Equivalent viscous friction coefficient	B_{eq}	$2.5e-7$	$\frac{kgm^2}{s}$
Coefficient of friction	μ	0.12	$-$
Lead screw diameter	D	$2e-3$	m
Lead screw pitch	p	$0.5e-3$	m
Thread angle	β	14.5	deg
Nut mass	M_n	$10e-3$	kg
Gear ratio	n	1.2	$-$

It should be pointed out that the parameters listed in Table 3-4 do not represent the actual final parameters of the master system that was constructed in the lab. They simply constitute value approximations based on bibliography or desirable characteristics, that were used with the sole purpose of receiving an estimation of the specifications that the master motor should meet. Unfortunately, as it will be explained in the respective chapters regarding the hardware selection process, mainly due to product scarcity along with cost and time restrictions, some parameters such as the lead screw pitch p or the gear ratio n, had to be altered slightly.

The diagram in Figure 3-6 summarizes the work-flow followed to determine the desired master motor specifications.
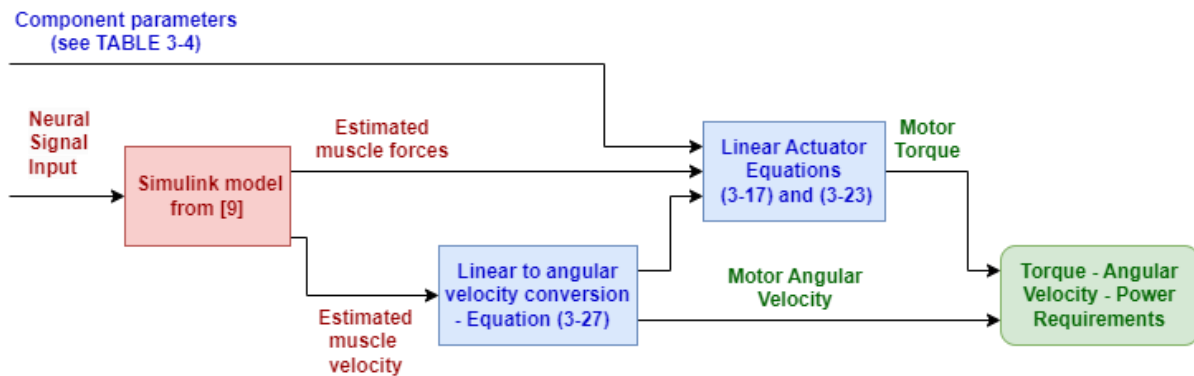
Figure 3-6.   Work-flow diagram.

The exact requirements calculated concerning the torque, angular velocity and power of the master motor are listed in Table 3-5.

Table 3-5.   Torque – Angular Velocity – Power requirements for the Master Motor.

Requirement	Symbol	Value	Unit
Max. Torque	T_{max}	1.47	mNm
Max. Angular Velocity	ω_{max}	5113	rpm
Max. Power	P_{max}	0.31	W
Torque at max. Power	$T_{o,max}$	0.59	mNm
Angular velocity at max. Power	$\omega_{o,max}$	5037	rpm

3.1.2   Power Consumption Restriction

At this point, another critical specification concerning the power consumption of the master system must be discussed. In 2015, an initial analysis regarding the safety and feasibility of the Biomechatronic EPP upper limb prosthesis controller was performed [11]. In that work, among other factors, the thermal losses of the implant were taken into consideration to examine the aspect of human safety. The initial findings suggested that the proposed topology is safe and feasible, assuming that each master motor placed inside the amputated limb would have a power consumption no more than 0.5 W. Based on these findings, in the current thesis, the power consumption goal that was defined during the master system's design process was that each of the master mechanism should not exceed an average consumption of 0.5 W during its operation.

After having defined all of the above necessary characteristics and specifications that the master system should meet, each mechanical component that was selected for this project is presented.

3.1.3 Master Motor Selection

The master motor of choice was the Maxon DCX08 EB KL 4.2V (Figure 3-7).

DCX 8 M $\varnothing$8 mm, precious metal brushes, DC motor

Key Data: 0.5/1.0 W, 0.65 mNm, 17300 rpm
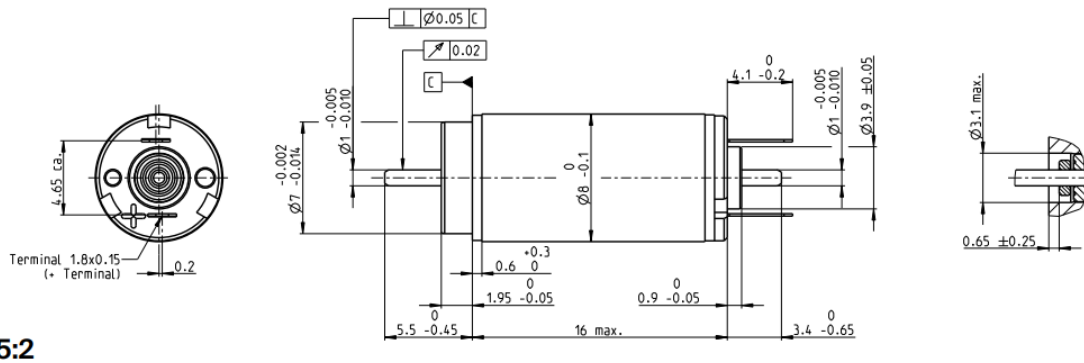
M 5:2

Figure 3-7.   Master Motor - Maxon DCX08 EB KL 4.2V.

The above motor is a brushed DC motor equipped with Maxon's precious metal brushes and ball bearings. Its diameter is 8 mm and its power rating is 0.5 W.

Several characteristic values of the motor are presented in Figure 3-8, while the Torque/Speed curve, at the nominal voltage of 4.2 V, is displayed in Figure 3-9. The datasheet stating the complete product specification list is quoted in Appendix A.

Product specification	
Values at nominal voltage	
Nominal voltage	4.2 V
No load speed	11600 min^{-1}
No load current	10.1mA
Nominal speed	4970 min^{-1}
Nominal torque (max. continuous torque)	0.641 mNm
Nominal current (max. continuous current)	0.199 A
Stall torque	1.14 mNm
Stall current	0.34 A
Max. efficiency	69.3 %
Characteristics	
Max. output power continuous	1.03 W
Terminal resistance	12.3 Ω
Terminal inductance	0.0411 mH
Torque constant	3.36 mNm A^{-1}
Speed constant	2850 min^{-1} V^{-1}
Speed/torque gradient	10500 min^{-1} mNm^{-1}
Mechanical time constant	4.15ms
Rotor inertia	0.0379 gcm^{2}

Figure 3-8.   Master Motor (Maxon DCX 8 M $\varnothing$8 mm) specifications.
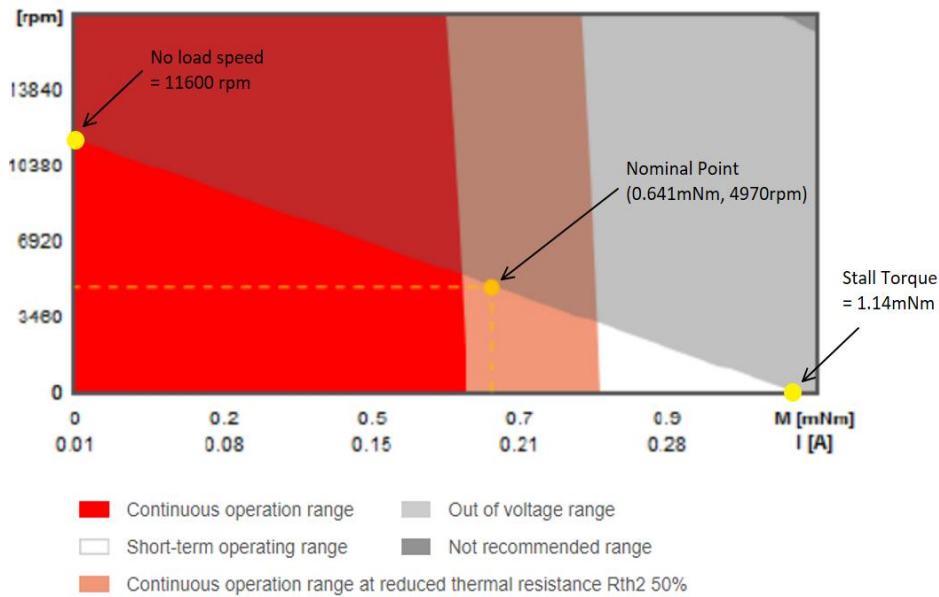
Figure 3-9.   Maxon DCX 8 M Ø8 mm torque/speed curve at nominal voltage (4.2 V).

The selected motor fulfils the dimension and power restrictions set during the design stage. It must be stated that during the experimental phase of this thesis, due to the torque requirements of the application, the voltage supplied to the master motors had to be increased up to 8V for the motor to be able to provide the necessary torque. This voltage increase allowed the stall current to reach values of around 0.45 A. Taking into consideration the torque constant of the motor, which is equal to 3.36 mNm A^{-1}, in theory, the available stall torque of the master motors during the experiments was 1.51 mNm.

3.1.4   Encoder Selection

The need to measure the position of the master motors led to the selection of Maxon's encoders ENX 8 MAG 256IMP (Figure 3-10).
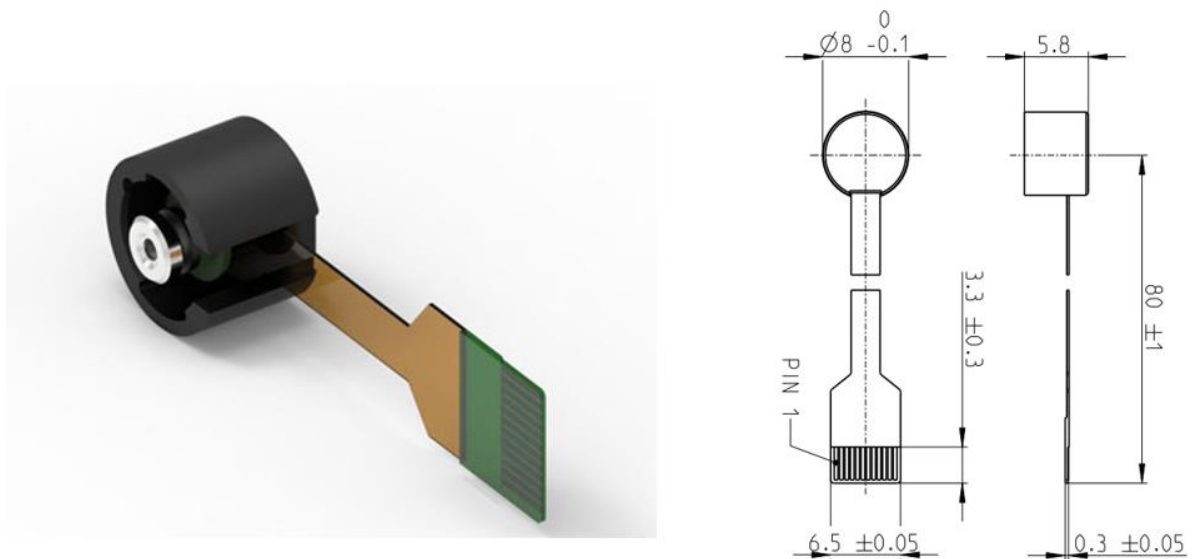
Figure 3-10. Master Encoder - ENX 8 MAG 256IMP.

This specific encoder is the only compatible option offered by Maxon that could be attached to the corresponding selected master motor. It is a 3-channel incremental encoder with 256 counts per turn.

The major technical data of the encoder are given in Figure 3-11, while the complete datasheet can be found in Appendix A.

Product specification	
Sensor data	
Counts per turn	256
Number of channels	3
Line Driver	No
Max. electrical speed	100000 min[1]
Max. mechanical speed	100000 min[1]
Technical data	
Supply voltage Vcc	3.3 V ±10 %
Output signal	INC
Output signal driver	Single Ended / CMOS
Output current per channel	-4...4 mA
State length	45…135 °el
Signal rise time/Signal fall time	10/10 ns
Min. state duration	ns

Figure 3-11. Master Encoder (ENX 8 MAG 256IMP) specifications.

A challenging task encountered in the lab was that an adaptor that provides easy access to the pins of the encoder's Flexible Printed Circuit (FPC) cable was required to supply voltage to the motor and the encoder and to receive the encoder's pulses.

The commercial option offered by the manufacturer was an expensive and bulky adaptor with a high lead time. Therefore, it was decided to create a custom adaptor in the lab. For this purpose, the Molex 52745-1297 female FPC connector was purchased (Figure 3-12), which constitutes a compatible connector for the aforementioned encoder cable.

(a)   (b)

Figure 3-12. Molex 52745-1297, 0.5mm Pitch, 12 Way Right Angle Female FPC Connector (a) Front view (b) Back view.

In addition, a breakout board had to be designed so that standard jumper cables could be easily connected to the pins of the Molex connector. The breakout board was designed using the EAGLE PCB design software (Figure 3-13 (a)) and was constructed in a CNC machine (Figure 3-13 (b)).
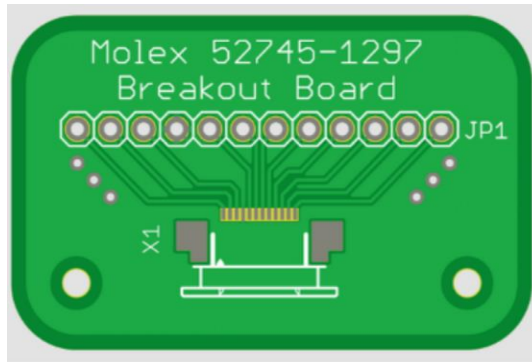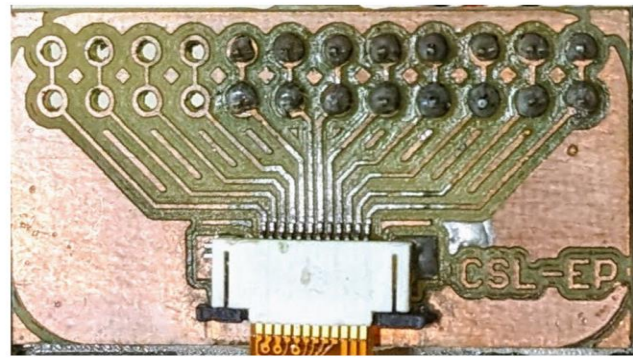
(a)   (b)

Figure 3-13. Breakout Board (a) Designed in EAGLE PCB software (b) Constructed in the lab.

The complete master motor-encoder-breakout board setup is displayed in Figure 3-14.
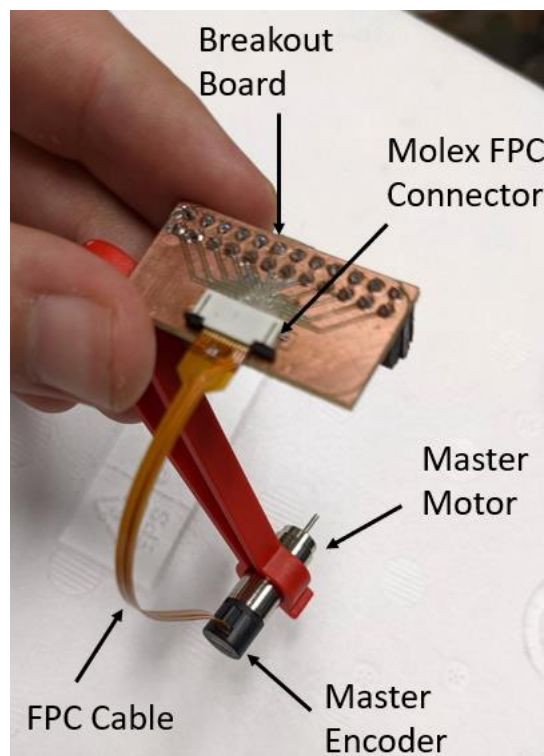
Figure 3-14. Motor – Encoder – Breakout board setup.

3.1.5   Master Motor Driver Selection

For the control of the DC master motors, an appropriate driver had to be identified. Initially, due to the nature of the master motors operation, it was decided that a current mode control scheme should be implemented. Current mode control directly determines the available torque of the system and, therefore, the system's acceleration. This fact was considered important since the priority was to achieve quick responses from the master system. Having the opportunity to instantly define the torque of the motor could facilitate the function of the linear actuator in cases where high-magnitude forces and/or forces with a rapid change of direction are exerted by the amputee's muscles.

For this purpose, a few commercial drivers were tested to see if a current mode control scheme could be applied. Unfortunately, despite exhaustive efforts, no compatible driver with

such capabilities was found. It is believed that due to the low current requirements (less than 500 mA per master motor), it was impossible to define the motor's current supply with the desired accuracy as was required by the application.

Consequently, a voltage mode control strategy was adopted. For voltage mode control, a plethora of commercial drivers were suitable. However, since it was used in previous works [8], the Texas Instruments' DRV8833 dual motor driver carrier was instantly available at the Control Systems Lab. The specifications of the aforementioned driver and its compatibility are thoroughly examined in Petros Konstantinea's Master Thesis [7], with whom we worked together on this part of the project. Nevertheless, the tiny breakout board of the DRV8833 is displayed in Figure 3-15 and its main features are mentioned below.
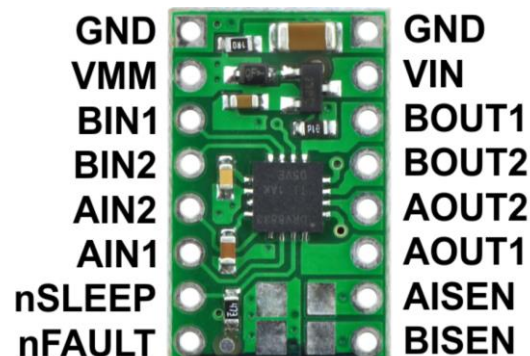
Figure 3-15. TI's DRV8833 Motor Driver Pinout [21].

Driver main features:
- Dimensions: 12.7 mm x 20.3 mm.

- Weight: 1.0 g.

- Can drive two DC motors simultaneously.

- Operating voltage: 2.7 V to 10.8 V.

- Output current: 1.2 A continuous (2 A peak) per motor.

- PWM signals can be applied to the input pins.

- Under-voltage lockout and protection against over-current and over-temperature.

- Reverse-voltage protection circuit.

The above characteristics are more than satisfying to control the selected master motors. During the experimental phase, the operating voltage was set to 8.3 V.

The connectivity map of the driver is presented in Chapter 5, while the corresponding datasheet of the DRV8833 is listed in Appendix A.

3.1.6 Lead screw and Lead Screw Nut selection

As mentioned in Chapter 2, regarding the selection of mechanical components, the general approach was to opt for off-the-shelf parts instead of custom-made ones since the latter choice would not prove to be efficient in terms of cost and lead time.

However, in the case of the lead screw system, this approach could not be applied. Due to the miniature size of the lead screw and the unique geometric configuration of its nut (see Figure 3-16 and Figure 3-17), a custom-made construction was required.
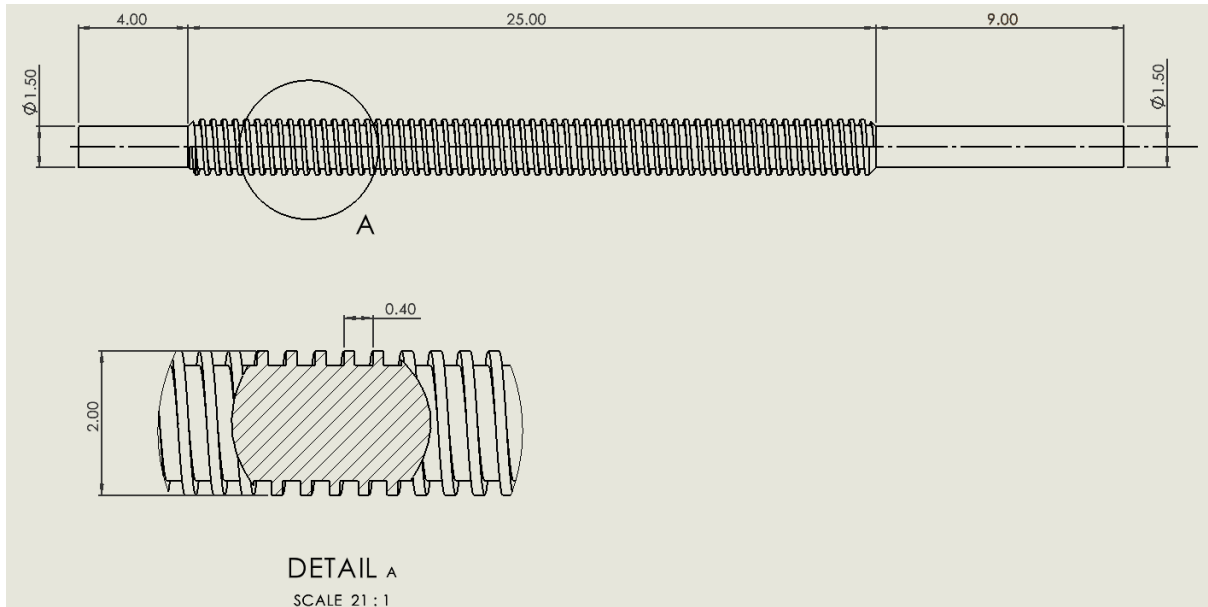
Figure 3-16. Lead screw Engineering Drawing.
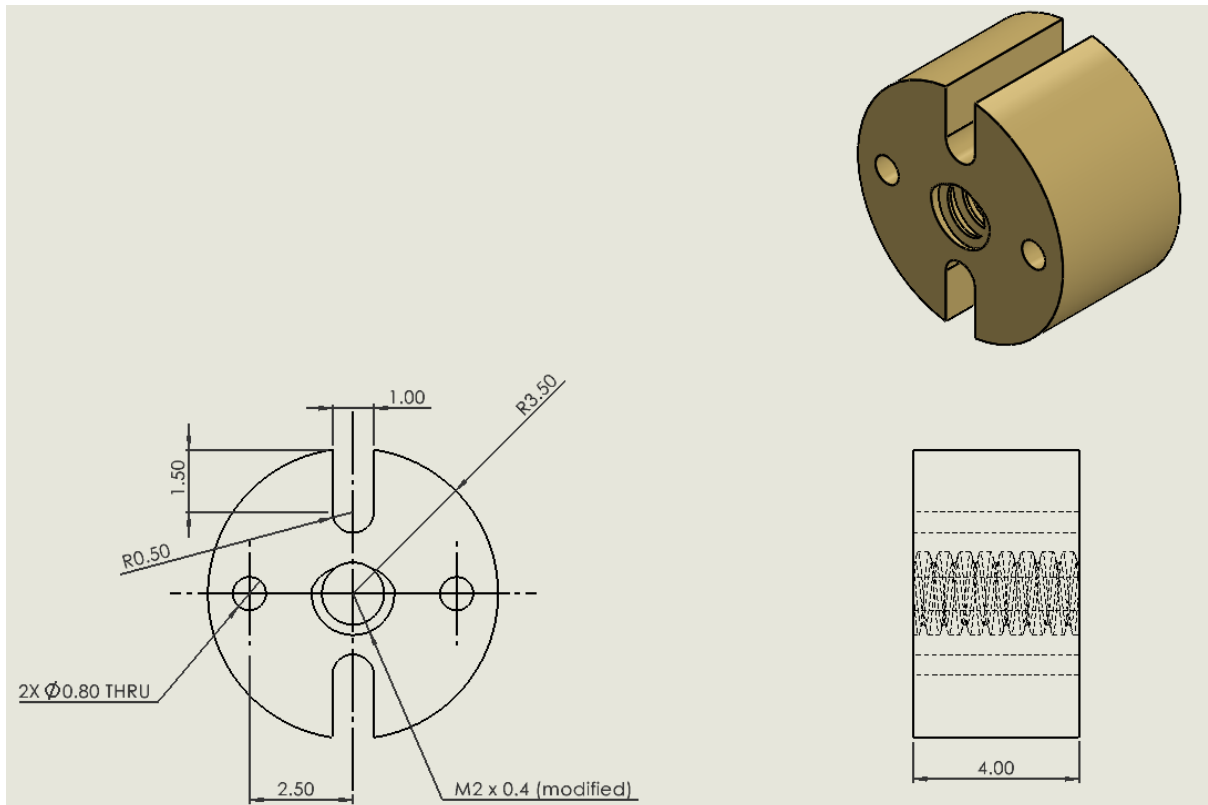
Figure 3-17. Nut Engineering Drawing.

On the one hand, as can be seen from the engineering drawings, both ends of the screw had to be machined to allow the placement of bearings with the ultimate purpose of achieving a smooth and stable rotating motion.

On the other hand, the nut had to have particular cuts so it could slide along guides that would prevent its rotation and ensure a linear operating motion. Moreover, small holes had to be drilled in the nut; a fact that would prove useful in tying the fishing lines that would connect the nut with the force sensor housing and eventually the residual muscle.

For the aforementioned reasons, for the construction of the lead screw system, a close collaboration with the Watchmaker Stamatios Kamatselos was realized. The end result is displayed in Figure 3-18.

Figure 3-18. Lead screw, Nut, Bearings and Gear Ring Adaptor.

Next, the main features of the designed lead screw system will be discussed.

- **Diameter, lead and non-backdrivability**

The constructed lead screw has a diameter D of 2 mm and a lead l of 0.4 mm. The selection of these geometric characteristics derived from the need to create the smallest non-backdrivable lead screw system that could endure the force magnitude of an amputee's muscles, while at the same time maintaining the highest possible level of lead screw efficiency.

The following equation defines the efficiency ε of a lead screw system [24].

$$\varepsilon = (\tan \lambda)\left[\frac{\cos \theta_n - \mu \tan \lambda}{\cos \theta_n \tan \lambda + \mu}\right] \tag{3-30}$$

It must also be noted that the thread angle λ depends on the lead l and the diameter D of the thread, as expressed in Equation (3-31).

$$\lambda = \arctan\left(\frac{l}{\pi D}\right) \tag{3-31}$$

Therefore, as the thread lead l increases, the thread angle λ increases and most importantly the efficiency ε of the system increases as well. However, the non-backdrivability feature of a lead screw mechanism is generally ensured only if the following condition holds true [24].

$$\varepsilon < 50\% \tag{3-32}$$

Considering all of the above, the goal was to create a 2mm diameter lead screw with the highest possible lead, which would not increase the system's efficiency over the 50% threshold. An additional factor that influenced the final design decision was that for the creation of the lead screw system, a thread tap and die set had to be purchased (see Figure 3-19). The available commercial standardized thread tap and die sets that met the desired specifications were the 2 mm x 0.4 mm ones. Consequently, despite the fact that, in theory, it was possible to select a lead screw system with a greater lead, the practical restrictions enforced the final dimensional characteristics.

Figure 3-19. Tap and Die used by the watchmaker for the manufacturing of the lead screw system.

- **Resolution**

The combination of a screw with a 0.4 mm lead, along with a 256 counts encoder and a gear ratio of 1:1, offers a linear displacement resolution of $\Delta x_n = 1.56 \mu m$. That is to say that each count of the encoder corresponds to a 1.56μm linear displacement of the lead screw nut, which is considered a more than satisfactory resolution level for the control of the system.

- **Thread Length**

The screw's thread length le_u constituted another important aspect of the lead screw system that had to be determined. This quantity corresponds to the available length that the nut could travel in order to linearly displace the residual muscle. As can be seen from the engineering drawing (see Figure 3-16), le_u was set equal to 25 mm. This number was specified based on the following rationale:

According to a study carried out in [1], healthy volunteers required approximately 50° of wrist extension and 45° of wrist flexion in order to perform a series of daily life activities. Therefore, the total functional range of the wrist joint could be assumed to be equal to $\theta_{range} = 95°$.

Making also the simplified assumption that a human wrist joint could be represented by an ideal rotational joint with a lever arm equal to $r_{joint} = 12\,mm$ [10], the maximum linear displacement $\Delta x_{mu_{MAX}}$ of the muscles attached to the wrist joint could be calculated from the following equation:

$$\Delta x_{mu_{MAX}} = r_{joint} \theta_{range} \frac{\pi}{180} \approx 20 \; mm \tag{3-33}$$

Finally, considering that the lead screw nut has width w_n of 4 mm (see Figure 3-17), the thread length le_u was ultimately determined as

$$le_u = \Delta x_{mu_{MAX}} + w_n + e_{margin} = 20 + 4 + 1 = 25\,mm \tag{3-34}$$

where $e_{m\arg in}$ is the error margin considered to avoid collisions of the nut with the mechanism housing during the experimental tests. A total margin value of 1 mm, which essentially provides a 0.5 mm error margin in each direction, was considered satisfactory.

3.1.7 Gear Selection

Two plastic (polyacetal) spur gears with a 0.5 module and 18 teeth were selected to transfer the power of the master motor to the lead screw system.

Plastic was the preferred material for the gearing system. The main advantage of plastic gears is their low density which does not significantly increase the inertia of the system, while at the same time being able to transfer the small torque requirements of the application. Ideally, to further reduce the inertia of the gearbox, instead of using only two gears for the prototype, three or more smaller gears could be used (with smaller diameters and the same final gear ratio). Nevertheless, the construction of such a miniature gearbox would require industrial precision and accurate placement of the components and therefore this concept could not be applied to the project at that point in time.

The selected gear ratio was 1:1 and was based on the calculations performed during the modelling stage of the mechanism. Moreover, since it was almost impossible to use more than two gears, a gear ratio other than 1:1, entails that one of the gears should have a greater diameter. This fact would result in an increase of the mechanism's total dimensions and would oppose the attempt to create the smallest possible implant device.

Figure 3-20 presents the geometric specifications of the selected gears.

Material:	Plastic
Typ:	Spur gear
Outside diameter da:	10
gearing:	straight
Hub diameter ND:	7,8
Nominal diameter d:	9
Modulus:	0,5
Hub:	with hub
Inside diameter B:	4
Width b:	3
Number of teeth:	18
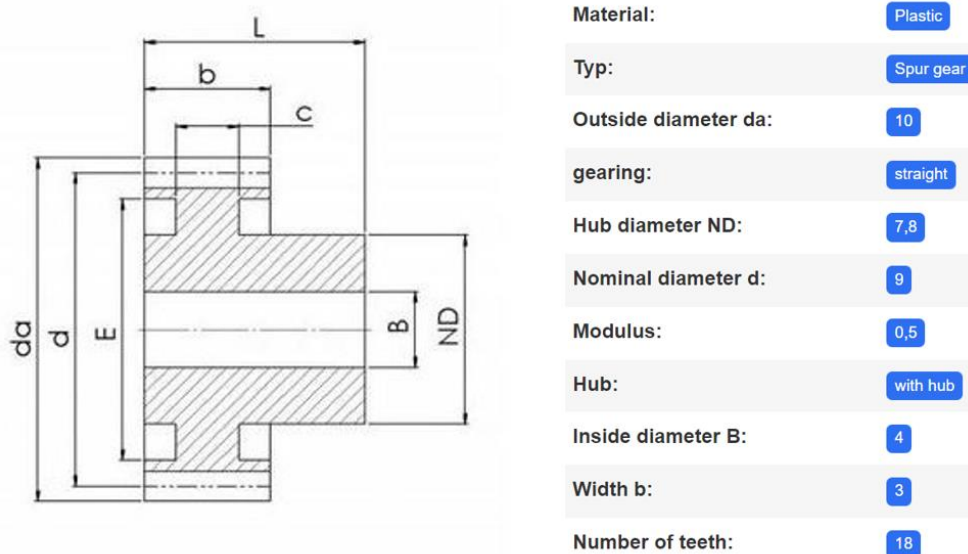
Figure 3-20. Gear Specifications [22].

Note that even though there is a variety of available miniature gears in the market, no off-the-shelf gear satisfied all the restrictions of this project. Hence, after the purchase of the gears, post-processing had to take place. In particular, firstly, the gear hub had to be removed since it was unnecessary. Secondly, plastic rings had to be created. Those were intended to be placed between the inner diameter of the gear and the outside diameter of the motor and lead screw shafts, thus ensuring the tight fit of the gears to the shafts. Both post-processing procedures were carefully carried out using the lathe at the Manufacturing Technology Lab (NTUA) (see Figure 3-21).
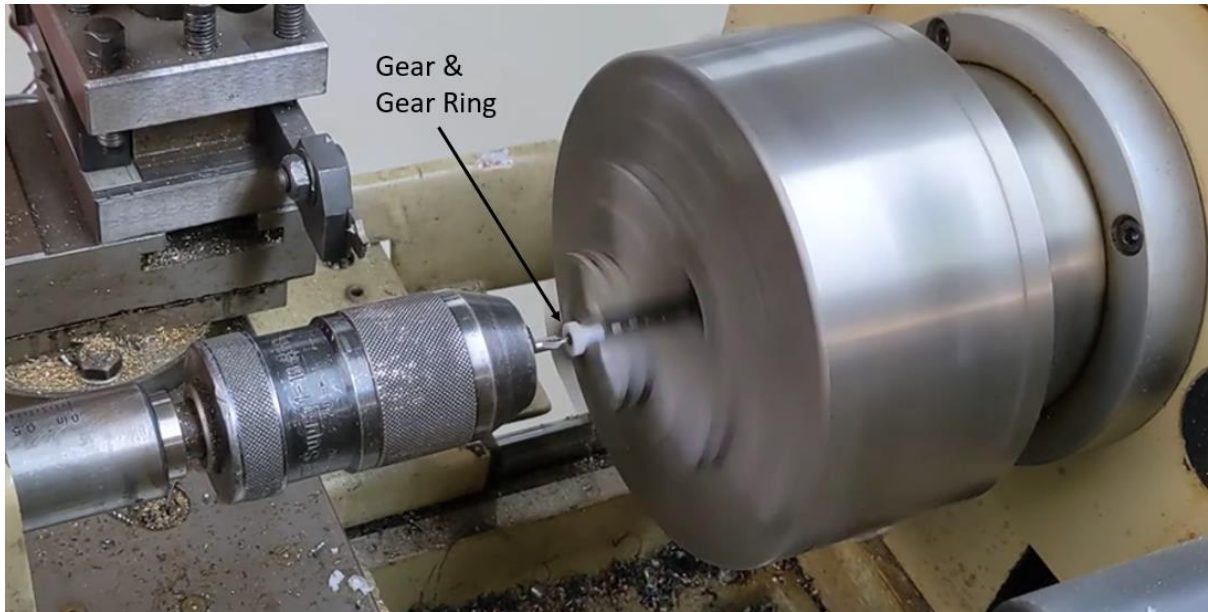
Figure 3-21. Gear Ring manufacturing using a lathe.

The final result is presented in Figure 3-22 and Figure 3-23.
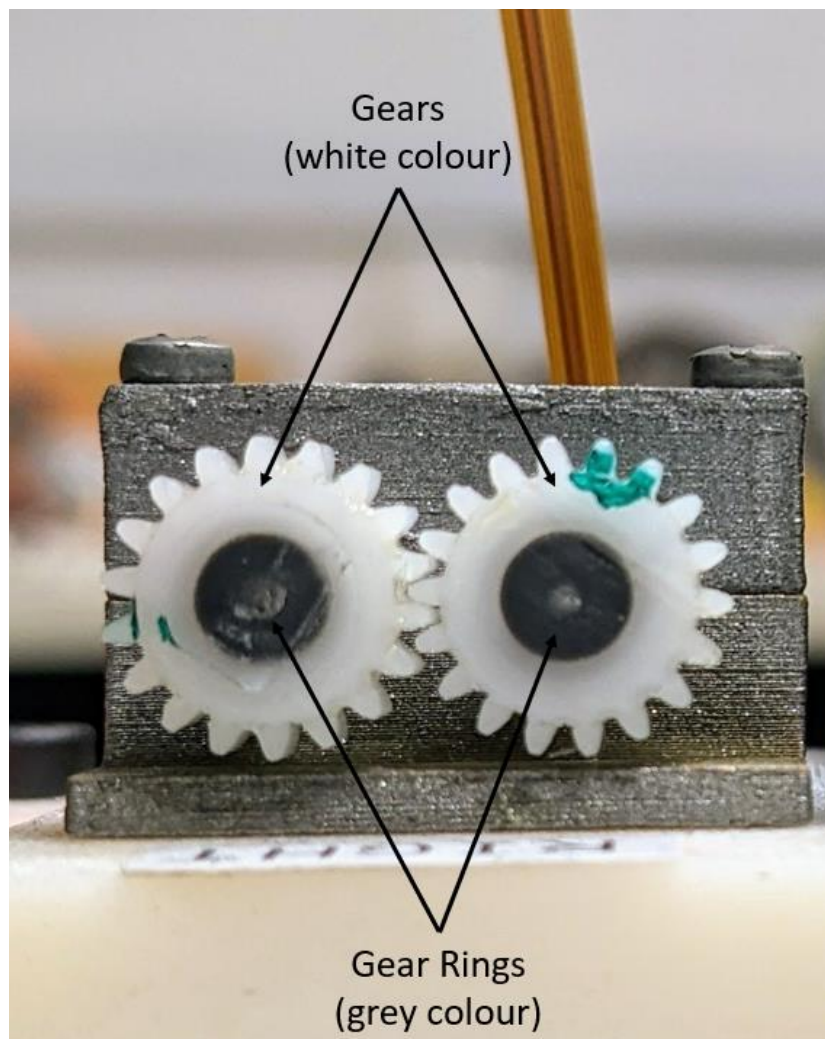
Figure 3-22. Gears and Gear Rings.
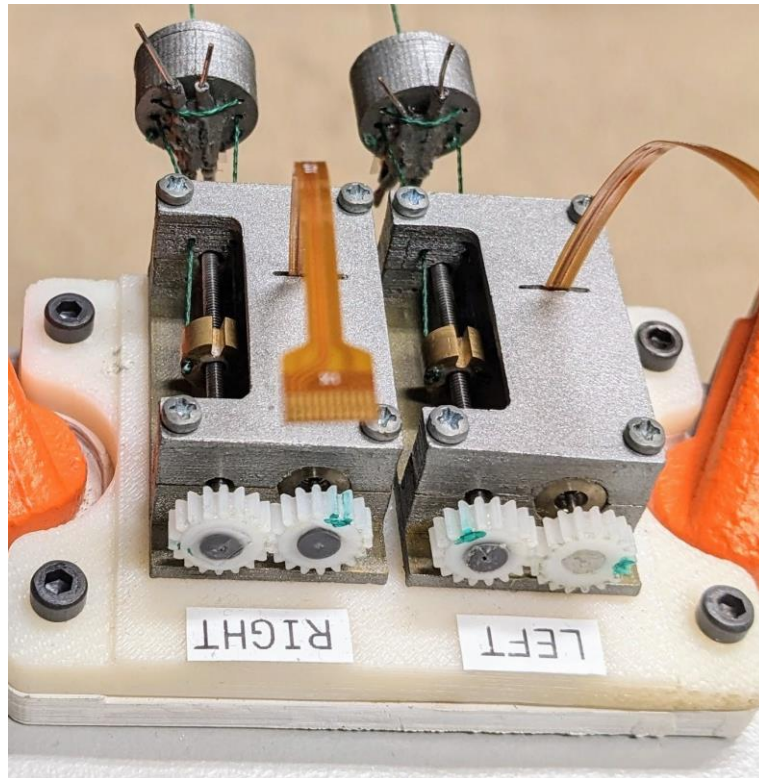
Figure 3-23. Gears as part of the complete master mechanism.

3.1.8 Bearing selection

Bearings constituted another important mechanical component for the smooth operation of the master linear actuator. The chosen bearings were the 681-X-ZZ NBZ single row deep groove miniature ball bearings. In Figure 3-24, the bearing and its dimensions are displayed.

Dimensions	Symbol	Value
Bore diameter	d	1.5 mm
Outside diameter	D	4 mm
Width	B	2 mm

(a)   (b)
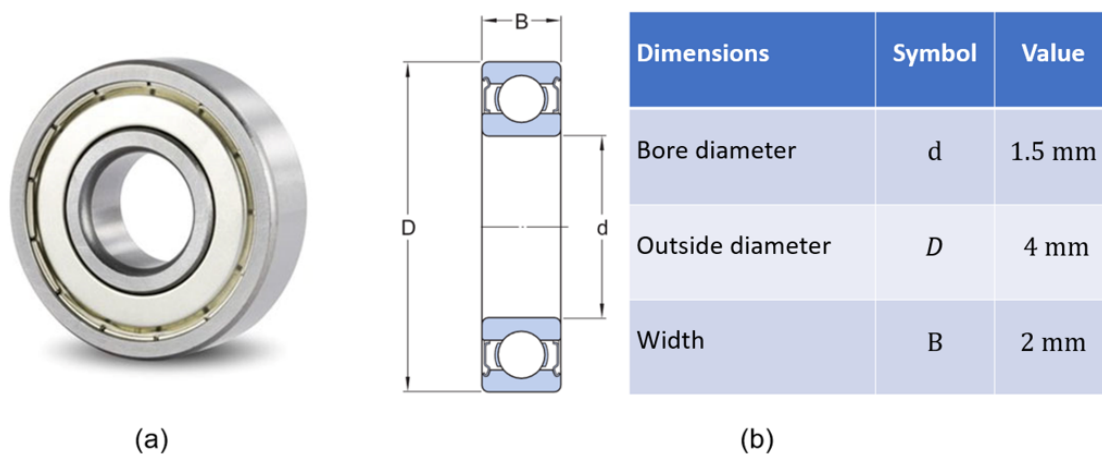
Figure 3-24. (a) Deep groove ball bearing 681-X-ZZ NBZ (b) Bearing dimensions [23].

Deep groove ball bearings are capable of withstanding considerable axial and radial loads in both directions. There are also suitable for high speeds, well beyond the maximum required 5113 rpm mentioned in Table 3-5, while at the same time operating quietly; which is a desirable feature for this application. Unfortunately, no specification datasheet for the particular selected bearing model could be found.

3.1.9 Fishing Braid

To test the new linear actuators in the lab, a thin, flexible (but not stretchable) and durable material had to be used to connect the lead screw nut with the force sensor housing (see Figure 3-25). For this purpose, a fishing braid was considered the best option due to its characteristics, low cost and availability. During the experimental tests, the fishing braid would also be used to apply forces to the force sensor, thus enabling the user of the experimental setup to imitate the loading scenarios that the master system would endure by the amputated muscles in the actual application.

The selected fishing braid was the Black Diamond PE - 4Braid. The relevant main features of the braid are:

- Braid diameter 0.3 mm
- Stretch 0%
- Can withstand forces up to 200 N
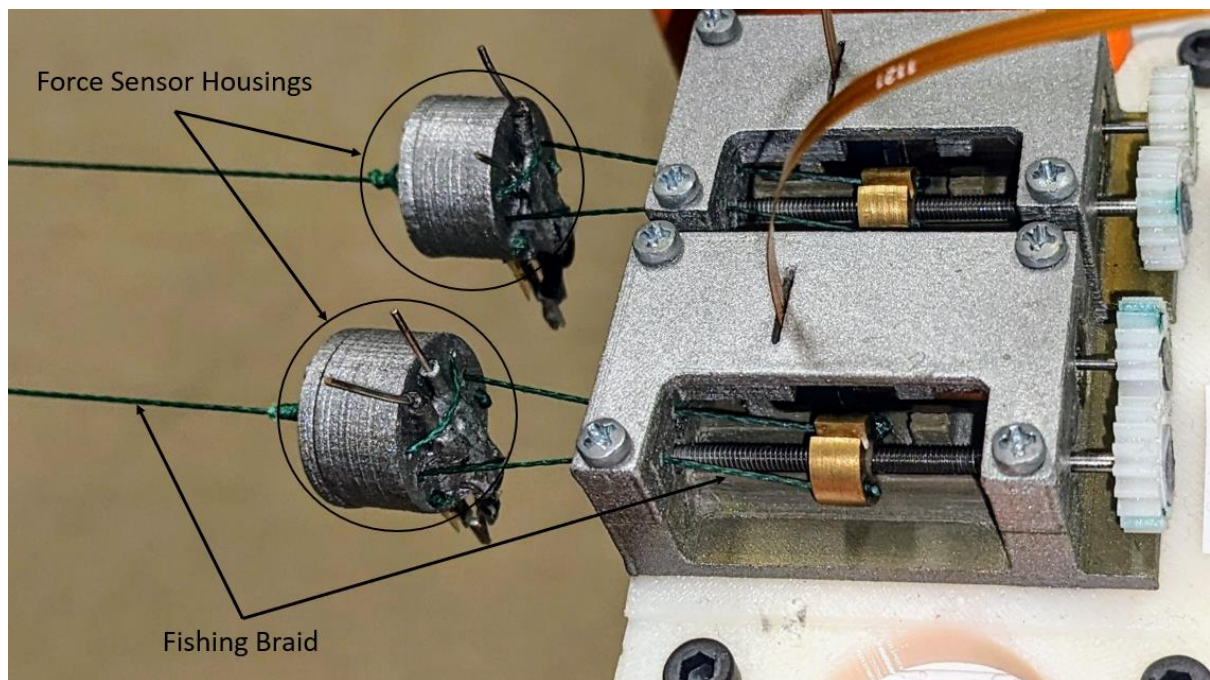
Figure 3-25. Fishing Braid used to connect the lead screw nut with the force sensor housing.

It must be emphasized that the use of a fishing line constituted a practical solution for the sole purpose of performing tests in the lab and it is not suggested to be used in the actual implantable device to connect any mechanical components.

3.2 Force Sensors

An essential function that the master system must perform, is the measurement of the forces using a force sensor that is intended to be placed between the residual muscles of the amputee and the linear actuator. In the past, for this purpose, a widely known force sensor type called Force Sensitive Resistor (FSR) was used. FSRs are materials whose resistance changes when a force is applied to their surface. Even though FSRs cannot provide high accuracy measurements, their small size and low cost make these components ideal for lab experimenting. Therefore, in the context of attempting to create the smallest possible master

system, new, smaller FSRs were selected, and new FSR housings were designed and 3D-printed.

3.2.1 FSR selection

The newly selected FSRs are the FSR 400 Round Short Tail by Interlink Electronics. The main advantages of the new FSRs compared to the ones used in previous works are the smaller dimensions and the wider force measuring range. More specifically, they can detect forces in the range of 0.1 N – 20 N, which is considered sufficient based on the fact that the average maximum force that an amputee can exert is around 15 N (based on [2] muscle cineplasty and exteriorized tendons amputees have the capability to exert forces grossly from 5.9 N (maximum force for weak amputees) up to 24.5 N (maximum force for strong amputees)). The tiny dimensions of the product are displayed in Figure 3-26.
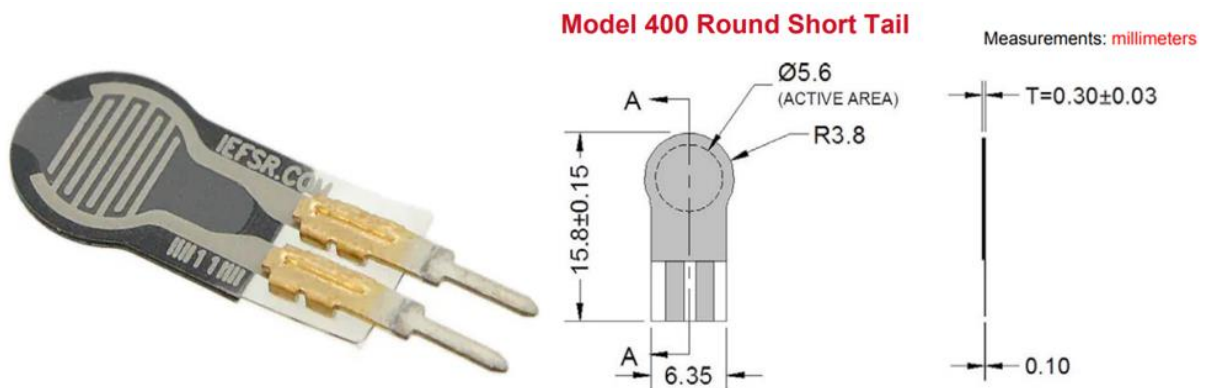
Figure 3-26. FSR Model 400 Short Tail by Interlink Electronics.

3.2.2 FSR Housing

For the integration of the newly selected FSRs into the rest of the master system, firstly, appropriate housings had to be designed. These housings would allow the proper loading of the FSR so that the received force measurements would be as reliable and accurate as possible. Due to the small dimensions of the components involved, this task proved to be more difficult than initially seemed. In particular, the housings had to fulfil at least the following criteria:

- The housings should be an assembly of parts that allow short relative motion between them for the loading of the FSR to occur.
- The exerted force had to be evenly distributed to the FSR's surface (uniform loading).
- As soon as no force was exerted, the residual stresses of the structure should be zero.

Next, the final FSR housing design is presented. Figure 3-27 (a) displays the complete assembly, while Figure 3-27 (b) shows the exact same thing but with the outer parts of the housing being transparent, thus revealing the inside configuration.

(a)   (b)
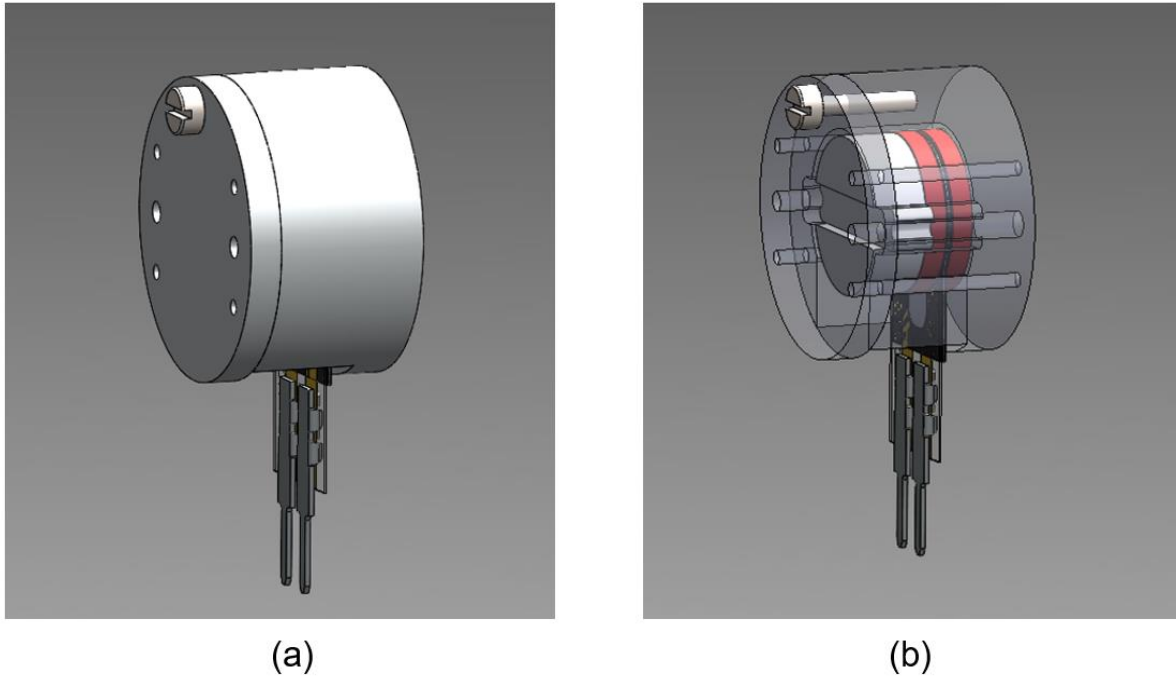
Figure 3-27. (a) FSR Housing (b) FSR Housing with some transparent parts.

In Figure 3-28, the Exploded View feature in Solidworks was used to provide a clearer visual. The housing is comprised of three 3D-printed parts and two elastic pads. The thin elastic pads ensure the best possible contact with the sensor's surface, thus contributing to the uniform loading of the FSR. In order for the forces to be picked up by the sensor, a pressure plate is used to press against the FSR's surface as soon as the fishing braid connecting the FSR with the supposing muscle is pulled (see Figure 3-30).
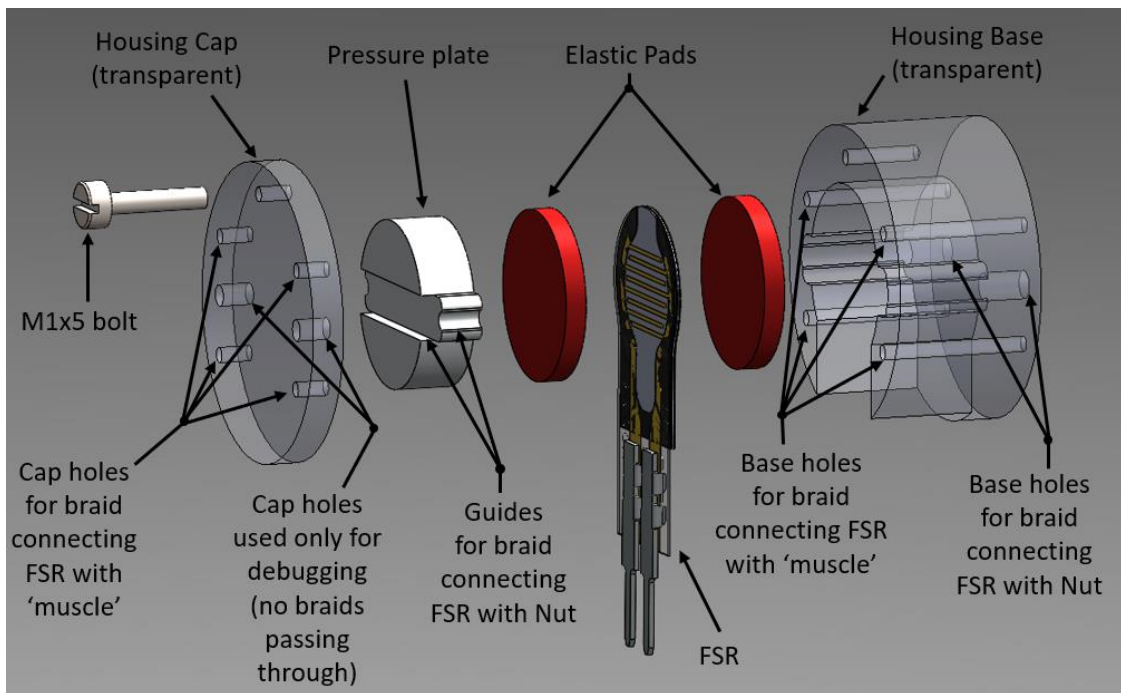
Figure 3-28. Exploded View of the FSR Housing.

Figure 3-29 (a) shows how the FSR housings were integrated with the linear actuators of the master system in the lab, while Figure 3-29 (b) displays the exact same setup in Solidworks

but with some of the housing's parts being transparent for the fishing braid connections to be visible.

(a)   (b)
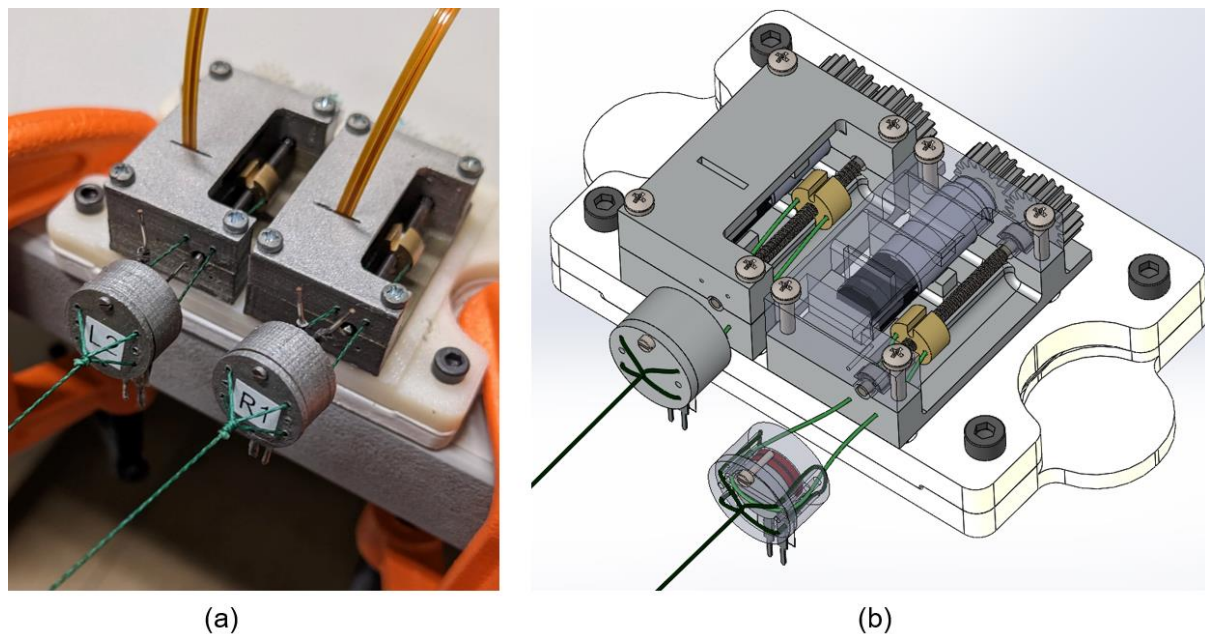
Figure 3-29. (a) FSR Housings as part of the master system in the Lab (b) FSR Housings part of the master system in Solidworks.

A transparent close up picture of the FSR housing is presented in Figure 3-30. The light-green coloured fishing braid is used to connect the lead screw nut with the force sensor, while the dark-green braid connects the sensor with the user. In the lab, during the tests, forces were exerted on the system by essentially pulling the dark-green braid. This would push the pressure plate part on the elastic pad, thus squeezing the FSR and ultimately changing its resistance. The harder the user pulls the braid, the higher the change in the sensor's resistance.
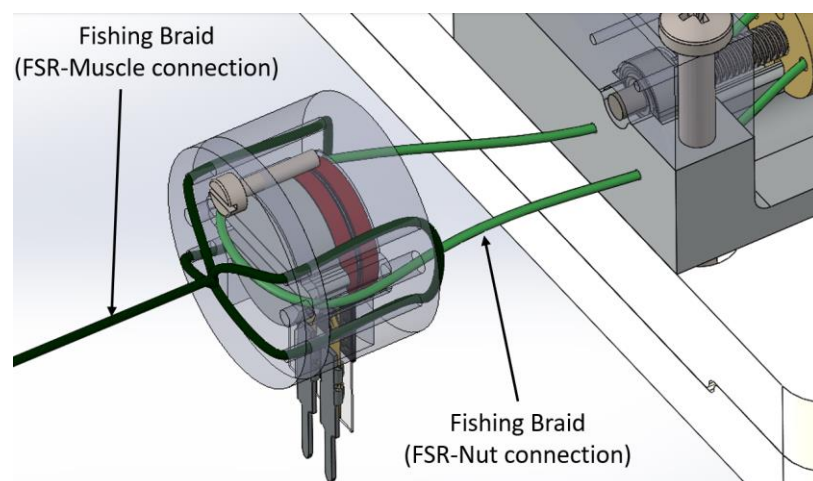
Figure 3-30. Fishing braid configuration of the FSR housing (with transparent parts).

The working principle of the FSR housing is also graphically illustrated in Figure 3-31 where a section view of the housing is presented.
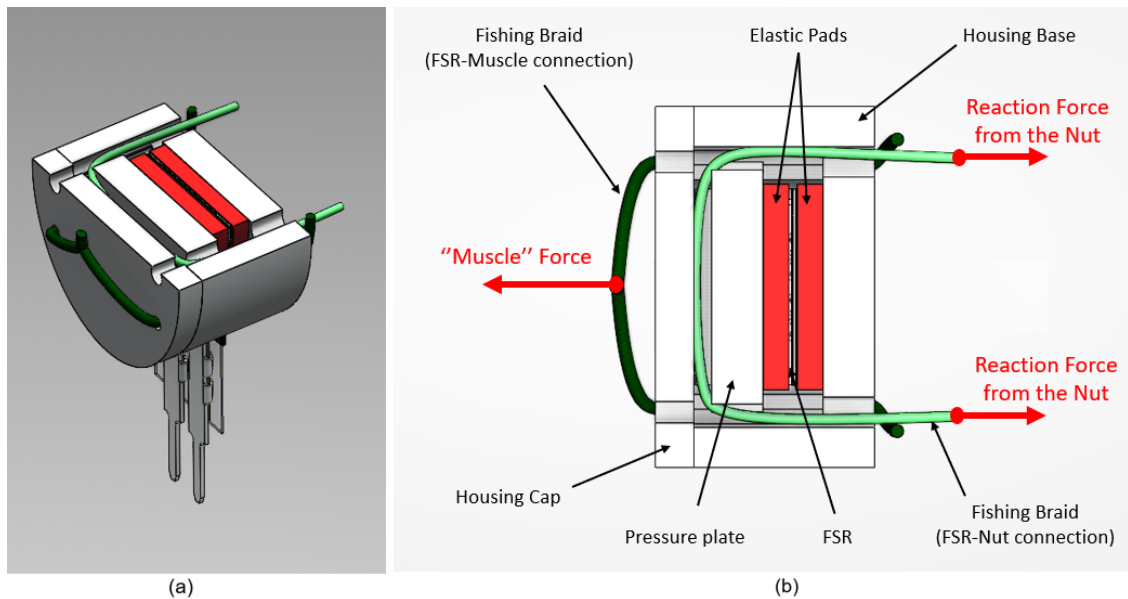
Figure 3-31. Working Principle of the FSR Housing - Section (a) Isometric View (b) Top View.

3.2.3 FSR Calibration

Before the new FSRs were ready to be used along with the rest of the master system, a calibration process was required. As mentioned previously, the way that the FSRs indicate the magnitude of the force applied to them is by changing their resistance. As a result, when the FSRs are part of an electronic circuit, the change in resistance corresponds to a change in the voltage drop across the sensor. Depending on the configuration of the circuit, a specific correlation between the force applied to the sensor and the output voltage of the circuit can be observed. Thus, the purpose of the calibration process is precisely to determine a mathematical formula that describes the relationship between the applied force and the circuit's output voltage.

The electronic circuit that was used is displayed in Figure 3-32.
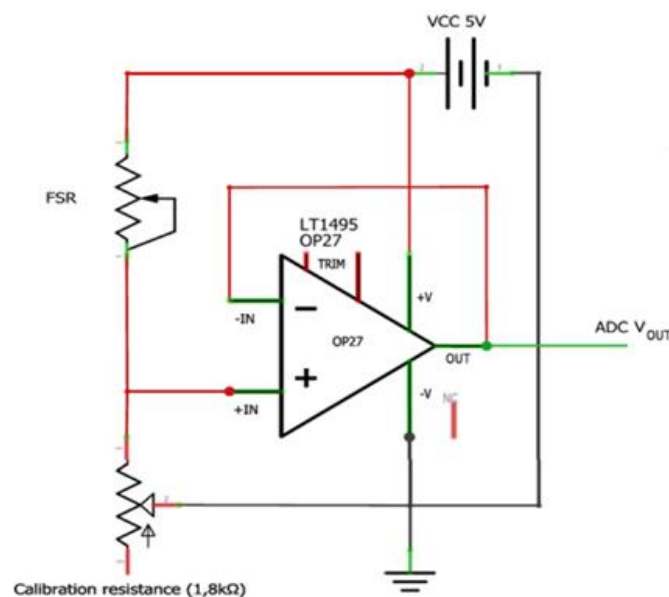
Figure 3-32. FSR circuit diagram modified from [7].

A detailed explanation of the circuit and the calibration process is presented in [7]. To avoid extensive repetition, in this thesis, only the results of the calibration will be presented. It is worth mentioning, however, that the calibration process was performed by gradually increasing the loading of the FSRs using calibrated weights, while at the same time recording the output voltage of the FSR circuit.

Figure 3-33 and Figure 3-34 display the recorded measurements taken during the calibration process. The two graphs indicate the relationship between the circuit's output voltage (V) and the weight (g) applied to FSR 1 and FSR 2 respectively. The calibration process had to be carried out separately for each FSR since slight manufacturing differences among the sensors and more importantly among the housings were expected.

$$y = 428.32x^3 - 1806x^2 + 2539x - 708.6$$
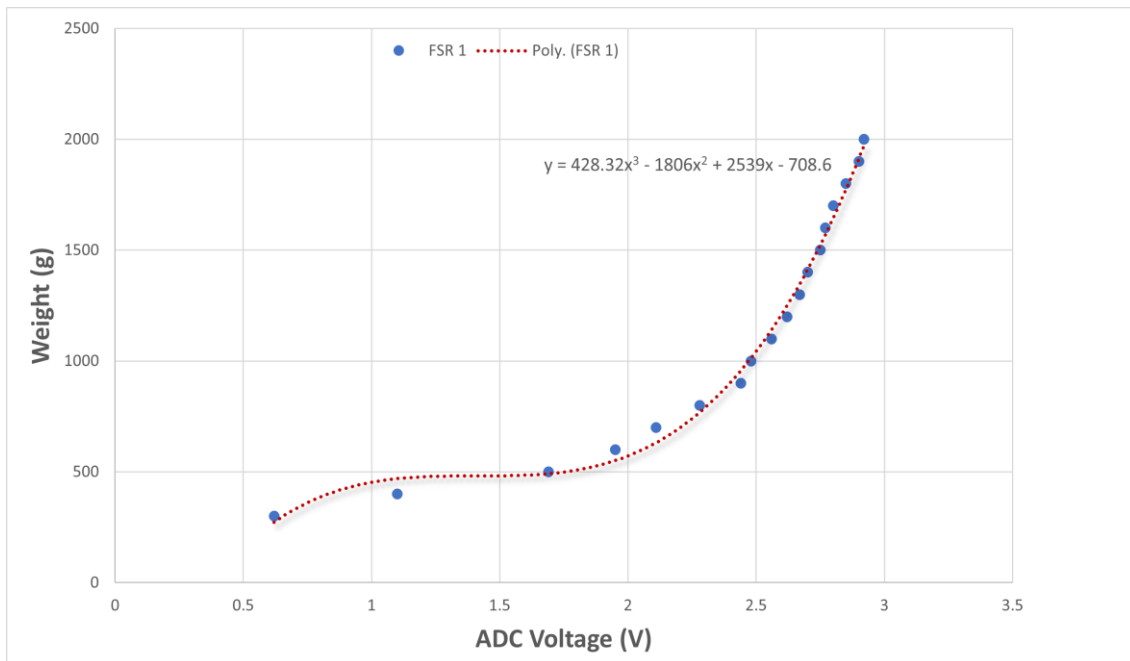
Figure 3-33. FSR1 calibration graph.

$$y = 454.59x^3 - 2029.7x^2 + 3202x - 1393.9$$
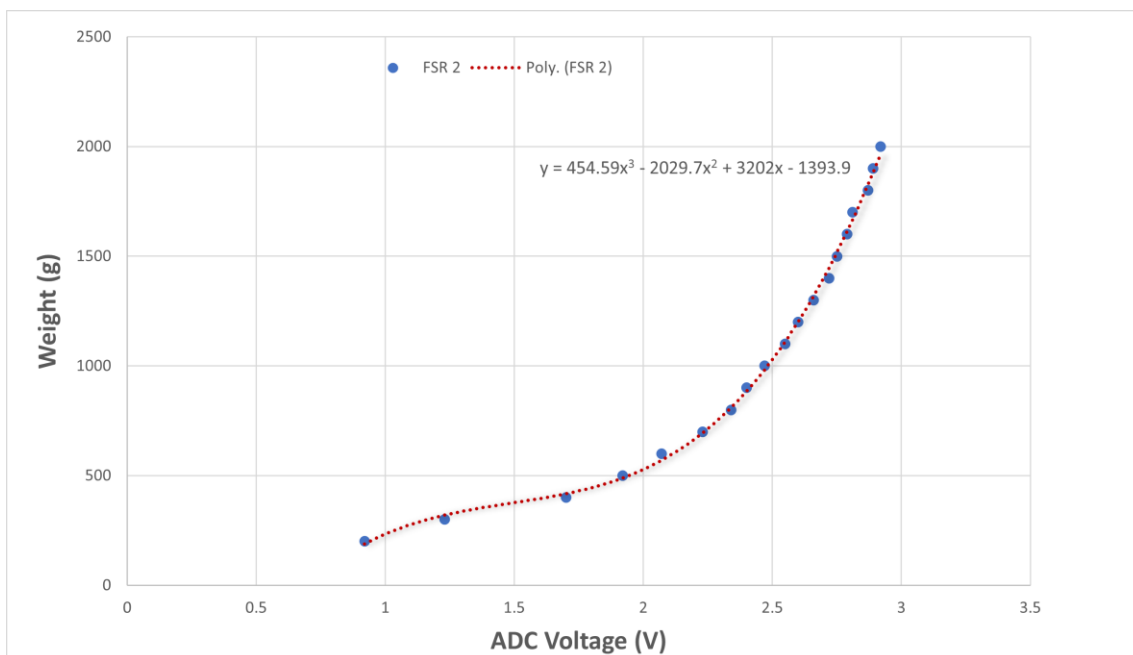
Figure 3-34. FSR2 calibration graph.

Lastly, a curve fitting method using a 3rd order polynomial function was applied to the experimental data. As a result, the following mathematical equations were obtained, where *x* is the output voltage in millivolts (mV) and *y* is the applied weight in grams (g).

FSR 1:

$$y = -708.602 + 2539.024x - 1806x^2 + 428.324x^3 \qquad (3\text{-}35)$$

FSR 2:

$$y = -1393.889 + 3202.032x - 2029.667x^2 + 454.591x^3 \qquad (3\text{-}36)$$

Of course, to obtain the actual force measurement in Newtons, the variable y should be multiplied by $10^3 \cdot g$, where g is the gravitational acceleration in m/s^2.

3.3 Slave System

The slave system, which represents the prosthetic limb, was constructed during a previous Diploma Thesis [10]. In the current thesis, for the imitation of the wrist motion, the same components were used. For purposes of completeness, the parts that constitute the slave system will be briefly mentioned below.

The slave motor of choice was the Maxon RE 30 Ø30 mm, Graphite Brushes, 60 Watt (see Figure 3-35).
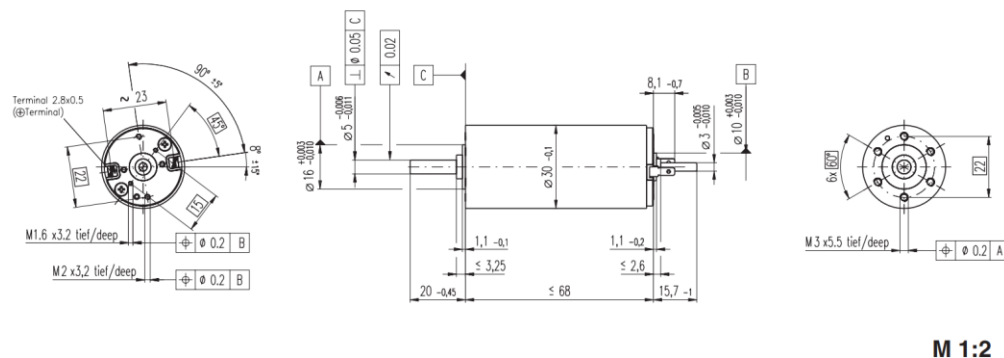
Figure 3-35. Slave Motor Dimensions (for the complete Datasheet see Appendix A).

The encoder utilized to keep track of the slave motor's position, was the HEDS 5540 500 counts per turn, 3 channels, displayed in Figure 3-36.

Figure 3-36. Encoder for the slave motor (for the complete Datasheet see Appendix A).

In addition, the Planetary Gearbox GP 32 C with a gear ratio of 343/17576 was attached to the shaft of the slave motor (see Figure 3-37).

Planetary Gearhead GP 32 C ⌀32 mm, 1.0 - 6.0 Nm
Ceramic Version

Technical Data	
Planetary Gearhead	straight teeth
Output shaft	stainless steel
Shaft diameter as option	8 mm
Bearing at output	ball bearing
Radial play, 5 mm from flange	max. 0.14 mm
Axial play	max. 0.4 mm
Max. radial load, 10 mm from flange	140 N
Max. permissible axial load	120 N
Max. permissible force for press fits	120 N
Sense of rotation, drive to output	=
Recommended input speed	< 8000 rpm
Recommended temperature range	-20 ... +100°C
Extended area as option	-35 ... +100°C

M 1:2

Option: Low-noise version

Figure 3-37. Gearbox attached to the slave motor (for the complete Datasheet see Appendix A).

For the control of the slave motor, the selected driver was the Analog Servo Drive AZBDC10A4 by Advanced Motion Controls (AMC), displayed in Figure 3-38.

SPECIFICATIONS	
Current Continuous (A)	5
Current Peak (A)	10
DC Supply Voltage (VDC)	10 - 36
Size (mm)	38.1 x 38.1 x 7.34

Figure 3-38. Motor Driver for the slave motor (for the complete Datasheet see Appendix A).

It is worth noting that unlike the master motor driver DRV8833, the AZBDC10A4 slave driver offers the possibility to control the slave motor using a current mode control scheme. This feature was exploited and more on this matter can be found in Chapter 4.2, where the control scheme is presented.

The complete slave system including the motor, encoder, gearbox, driver and a 3D-printed hand (representing the prosthetic limb) are displayed in Figure 3-39.
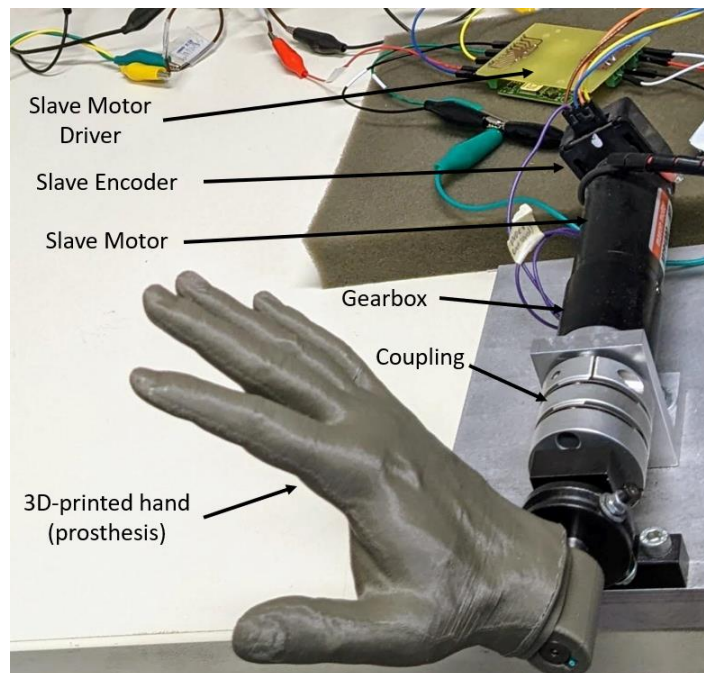
Figure 3-39. Slave system setup.

4   System Identification and Control

Following the selection of all the components that constitute the master linear actuator, a process of identifying the parameters of the system had to be conducted. In this Chapter, the steps and results of this process will be described in detail. Subsequently, the design of the control scheme for both the slave and master systems will be thoroughly presented.

4.1   Master System Parameter Identification

The parameter identification procedure is essential for any system. The knowledge of a system's parameters paints a full picture when it comes to understanding the strengths and weaknesses of the system in question. It enables the prediction of the system's behaviour in various scenarios and allows the design of the appropriate controller.

In this work, a well-defined methodology was followed to identify the parameters of the master system. For notation purposes, the two master motors will be referred to with the subscripts 'L' and 'R' accordingly. For example, the torque constant of the left master motor will be expressed by the notation K_{TL}, while for the right motor, the term K_{TR} will be used. It is also worth noting that the accuracy of the measurements presented below heavily depends on the accuracy of the instruments that were employed during the process. Those were the Hameg 7042-5 power supply (Figure 4-1 (a)), the Agilent U1252A digital multimeter (Figure 4-1 (b)) and the ENX 8 MAG master motor encoder (see Figure 3-10).

(a)   (b)
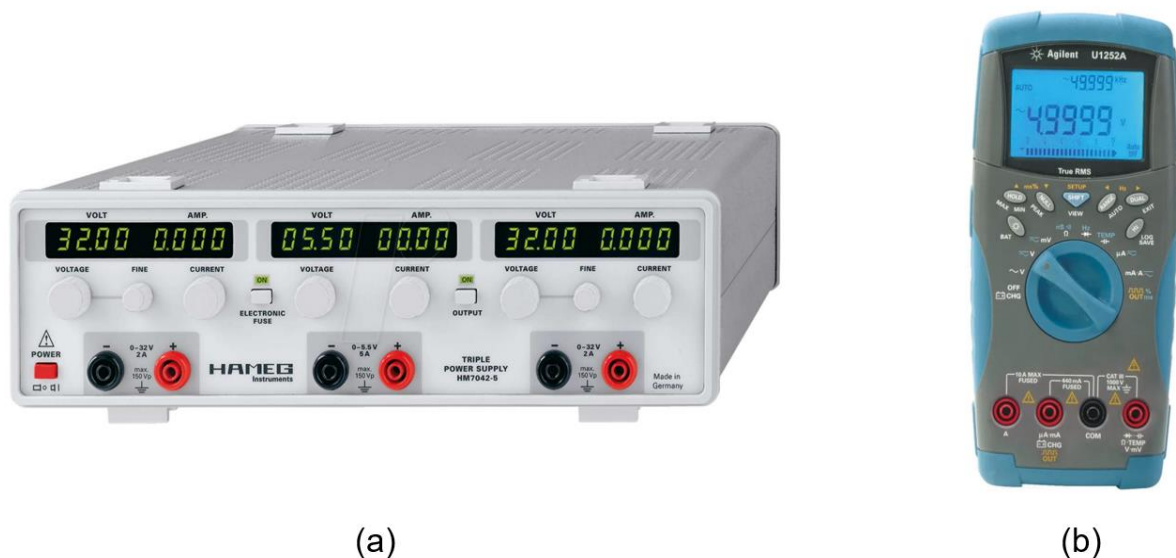
Figure 4-1.   (a) Hameg 7042-5 Power Supply (b) Agilent U1252A Digital Multimeter.

First, the specifications listed on the datasheet of the selected master motor had to be verified. More specifically, the resistance R_a and the torque constant K_T of each of the master motors were examined.

Figure 4-2 illustrates the equivalent circuit of a DC motor.
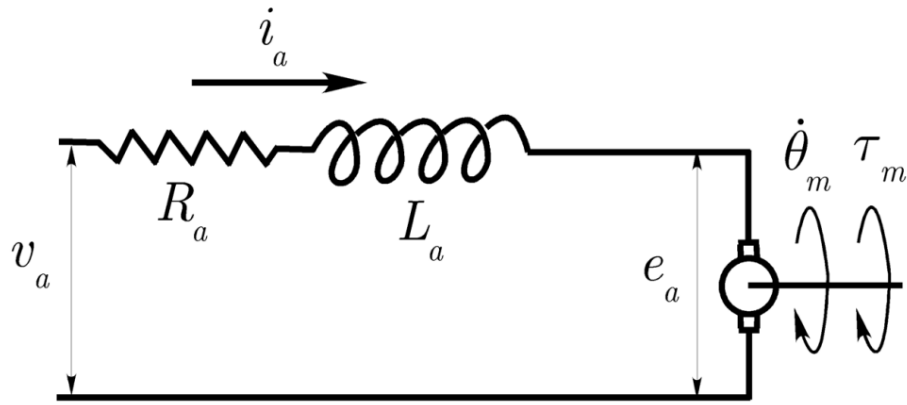
Figure 4-2. DC Motor equivalent circuit.

Due to its negligible magnitude, the induction of the motor L_a can be disregarded and therefore the equation for an ideal brushed DC motor can be given by

$$V_a = K_T \dot{\theta}_m + R_a i_a \tag{4-1}$$

where V_a is the voltage supplied to the motor, i_a the current running through the motor, K_T the torque constant, R_a the resistance of the motor and $\dot{\theta}_m$ the angular velocity.

Thus, if the resistance R_a is known, the torque constant K_T could be experimentally determined by providing a specific voltage V_a to the motor while simultaneously measuring the current i_a and the velocity $\dot{\theta}_m$.

4.1.1   Resistance R_a

The resistance of the motors was the first parameter to be identified and the measurements were performed using the digital multimeter. The important thing to remember is that in the experimental setup, the master motor receives its power through the FPC cable of the encoder, which is connected to the breakout board and the corresponding jumper cables (see Section 3.1.3). Therefore, for the experimental tests to follow, the combined resistance of all the aforementioned components should be taken into consideration since those components constitute an integral part of the setup.

The results of the measurements were $R_{aL} = 14.73\ \Omega$ and $R_{aR} = 14.88\ \Omega$.

4.1.2   Torque Constant K_T

After having determined the resistance of each mechanism, the torque constants could be calculated by the following equation:

$$K_T = \frac{V_a - R_a i_a}{\dot{\theta}_m} \tag{4-2}$$

To receive the most reliable results possible, three separate measurements were executed. In each measurement, the supplied voltage was altered (1st Test at 2V, 2nd at 3V and 3rd at 4.2V). The current i_a and velocity $\dot{\theta}_m$ of the motors were measured using the multimeter and the pulses of the encoder, respectively. In each test, the results were almost identical for both motors.

The calculated torque constants were $K_{TL} = 3.357\ mNm \cdot A^{-1}$ and $K_{TR} = 3.354\ mNm \cdot A^{-1}$.

Thus far, the master motors were examined separately from the rest of the components. However, for the upcoming steps of the identification process, the complete linear actuator

mechanisms were assembled since the system had to be examined as a whole. As presented in the previous chapter, the equation that describes the dynamic behaviour of the master mechanism has the following form:

$$J_{eq}\ddot{\theta}_m + B_{eq}\dot{\theta}_m = \tau_m - \tau_f \tag{4-3}$$

The next parameters to be identified were the static friction $T_{f_{st}}$ (which constitutes a subset of the term τ_f), the equivalent viscous damping coefficient B_{eq} and the equivalent moment of inertia J_{eq}. It is noteworthy that the order in which the identification occurred was important since the discovery of each parameter required knowledge of the previous parameters.

4.1.3   Static Friction $T_{f_{st}}$

To obtain the static friction values, the linear actuators initially had to be at a standstill. Then, the current i_a was monitored while gradually increasing the supplied voltage V_a to the motors using the power supply. The current magnitude i_{start} corresponding to the moment that the axis of the motor began to rotate is the crucial measurement that provides the magnitude of the static friction through the following equation:

$$T_{f_{st}} = K_T i_{start} \tag{4-4}$$

The starting current measurements were $i_{startL} = 40.0\ mA$ and $i_{startR} = 49.2\ mA$. Therefore, the corresponding static frictions were $T_{f_{st}L} = 0.134\ mNm$ and $T_{f_{st}R} = 0.165\ mNm$.

The slight difference observed between the left and right master robots can be attributed to the manufactural inconsistencies, due to the fact that the lead screw systems were handmade. In addition, it has to be taken into consideration that the nut guide was 3D-printed from PLA material and was grinded using a hand file. This process might have contributed to the creation of uneven surfaces along which the lead screw nut comes in contact during the system's operation.

4.1.4   Equivalent viscous damping coefficient B_{eq}

For determining the damping coefficient, the system must be examined during a steady state. Therefore, a constant voltage of 2.75V was applied to the motors while the current and angular velocity were monitored. When the system reached its steady state, the equivalent viscous damping coefficient was obtained from Equation (4-5).

$$B_{eq} = \frac{K_T i_a - T_{f_{st}}}{\dot{\theta}_{m_{ss}}} \tag{4-5}$$

The results for each system were $B_{eqL} = 9.93e-7\ \dfrac{kgm^2}{s}$ and $B_{eqR} = 9.11e-7\ \dfrac{kgm^2}{s}$.

4.1.5   Equivalent moment of inertia J_{eq}

The moment of inertia is directly linked to the transient state of a system. Again, a voltage of 2.75V was applied to the master motors and the angular velocity response was studied. The aim was to determine the time constant τ of the mechanisms through which their equivalent moment of inertia could derive from Equation (4-6). The settling time τ_s required for the response to reach the steady state and stay within a tolerance band of 2% around the final value is equal to four times the time constant (see Figure 4-3).

$$J_{eq} = \tau B_{eq} \tag{4-6}$$
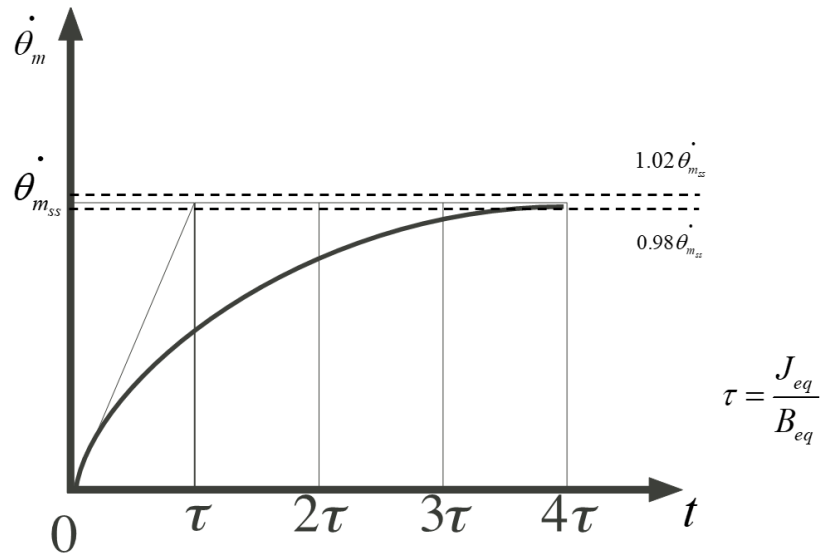
Figure 4-3. Time constant graph.

After close inspection of the angular velocity response graphs, the settling times for each system were assessed at $\tau_{sL} = 4\tau_L = 0.052s$ and $\tau_{sR} = 4\tau_R = 0.058s$. Hence, the equivalent moments of inertia were calculated equal to $J_{eqL} = 1.29e - 8kgm^2$ and $J_{eqR} = 1.32e - 8kgm^2$.

4.1.6 Identified parameters and verification

Table 4-1 and Table 4-2 summarize the parameters identified for the left and right master robots, respectively.

Table 4-1. Parameters of the Left Master System.

Left Master System			
Parameter	**Symbol**	**Value**	**Unit**
Equivalent moment of inertia	J_{eqL}	$1.29e - 8$	kgm^2
Equivalent viscous friction coefficient	B_{eqL}	$9.93e - 7$	$kgm^2 s^{-1}$
Static friction	T_{fstL}	0.134	mNm
Torque Constant	K_{TL}	3.357	$mNmA^{-1}$
Resistance	R_{aL}	14.73	Ω

Table 4-2.   **Parameters of the Right Master System.**

Right Master System			
Parameter	**Symbol**	**Value**	**Unit**
Equivalent moment of inertia	J_{eqR}	$1.32e-8$	kgm^2
Equivalent viscous friction coefficient	B_{eqR}	$9.11e-7$	kgm^2s^{-1}
Static friction	$T_{f_{st}R}$	0.165	mNm
Torque Constant	K_{TR}	3.354	$mNmA^{-1}$
Resistance	R_{aR}	14.88	Ω

Finally, in an attempt to verify the quality of the identified parameters' values, a simplified Simulink model was created to emulate the behaviour of a system with the same values as those listed in the tables above. The model is displayed in Figure 4-4 and constitutes an open-loop system representation of the actual master system examined in the lab. A step input of 2.75V was used to recreate the exact scenario performed in the lab during the identification process. The goal was to run the model and obtain the angular velocity response of the theoretical system in order to compare it with the experimental data that were recorded during the analysis of the actual master system.

Open Loop Velocity Response Operating at 2.75V
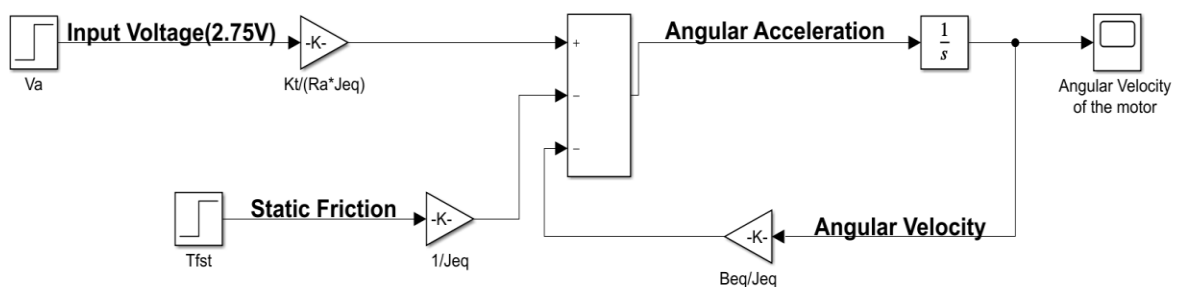
Figure 4-4.   **Simulink model imitating the behaviour of the actual master system.**

The theoretical and experimental angular velocity responses for the left and right master robots are displayed in Figure 4-5 and Figure 4-6 correspondingly.

As can be observed from the figures, the theoretical response produced by the Simulink model and the experimental response received from the actual master system display an almost identical trend.
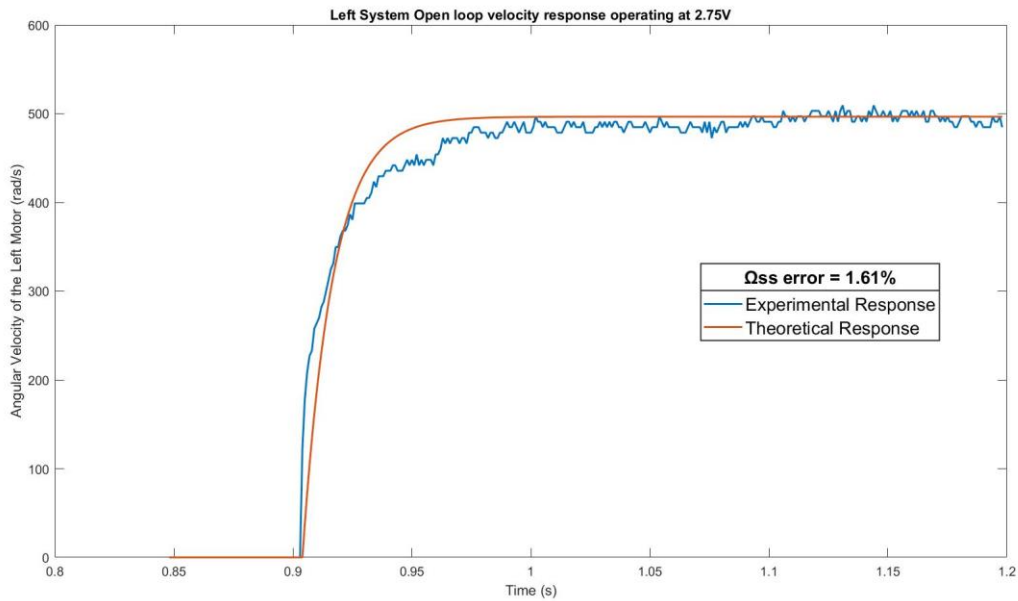
Figure 4-5.   Left master system open loop velocity response operating at 2.75V.
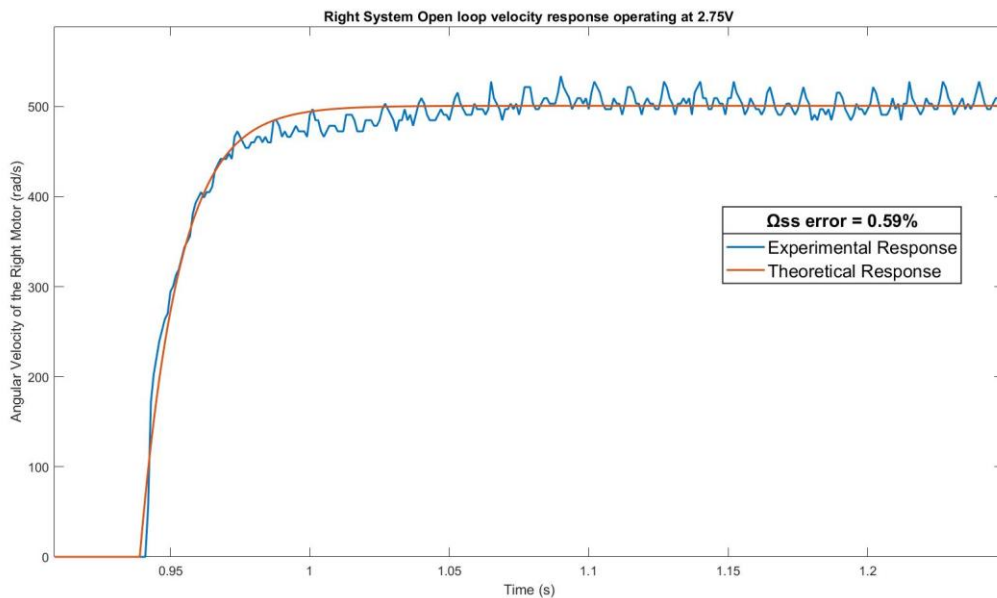
Figure 4-6.   Right master system open loop velocity response operating at 2.75V.

The responses are closely similar both during the transient and the steady state. In particular, the angular velocity steady state error between the two responses are 1.61% for the left and 0.59% for the right system, which are considered satisfactory. The discrepancies may be mainly due to the noisy readings of the encoder's pulses and due to the minor structural inconsistencies that may affect the smooth and repetitive operation of the real linear actuator. In addition, it must be taken into account that the Simulink model constitutes a simplified version of the actual master mechanism, which is based on ideal equations that can only provide an approximation of the behaviour of the real system. Lastly, note that in Figure 4-6, a repetitive high-frequency of around 160Hz (~8 peaks every 0.05 sec) appears clearly in the experimental response. In this thesis, the origin of this frequency was not identified; yet it would be interesting to further investigate the matter in the future to determine the source of this phenomenon.

4.2　Controller Design

Following the parameter identification process, in this chapter, the design of the control scheme for both the slave and the master systems is presented. Due to its complexity and vast expanse, the control scheme will be initially presented as a whole and then it will be dissected into separate divisions for further analysis.

　　Before proceeding, it should be stated that the control scheme presented in this thesis was implemented using Simulink together with the dSPACE DS1103 controller board. As will be explained in the following chapter, the dSPACE platform constitutes a powerful processing board that allows the wired communication between the slave and master systems and was utilized for the experimental tests performed in this project. However, a work towards the implementation of a wireless communication among the slave and master systems was simultaneously being carried out in the lab by the master student Petros Konstantineas. In his Thesis [7], a simplified version of the following control scheme was created and applied using two Nordic nrf5340 microcontrollers in order to examine the wireless response of the proposed Biomechatronic EPP topology.

4.2.1　Biomechatronic EPP control scheme

A diagrammatic representation of the complete control scheme is displayed in Figure 4-7, where the rationale behind the workings of the slave and master systems is revealed. It must be highlighted that even though seemingly a single control scheme is presented, in fact, three distinct control loops are incorporated and operating simultaneously:

- An *open-loop* control concerning the **slave** system (blue colour)
- A *closed-loop* control (PV controller) for the **left master** system (green colour)
- A *closed-loop* control (PV controller) for the **right master** system (red colour)
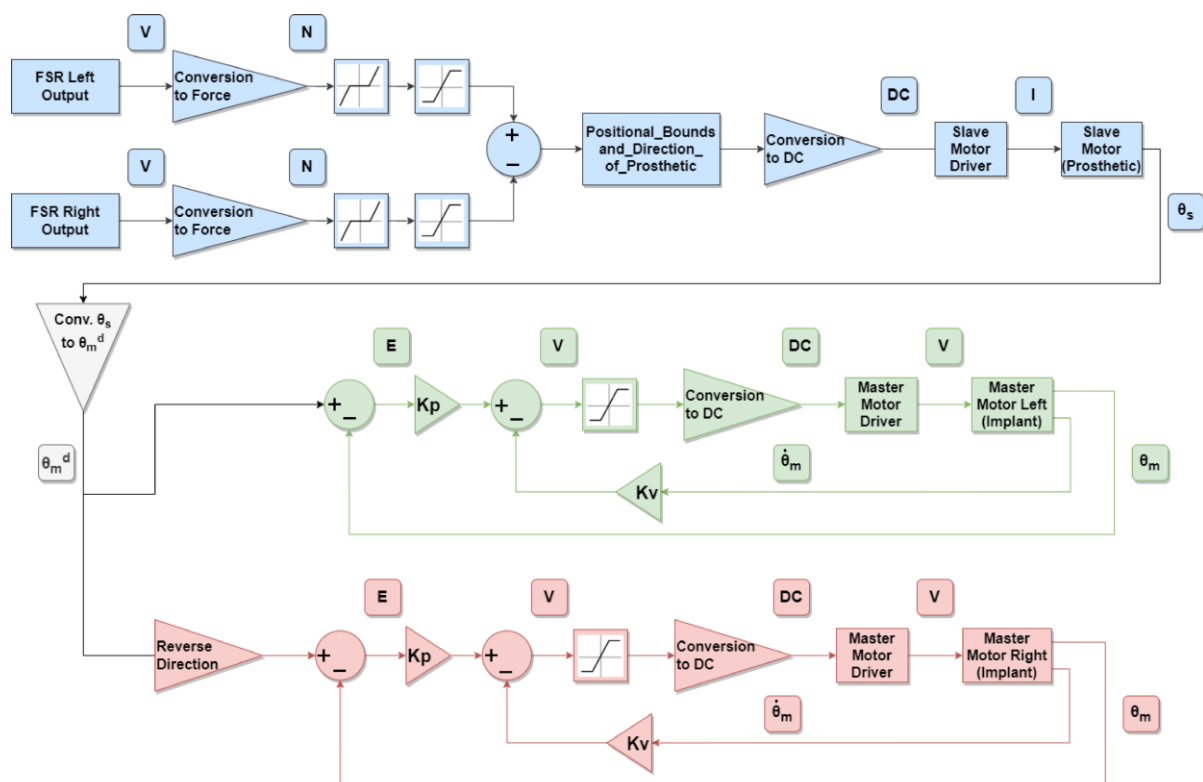
Figure 4-7.　Biomechatronic EPP control scheme.

The Biomechatronic EPP control topology architecture was explained in Chapter 2.1 and was visually illustrated in Figure 2-4. The additional value of Figure 4-7 lies in the fact that it presents an in-depth insight into how the measurements received from the various sensors (the FSRs and the encoders) are actually processed, and how the control commands are formed and passed to the actuators (slave and master motors) to achieve the desired outcome. Next, the slave and master control loops integrated into the complete Biomechatronic EPP control scheme will be separately presented in detail.

4.2.2 Slave System Open-loop Control Scheme

A closer look at the isolated open-loop control diagram of the slave system is displayed in Figure 4-8.
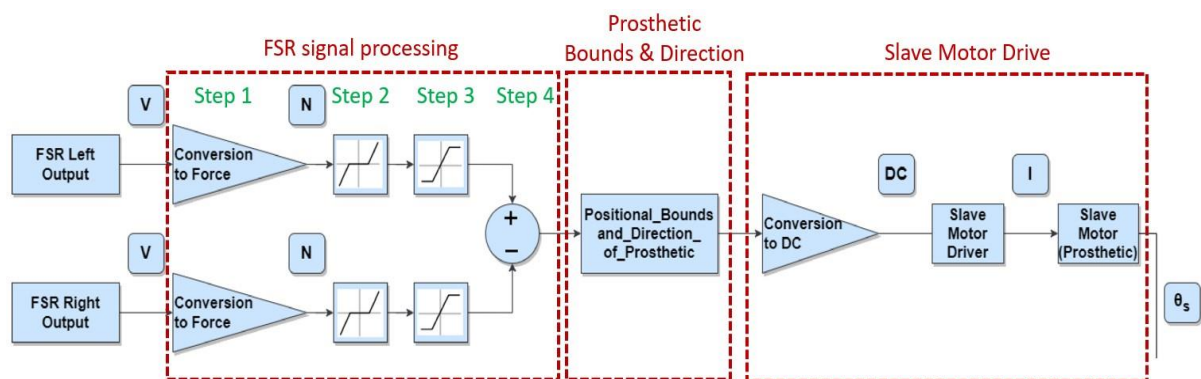
Figure 4-8.   Isolated slave system control scheme.

The whole control scheme is initiated by the signals received from the force sensors connected to the left and right master robots as shown in Figure 4-8. The output voltage of the FSR circuit (see Section 3.2.3) passes through a post-processing stage, after which the force signals are used to form the input command that will determine the current and consequently the torque of the slave system, which represents the prosthetic limb.

FSR signal processing

More precisely, the processing of the FSR measurements includes the following steps:
1. Convert the FSR circuit voltage signals (V) into force signals (N).
2. Set a lower bound (dead zone block).
3. Set an upper bound (saturation block).
4. Obtain the difference between the left and right FSR signals.

Step 1 is performed by employing Equations (3-35) and (3-36) that were obtained from the line fitting task during the FSR calibration process (see Section 3.2.3).

The need for *steps 2* and *3* can be visualized in Figure 4-9.
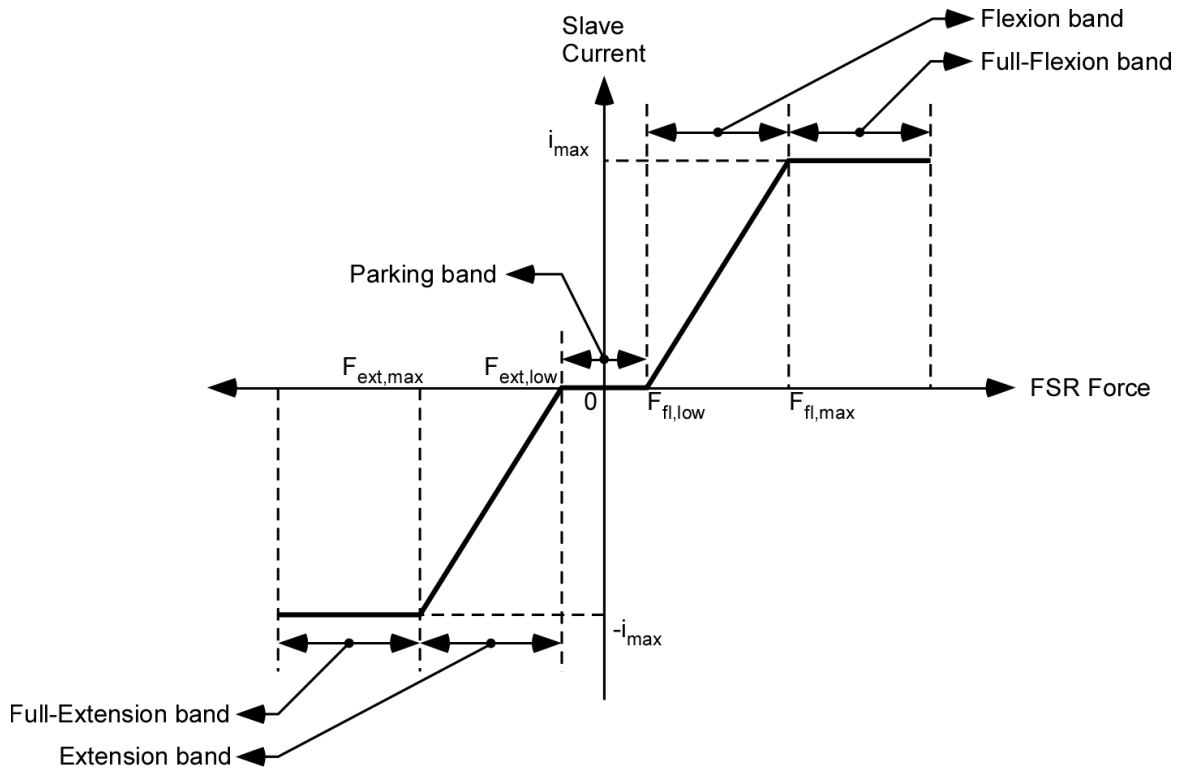
Figure 4-9.   Upper and Lower Bounds of the FSR sensor Output – Modified from [10].

Considering that ultimately the FSR values will be used to determine the current of the slave motor, Figure 4-9 illustrates the correlation among the two quantities.

On the one hand, the parking band ensures that tiny forces, residual stresses, or even noise from the force sensors will not be interpreted as genuine intention from the amputee to move the prosthetic. Therefore, low output values from the sensors do not trigger the motion of the slave system.

On the other hand, once a certain upper bound is reached, the slave motor command should remain constant. During the experiments, the upper and lower bounds must be variable and should be able to be set independently of one another, thus allowing to adjust the controller according to the preferences of the user. In this work, during the tests, the lower bounds were set equal to $F_{lowerB} = F_{fl,low} = -F_{ext,low} = 1N$ and the upper bounds equal to $F_{upperB} = F_{fl,\max} = -F_{ext,\max} = 15N$.

Step 4 constitutes a simple subtraction between the two FSR measurements, which is crucial in determining the movement of the prosthetic. This FSR signal difference F_{diff} is defined as

$$F_{diff} = F_{left} - F_{right} \tag{4-7}$$

where F_{left} and F_{right} are the force signals from the left and right FSRs respectively, after having passed through steps 1,2 and 3 of the post-processing stage.

The actual part of the Simulink model corresponding to the FSR signal processing is presented in Figure 4-10.
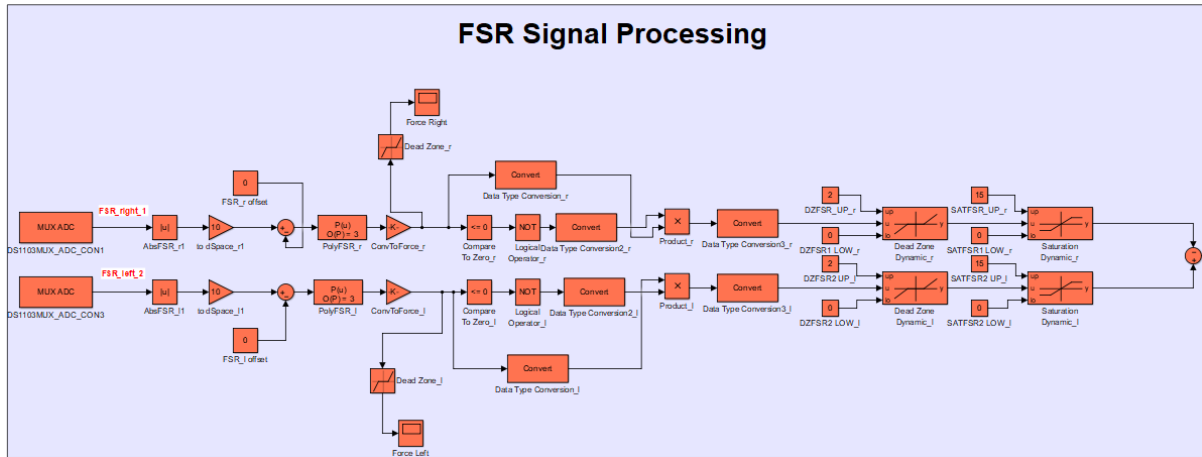
Figure 4-10. FSR Signal Processing - Simulink model.

It must be pointed out that in addition to the blocks concerning the processes described above, additional blocks can be seen in Figure 4-10. These blocks mainly concern the compatibility of the Simulink model with the DS1103 controller board and their utility is diligently described in Appendix A: dSPACE Basics of a previous Diploma Thesis [15].

Prosthetic Bounds and Direction

The output from the FSR processing stage is the force difference F_{diff} between the two force signals. This force difference has a sign and a magnitude. The sign is used to determine the direction that the slave motor should rotate. For example, a stronger signal from the left FSR will result in a force difference with a positive sign which will then give the command to the slave motor to rotate in a clockwise direction. Correspondingly, a stronger signal from the right FSR will produce an anticlockwise rotation.

Moreover, since the slave motor is intended to imitate the extension and flexion of a human wrist, appropriate positional bounds must be set. These bounds ensure that the slave motor will only receive commands to move inside the positional limits.

More specifically, if θ_f and θ_e are the boundaries of the movement in the flexion and extension bands respectively, and if θ_s is the angular position of the prosthetic limb, the following equation set is true:

$$F_{diff} > 0 \ and \ \begin{cases} \theta_s < \theta_e & clockwise \ rotation \\ \theta_e \leq \theta_s \leq \theta_f \ , & clockwise \ rotation \\ \theta_s > \theta_f & halted \end{cases}$$

$$(4\text{-}8)$$

$$F_{diff} < 0 \ and \ \begin{cases} \theta_s < \theta_e & halted \\ \theta_e \leq \theta_s \leq \theta_f \ , & anticlockwise \ rotation \\ \theta_s > \theta_f & anticlockwise \ rotation \end{cases}$$

Based on the findings of study [1], which was mentioned and explained in Section 3.1.6, during the experimental tests, the respective boundaries were set equal to $\theta_f = -45°$ and $\theta_e = 50°$.

The direction change and the set of positional bounds in Simulink are displayed in Figure 4-11 and were first implemented and explained in [14]. In this work, the same concept is adopted since the driver of the slave system remained the same.
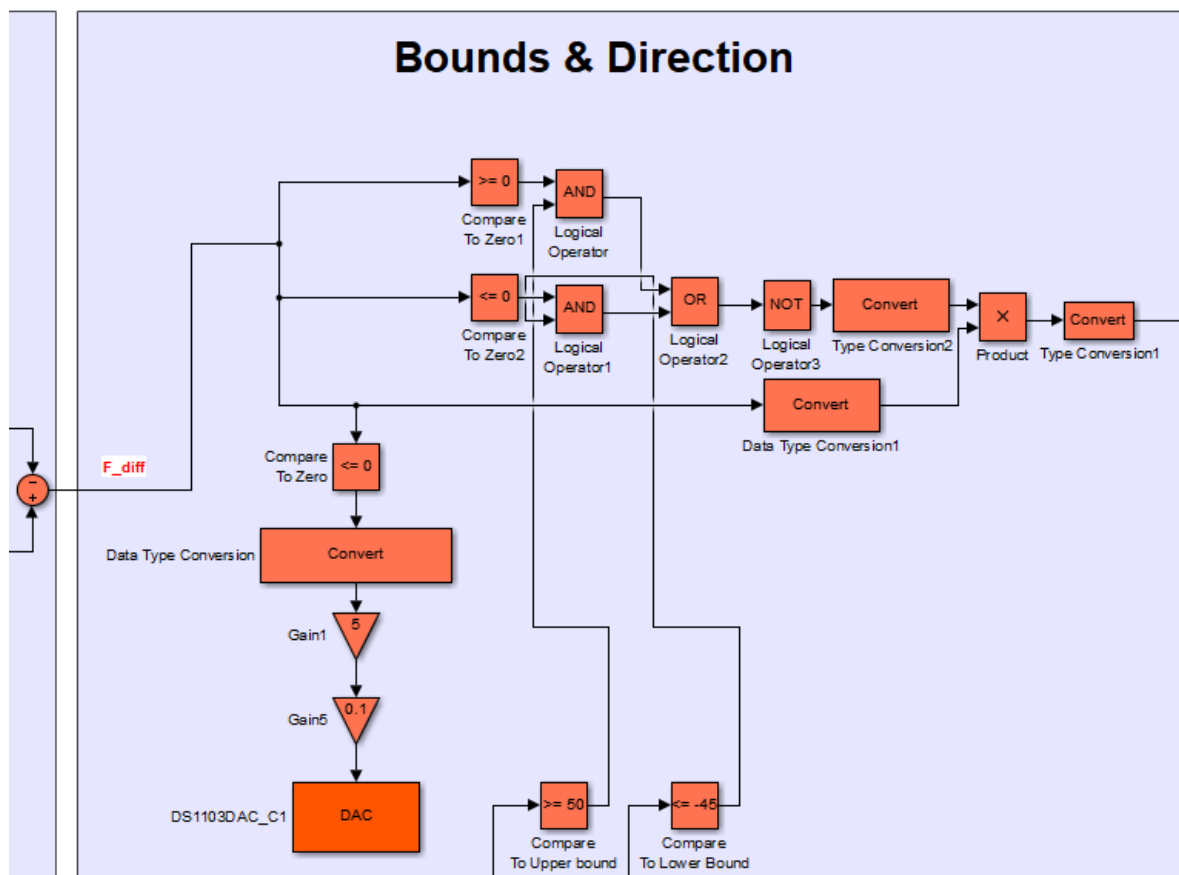
Figure 4-11. Prosthetic Bounds and Direction - Simulink model.

Slave Motor Drive

The input of the AZBDC10A4 slave driver is a PWM pulse and the output is current in PWM form. The magnitude of the current that will be directed to the slave motor depends on the Duty Cycle (which is noted as DC in Figure 4-7) of the PWM pulse, which in its turn depends on the magnitude of the FSR difference F_{diff}. Therefore, the driver's input command must be normalized. In other words, the FSR signal difference must be converted to a duty cycle range between 0 and 1. This is done by multiplying the FSR signal difference F_{diff} by $1/F_{diff_{MAX}}$, where $F_{diff_{MAX}} = F_{upperB} = 15N$ in this case.

However, due to the fact that currently, the chosen slave motor is largely oversized for this application and a duty cycle with the value of 1 would result in an over-reaction of the slave system, an FSR reduce gain had to be placed to mitigate the output current command of the driver. As a result, the duty cycle range that is actually utilized lies between 0 and 0.05.

The corresponding Simulink model is displayed in Figure 4-12.
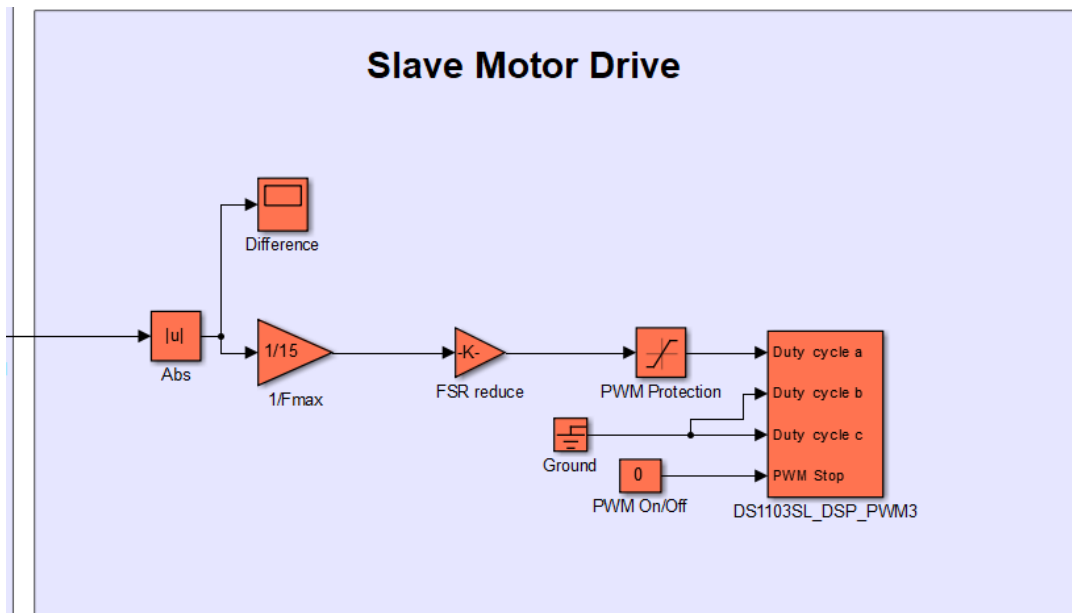
Figure 4-12. Slave Motor Drive Command - Simulink model.

With the above figure, the open-loop control scheme of the slave system was thoroughly analysed. Next, the control of the master system will be presented in detail.

4.2.3   Master System Control

The control schemes for the left and right master robots are separate but identical, and therefore only one of the two will be presented meticulously. The isolated closed-loop control diagram for the left master robot is displayed in Figure 4-13.
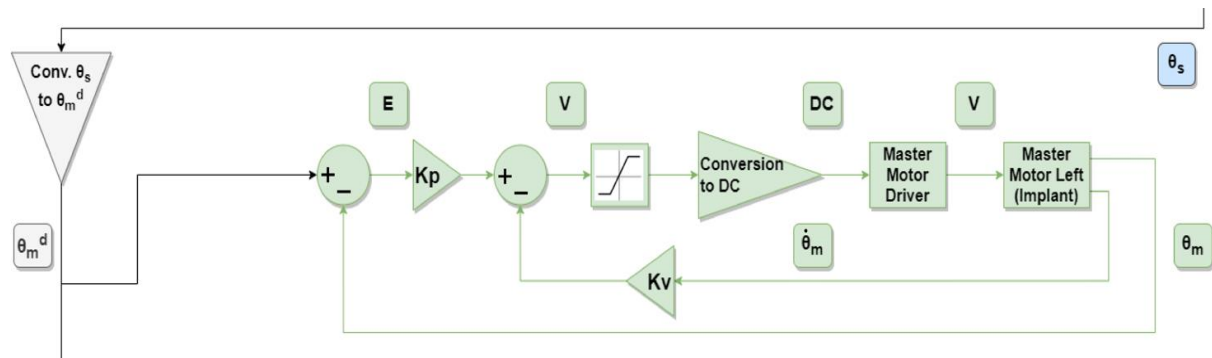
Figure 4-13. Isolated left master system control scheme.

The position response of the prosthetic limb θ_s constitutes the reference input for the master motors closed-loop controller. The aim of each master robot is to set the appropriate length of the residual muscles that corresponds to the rotation of the wrist joint, which in this application is represented by the prosthetic limb.

Proceeding the first order of business is to calculate the angular position θ_s of the prosthetic through the pulses of the slave encoder. The dSPACE platform can only measure the number of pulses of the encoder, so the following equation is used to obtain the angular position of the prosthetic:

$$\theta_s[\text{deg}] = EncPosition[counts]\frac{360°}{slave\ encoder\ counts\ /\ rev}GR_{slave} \qquad (4\text{-}9)$$

where $GR_{slave} = 343:17576$ is the gear ratio of the gearbox attached to the slave motor. Also, from the encoder datasheet, it is given that the slave encoder counts per revolution are 500.

Next, the acquired angular position of the prosthetic θ_s has to be converted into the corresponding desired master motor position $\theta_m{}^{des}$. This is done using the following formula:

$$\theta_m{}^{des}[rad] = \theta_s \frac{360°}{\theta_{range}} \frac{le_u}{l} \frac{\pi}{180} \tag{4-10}$$

where the lead screw lead l is equal to 0.4mm, the thread length of the lead screw le_u is 20mm, and the motion range of the prosthetic limb θ_{range} is 95°, see Chapter 3 also.

Figure 4-14 presents the part of the Simulink model corresponding to the conversion described above.
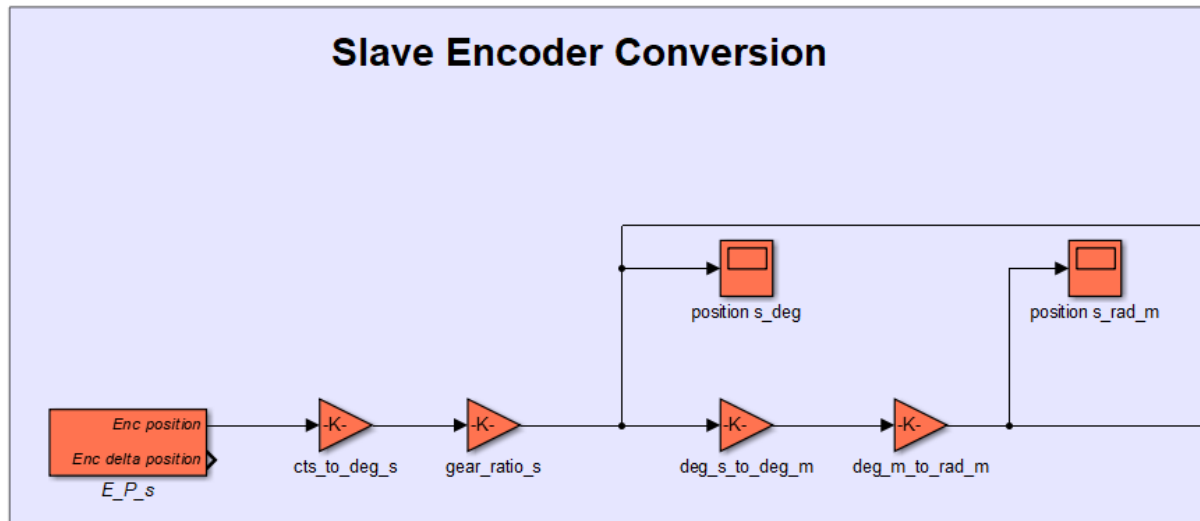
Figure 4-14. Slave Encoder Count Conversion - Simulink model.

The desired master motor position $\theta_m{}^{des}$ is then used as the command input for the master motor closed-loop PV controller. The output of a PV controller (in the case of a voltage mode control) is given by:

$$Voltage\ Command(t)[V] = K_p e(t) + K_v \dot{\theta}_m(t) \tag{4-11}$$

where $\dot{\theta}_m$ is the angular velocity of the master motor, e the positional error defined as

$$e = \theta_m{}^{des} - \theta_m \tag{4-12}$$

and K_p, K_v the position and velocity gains, respectively.

To calculate the positional error e, the input command is compared to the actual master motor angular position θ_m. As with the slave motor position, the knowledge of the master motor position θ_m is obtained from the master encoder using Equation (4-13).

$$\theta_m[rad] = EncPosition[counts] \frac{360°}{master\ encoder\ counts\ /\ rev} \frac{\pi}{180} \tag{4-13}$$

where, according to the datasheet, the master encoder counts per revolution are 256.

The velocity of the master motor is obtained in a similar fashion from Equation (4-14).

$$\theta_m[rad] = \frac{EncDeltaPosition[counts\ /\ s]}{sampling\ rate} \frac{360°}{master\ encoder\ counts\ /\ rev} \frac{\pi}{180} \tag{4-14}$$

Using the dSPACE controller board, the sampling rate was set to 1 ms during the experimental tests.

The Simulink model division corresponding to the master encoder conversion and the implementation of the PV controller is displayed in Figure 4-15.
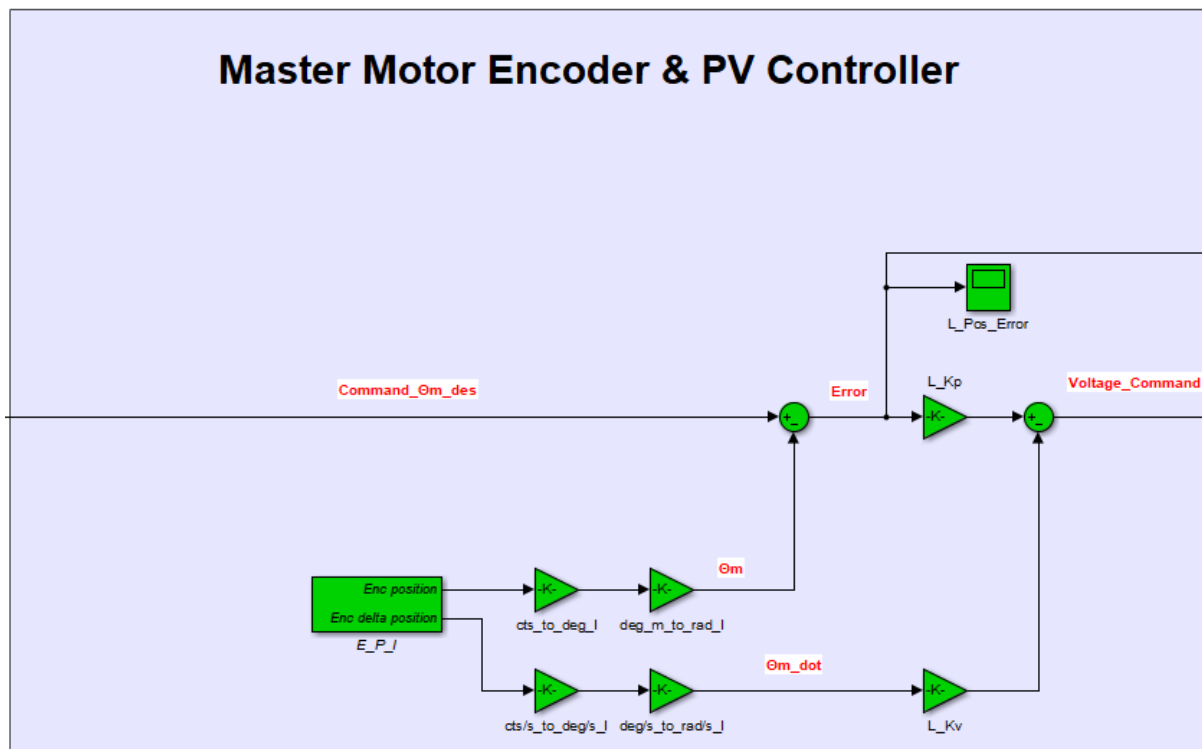
Figure 4-15. Master Encoder Count Conversion and the PV controller - Simulink model.

When designing a controller, one of the most critical tasks is determining appropriate values for the gains. To obtain an initial estimation of the gain values, the procedure described below was followed.

From Section 3.1.1, it is known that the master mechanism equation of motion can be expressed as:

$$J_{eq}\ddot{\theta}_m + B_{eq}\dot{\theta}_m = \tau_m - \tau_f \tag{4-15}$$

As mentioned in Section 3.1.5, a voltage mode control is implemented, which means that the torque τ_m of the master motor is defined as:

$$\tau_m = \frac{\mathrm{K}_T}{R_a}\left(V_a - \mathrm{K}_T\dot{\theta}_m\right) \tag{4-16}$$

In this case, the voltage V_a applied to the motor is equal to the output of the PV controller, which is given by Equation (4-11).

Combining Equations (4-11), (4-15) and (4-16) the master closed-loop equation is derived:

$$J_{eq}\ddot{\theta}_m + \left(B_{eq} + \frac{K_V K_T}{R_a} + \frac{K_T^{\,2}}{R_a}\right)\dot{\theta}_m + \frac{K_P K_T}{R_a}\theta_m = \frac{K_P K_T}{R_a}\theta_m^{\,des} - \tau_f \tag{4-17}$$

Equation (4-17) could also be written as:

$$\ddot{\theta}_m + 2\zeta\omega_n\dot{\theta}_m + \omega_n{}^2\theta_m = \omega_n{}^2\theta_m{}^{des} - \frac{\tau_f}{J_{eq}} \tag{4-18}$$

where ω_n is the closed-loop natural frequency and ζ the damping ratio.

Consequently, the gains of the PV controller could be given by the following equations.

$$K_P = \frac{\omega_n{}^2 R_a J_{eq}}{K_T} \tag{4-19}$$

$$K_V = \left(2\zeta\omega_n J_{eq} - B_{eq} - \frac{K_T{}^2}{R_a}\right)\frac{R_a}{K_T} \tag{4-20}$$

To ensure that all fast wrist movements up to 4.5 Hz will be followed by the system, a natural frequency of 140 rad/s was chosen considering that

$$f_{path_{MAX}} = 4.5\ Hz \Rightarrow \omega_{path_{MAX}} = 2\pi \cdot f_{path_{MAX}} = 28.27\ \frac{rad}{s} \tag{4-21}$$

and

$$\omega_n = 5 \cdot \omega_{path_{MAX}} \approx 140\ \frac{rad}{s} \tag{4-22}$$

Also, to achieve the fastest possible response without overshooting, a critical damping ratio was assumed.

$$\zeta = 1 \tag{4-23}$$

By substituting Equations (4-22) and (4-23) into (4-19) and (4-20), the gains for both the left and right master robots were obtained.

$$K_{P_{LEFT}} = 1.13\left[\frac{V}{rad}\right] \quad , \quad K_{V_{LEFT}} = 0.0083\left[\frac{Vs}{rad}\right] \tag{4-24}$$

$$K_{P_{RIGHT}} = 1.11\left[\frac{V}{rad}\right] \quad , \quad K_{V_{RIGHT}} = 0.0086\left[\frac{Vs}{rad}\right] \tag{4-25}$$

Even though the above gains proved to be a good initial estimation, fine-tuning of the values was implemented during the experimental tests. In particular, a slight increase of the positional gain value seemed to improve the response of the system. Also, it was observed that by reducing the damping ratio to around 0.7, the response was quicker, while the overshooting was not noticeable to the user. In conclusion, the final gain values are presented:

$$K_{P_{LEFT}}' = 1.4\left[\frac{V}{rad}\right] \quad , \quad K_{V_{LEFT}}' = 0.005\left[\frac{Vs}{rad}\right] \tag{4-26}$$

$$K_{P_{RIGHT}}' = 1.3\left[\frac{V}{rad}\right] \quad , \quad K_{V_{RIGHT}}' = 0.005\left[\frac{Vs}{rad}\right] \tag{4-27}$$

The input of the DRV8833 master driver is a PWM pulse and the output is voltage in PWM form. The magnitude of voltage that will be applied to the master motor depends on the duty cycle of the input PWM pulse, which is determined from the output of the PV controller.

Therefore, the output of the PV controller, which is in essence a voltage command, has to be converted in a duty cycle scale [0,1] in order for the command to be comprehended by the master driver.

Figure 4-16 shows the part of the Simulink model responsible for the correct interpretation of the PV controller's output command by the master driver.

The voltage command first passes through a saturation block which chops the voltage signal at a specified maximum voltage V_{max}. The chopping value represents the maximum voltage that the master motors should be subjected to during the operation of the system. From Section 3.1.3, it was stated that in the experimental phase, the maximum voltage provided to the master motors was set to 8V.

To finally obtain the Duty Cycle (DC) value that corresponds to the desired voltage command, the chopped signal is multiplied by $1/V_{max}$.
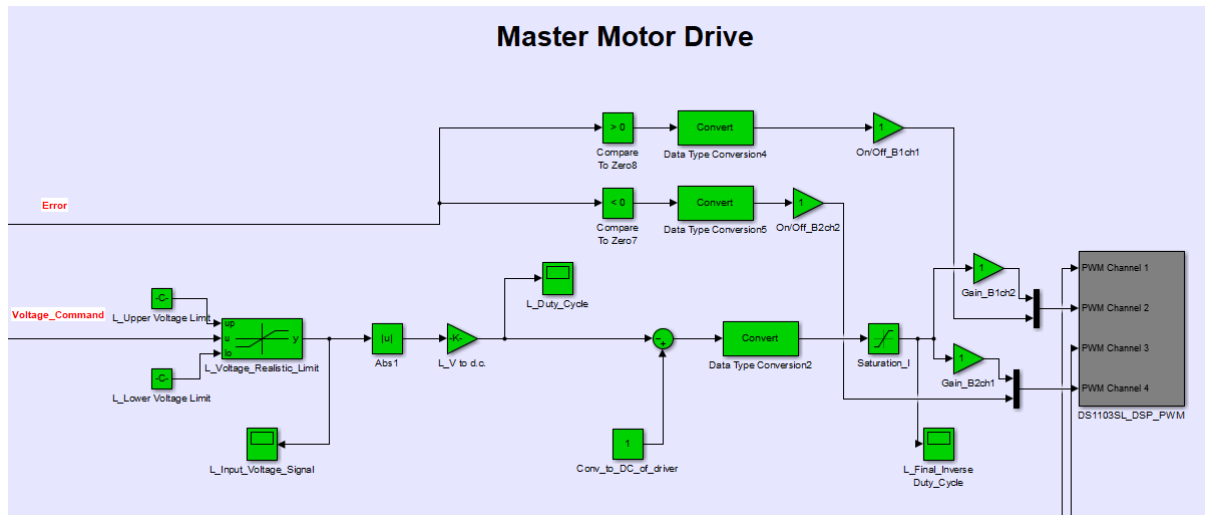
Figure 4-16. Master Motor Drive Command - Simulink model.

All the other blocks illustrated in Figure 4-16 concern how the master driver determines the direction of rotation using the positional error sign, and the fact that the driver actually utilizes the inverse of the duty cycle to produce the desired outcome. In-depth details about the workings of the DRV8833 are presented and thoroughly explained in works [8] and [7].

Lastly, the isolated control scheme for the right master motor is shown in Figure 4-17 and as mentioned previously, it is almost identical to the one of the left motor explained above. It must be pointed out, however, that the only difference is that the desired input command has the opposite sign ($\theta_{m_{LEFT}}{}^{des} = -\theta_{m_{RIGHT}}{}^{des}$), so that the lead screw nuts will move linearly in opposite directions, thus imitating the expansion and contraction of the human muscles accordingly.
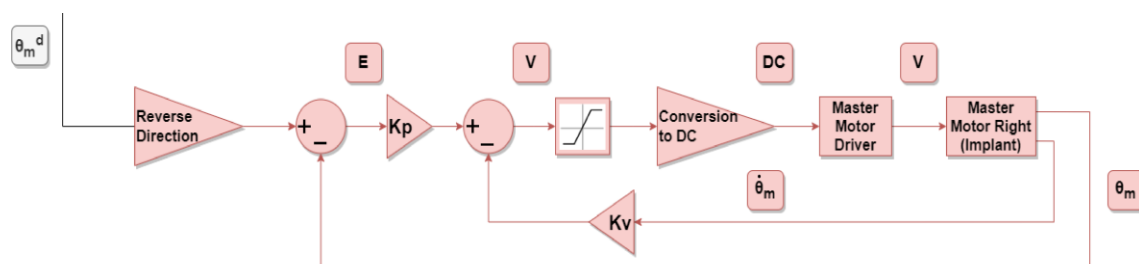
Figure 4-17. Isolated right master system control scheme.

5 Implementation

This chapter presents how the communication between the master and slave subsystems was implemented in the lab. In addition, the hardware connections and wiring diagrams for each subsystem of the setup are displayed and listed in detail.

5.1 Wired and Wireless Communication

It is evident that the proposed Biomechatrionic EPP control topology is inextricably linked with the concept of wireless communication between the master and slave subsystems. This statement derives from the fact that the master robots are intended to be placed inside an amputated arm. Therefore, inevitably, the exchange of information with the slave subsystem must be conducted through wireless communication. From previous works [11], [9], the Bluetooth Low Energy (BLE) wireless protocol was chosen as the most promising protocol to be implemented for this application. However, at the time of the conduction of this thesis, no wireless setup was ready-to-use to perform experiments. Therefore, as done in [15] and [8], the dSPACE DS1103 PPC controller board was employed once again to establish a wired connection between the master and slave.

The DS1103 is an all-rounder in rapid control prototyping. Its processing power and fast I/O are suitable for applications that involve numerous actuators and sensors. It is fully programmable from the Simulink block diagram environment and all I/O can be configured graphically using the dSPACE's Real-Time Interface (RTI). Through the corresponding software ControlDesk 5.6, new control functions can be tested and several parameters can be observed in real-time, thus facilitating the experimental procedure. A mini-manual containing instructions on how to use the hardware and software is presented in Appendix A: dSPACE Basics in [15].

At this point, it has to be mentioned that implementing a wired instead of a wireless setup was not directly obstructing the course of the current thesis since its purpose was predominantly to examine the adequacy of the newly constructed master system. However, it was clear that the project's ultimate goal was to test the whole system under wireless communication, which would constitute a far more realistic approach to the actual application. As mentioned in Chapter 4, the development of a wireless implementation was concurrently examined in the lab by Petros Konstantineas, who suggested using two Nordic nrf5340 microcontrollers to serve as the master and slave microcontrollers.

Therefore, even though the system was tested using the dSPACE platform in this work, the system's circuitry was designed and tailored based on the capabilities of Nordic's nrf5340 microcontroller. For example, the FSR circuit was designed so that the maximum output voltage would be 3V. This value constitutes the maximum input voltage that the nrf5340 microcontroller can measure and not the maximum input voltage that the DS1103 board can handle. The complete list of the microcontroller's capabilities and its suitability with the system are provided in [7].

5.1.1 Remodeling of the setup

The selection of new electromechanical components meant that the previous hardware connections had to be altered. This constituted one of the most arduous tasks to be carried out in this thesis, as the existing setup was not as straightforward as possible. In Figure 5-1, the setup received from previous works is displayed.
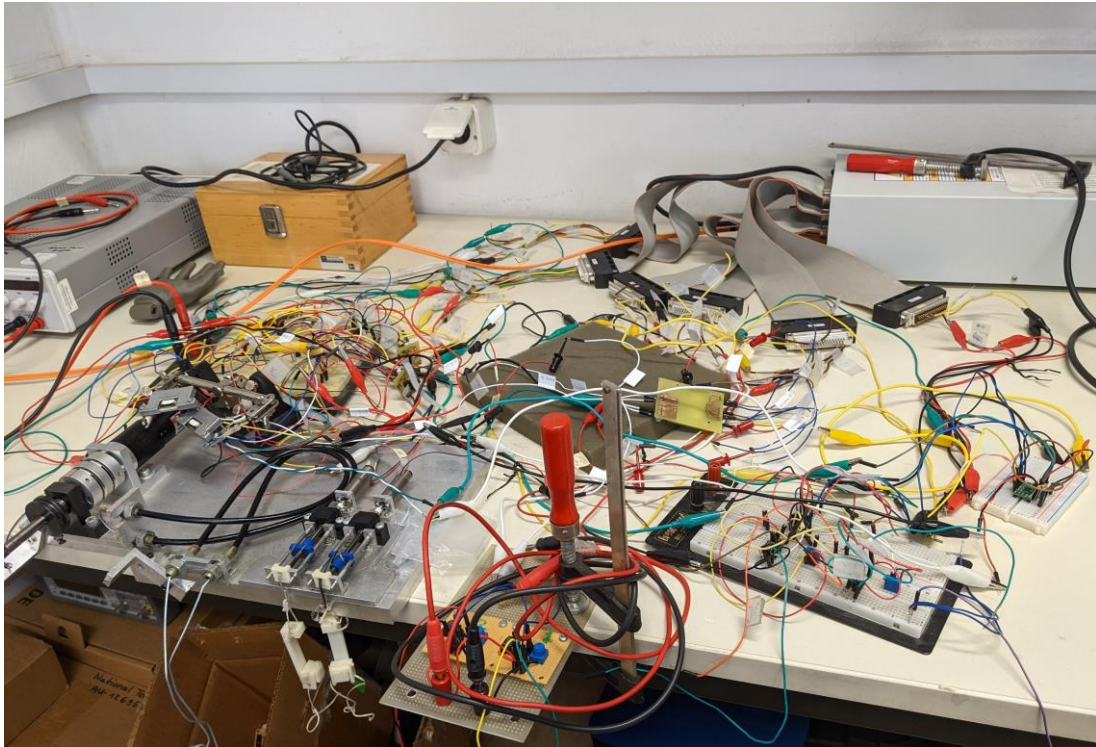
Figure 5-1.   View of the setup before remodeling.

Based on the complexity shown in Figure 5-1, a radical remodeling of the setup was considered necessary in order for the project to progress. After hours of disentanglement and careful integration of the newly selected components, the setup currently used in the lab is presented in Figure 5-2.
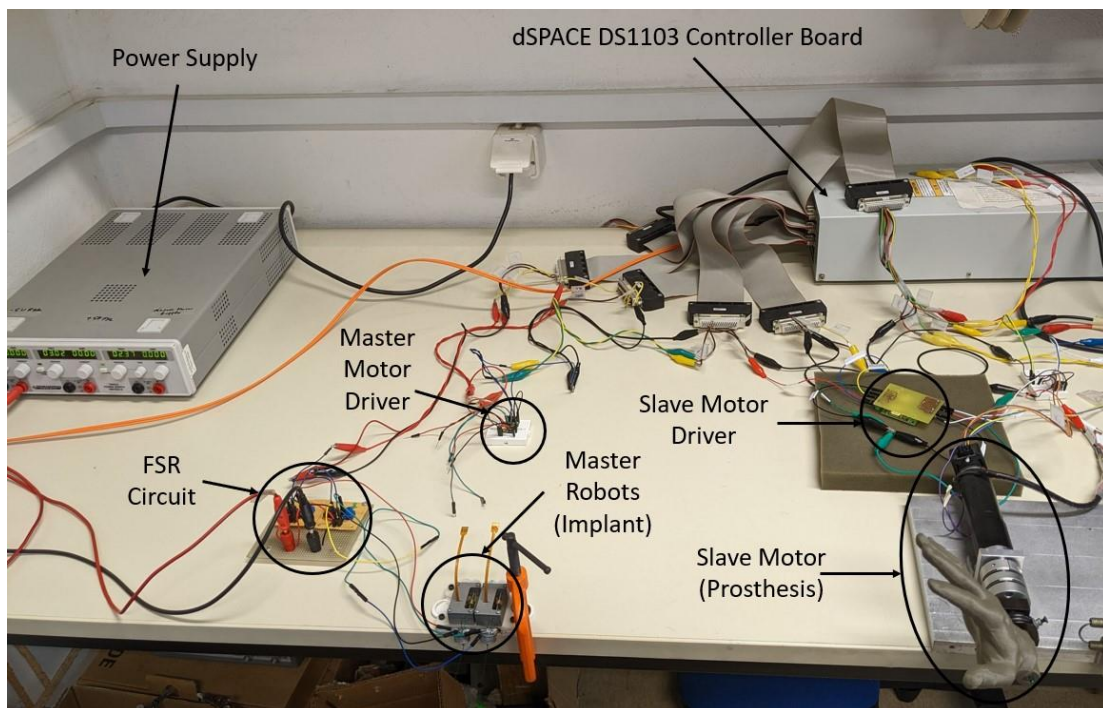
Figure 5-2.   View of the setup after remodeling.

In Figure 5-2, the main parts of the setup are circled and named. Note that the cables employed were labeled appropriately to avoid future confusion and possible connectivity mistakes.

5.2 Hardware Connections

This section presents tables and wiring diagrams to portray a complete picture of the setup's hardware connections. The setup can be split into three main subsystems. The first one concerns the prosthesis (slave), the second one the implant (master) and the third one the FSR sensors.

5.2.1 Slave subsystem

Figure 5-3 presents the wiring diagram of the slave subsystem, which involves the slave motor, the slave encoder, the slave motor driver and their respective connections with the DS1103 Pins and the power supply.
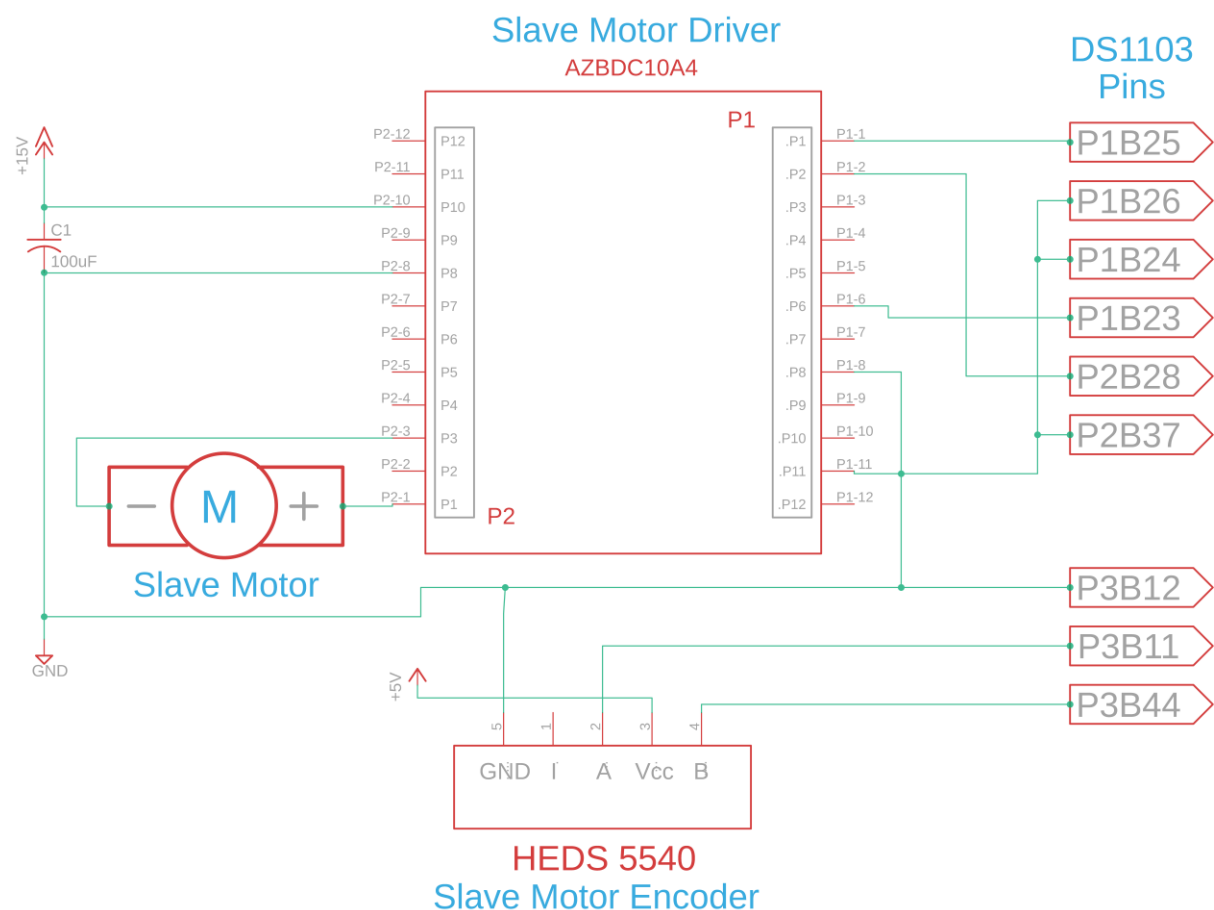
Figure 5-3.   Slave subsystem wiring diagram.

For further clarification, Table 5-1 and Table 5-2 present the connectivity map of the driver and the encoder, respectively.

A few clarifications must be made:
- All the power and signal grounds are common for all the subsystems in the setup.
- The DS1103 pins P1B26, P1B24 and P2B37 are ground pins.
- There is a 100uF decoupling capacitor between Pins 10 and 8.

Table 5-1.   Analog Servo Drive AZBDC10A4 connectivity map.

a/a	Hardware Pin	DS1103 Pins/Power Supply
Analog Servo Drive AZBDC10A4 Mapping		
1	P1 – Pin 1	P1B25(DACH1)
2	P1 – Pin 2	P2B28(SPWM1)
3	P1 – Pin 6	P1B23(ADCH17)
4	P1 – Pin 8	Signal Ground
5	P1 – Pin 11	Signal Ground
6	P2 – Pin 1	Motor Phase 1 (+)
7	P2 – Pin 3	Motor Phase 2 (-)
8	P2 – Pin 8	Power Supply(GND)
9	P2 – Pin 10	Power Supply(+15V)

Table 5-2.   Encoder HEDS 5540 500 Counts per turn connectivity map.

a/a	Hardware Pin	DS1103 Pins/Power Supply
Encoder HEDS 5540		
1	Pin 1- GND	P3B12(GND)/Ground
2	Pin 2-Index	-
3	Pin 3-Channel A	P3B11(PHI0(3))
4	Pin 4- Vcc	Power Supply(+5V)
5	Pin 5 – Channel B	P3B44(PHI90(3))

5.2.2 Master subsystem

The master subsystem includes the master motor driver and the two FPC cable adaptors that connect the master motors and encoders with the driver, the DS1103 Pins and the power supply. Table 5-3, Table 5-4 and Table 5-5 present the connectivity maps of the master motor driver and the left and right master encoders, respectively.

Table 5-3.   DRV8833 Dual Motor Driver Carrier connectivity map.

a/a	Hardware Pin	DS1103/Power Supply/Adaptors
DRV8833 Dual Motor Driver Carrier		
1	Pin 1 – GND2	Ground
2	Pin 3 - BIN1	P2B29(SPWM7)
3	Pin 4 - BIN2	P2B13(SPWM9)
4	Pin 5 - AIN2	P2A27(ST2PWM)
5	Pin 6 - AIN1	P2A29(SPWM8)
6	Pin 9 – GND1	Ground
7	Pin 10 - Vin	Power Supply(+8.3V)
8	Pin 11 - BOUT1	Left Adaptor Pin 1 - Left Master Motor (-)
9	Pin 12- BOUT2	Left Adaptor Pin 2 - Left Master Motor (+)
10	Pin 13 - AOUT2	Right Adaptor Pin 2 - Right Master Motor (-)
11	Pin 14 - AOUT1	Right Adaptor Pin 1 - Right Master Motor (+)

Table 5-4.   Encoder – ENX 8 MAG 256IMP connectivity map for Left Master Motor.

a/a	Hardware Pin	DS1103 Pins / Power Supply/Adaptors
Encoder – ENX 8 MAG 256IMP (Left Master Motor)		
1	Right Adaptor Pin 4 - GND	Ground
2	Right Adaptor Pin 5 - Vcc	Power Supply (+3.3V)
3	Right Adaptor Pin 6 - Channel A	P3B10(PHI90(2))
4	Right Adaptor Pin 7 - Channel B	P3B26(PHI0(2))

Table 5-5.   Encoder – ENX 8 MAG 256IMP connectivity map for Right Master Motor.

a/a	Hardware Pin	DS1103 Pins / Power Supply/ Adaptors
Encoder – ENX 8 MAG 256IMP (Right Master Motor)	
1	Right Adaptor Pin 4 - GND	Ground
2	Right Adaptor Pin 5 - Vcc	Power Supply (+3.3V)
3	Right Adaptor Pin 6 - Channel A	P3B25(PHI90(1))
4	Right Adaptor Pin 7 - Channel B	P3B41(PHI0(1))

Figure 5-4 presents the wiring diagram of the master subsystem.
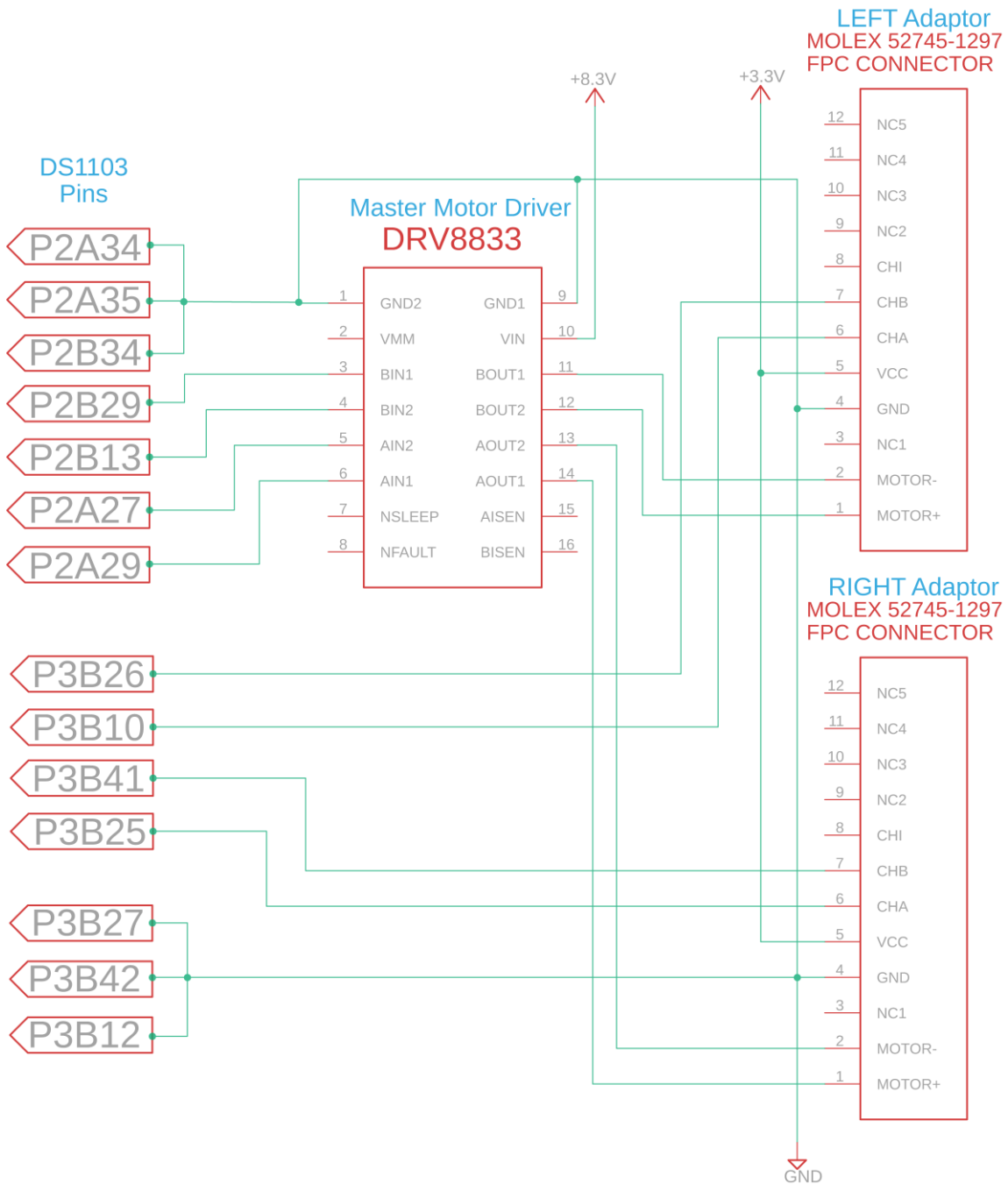
Figure 5-4.   Master subsystem wiring diagram.

The DS1103 pins P2A34, P2A35, P2B34, P3B27, P3B42 and P3B12 constitute ground pins and are connected to the rest of the ground setup.

5.2.3 FSR subsystem

The FSR circuitry is the simplest of the three subsystems since it involves only the FSR sensors, two variable resistors and two operational amplifiers. The connection with the DS1103 pins and the power supply is displayed in Figure 5-5.
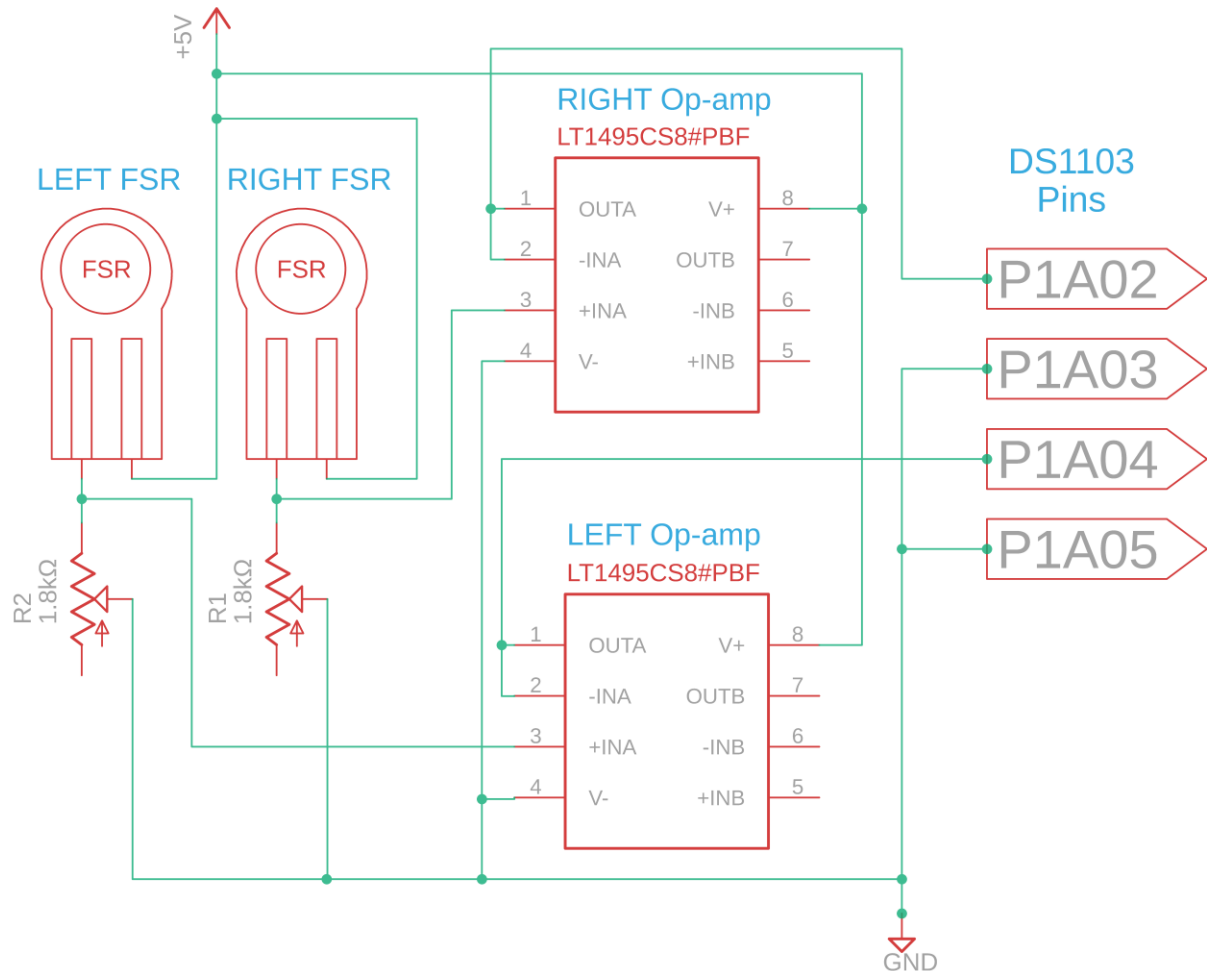
Figure 5-5.   FSR subsystem wiring diagram.

The DS1103 pins P1A03 and P1A05 are also ground pins and the corresponding connectivity map is given in Table 5-6.

Table 5-6.   FSR Circuit connectivity map.

FSR Circuit		
a/a	Hardware Pin	DS1103 Pins / Power Supply
1	Left Op-amp Pin 1 - OUTA	P1A04(ADCH10)
2	Left Op-amp Pin 4 – V-	Ground
3	Left Op-amp Pin 8 – V+	Power Supply (+5V)
4	Right Op-amp Pin 1 - OUTA	P1A02(ADCH04)
5	Right Op-amp Pin 4 – V-	Ground
6	Right Op-amp Pin 8 – V+	Power Supply (+5V)

6   Experimental Tests

Following the creation of the miniaturized master system, the control scheme design, and the wired implementation with the dSPACE platform, there was a need to study the characteristics and adequacy of the newly selected components that comprise the master robots. This chapter presents the experimental phase of putting the new implant and the proposed Biomechatronic EPP control topology to the test.

6.1   Experimental Setup

To perform any kind of test in the lab, firstly, a setup had to be created that would allow the imitation of the loading scenarios that the master implant would be subjected to if it was actually placed inside an amputated arm.

For this reason, inspired by a setup design used for experiments in [8], the following improved setup configuration was constructed (see Figure 6-1 and Figure 6-2).
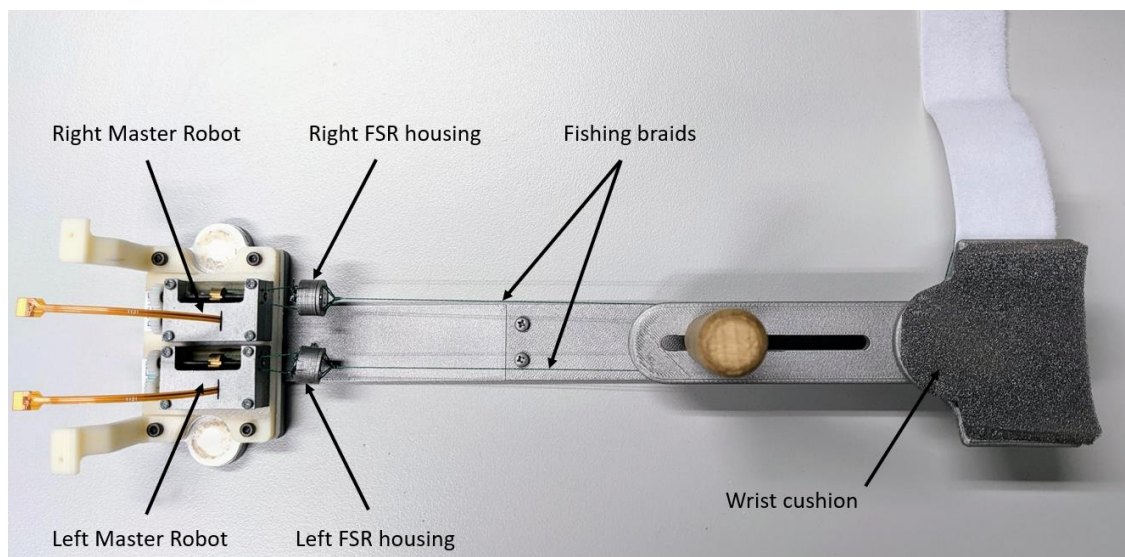
Figure 6-1.   Experimental setup parts (top view).
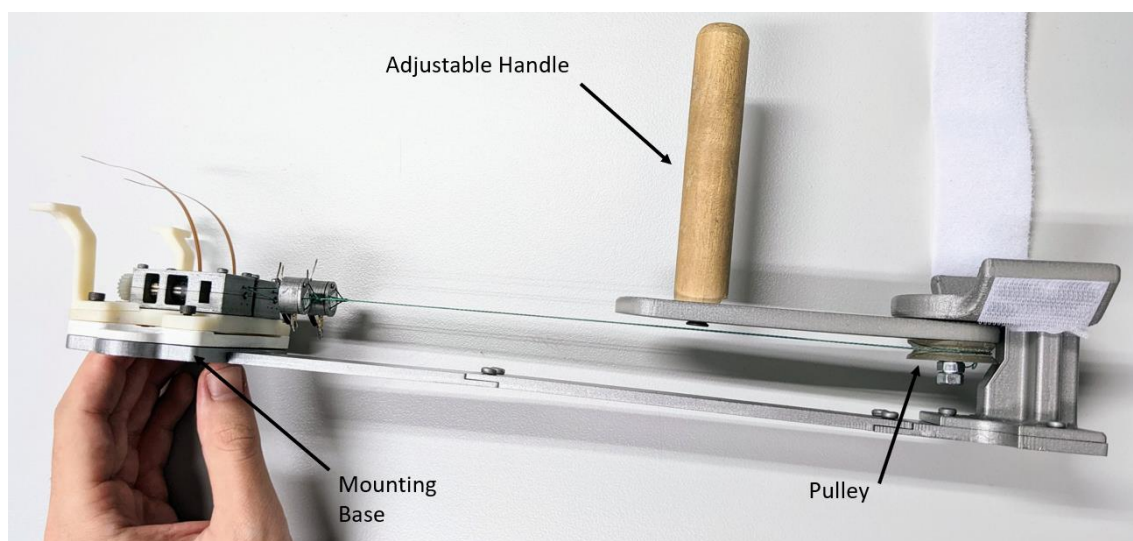
Figure 6-2.   Experimental setup parts (side view).

The structure was designed entirely in Solidworks and 3D-printed in the lab. The main parts are:

- A base where the two master robots are mounted with screws.
- A pulley acting as a rotational joint and thus representing a simplified version of a human wrist joint.
- An adjustable handle (connected to the pulley) that the user can rotate to transfer the intention to flex or extend the prosthetic limb.

The base part is located at a fixed distance from the pulley, thus ensuring that the fishing braids connecting the FSRs to the pulley are stretched constantly. More specifically, the above setup is supposed to work as follows:

First, the user has to grab the handle and adjust it so that the wrist is comfortably placed on the cushion above the pulley. Then, as shown in Figure 6-3 presented below, if the user attempts to flex or extend the wrist, the pulley connected to the handle will be forced to rotate. Consequently, one of the two fishing braids attached to the pulley will be tightened, thus pressing the corresponding FSR's surface with the help of the FSR housing parts (see Section 3.2.2). Afterward, the picked-up force signal initiates the control scheme presented in Section 4.2.1. As a result, the slave system (prosthetic limb) performs a movement depending on the slave's open-loop current mode control scheme. Subsequently, employing a closed-loop voltage mode control, the master mechanisms will have to linearly displace their lead screw nuts to follow the angular position of the slave. Hence, the pulley of the setup will be able to rotate and allow the user to indeed flex or extend the wrist as initially intended. This way, the user's wrist will have the same angular position as the prosthetic's. This means that the user's actual agonist and antagonist muscles responsible for the flexion and extension of the wrist will be displaced by a certain amount, and, therefore, the user will be able to "feel" the position of the prosthetic limb at any given moment, without requiring visual feedback. This, in a sense, is what will reinstate the proprioceptive ability of the amputee in the actual application and it is precisely what the proposed Biomechatronic EPP control topology strives to achieve through the implantable device.
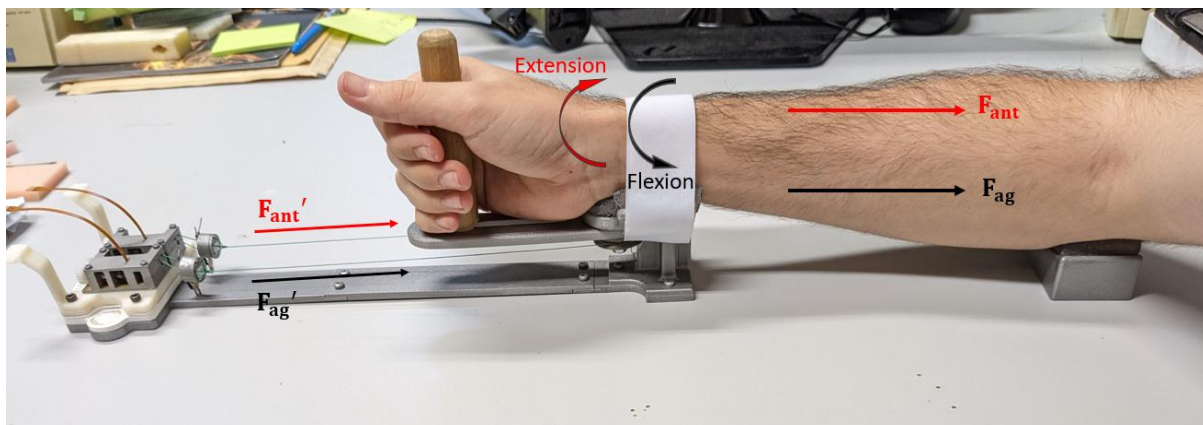
Figure 6-3. Setup function concept of flexion (black arrows) and extension (red arrows) of the wrist.
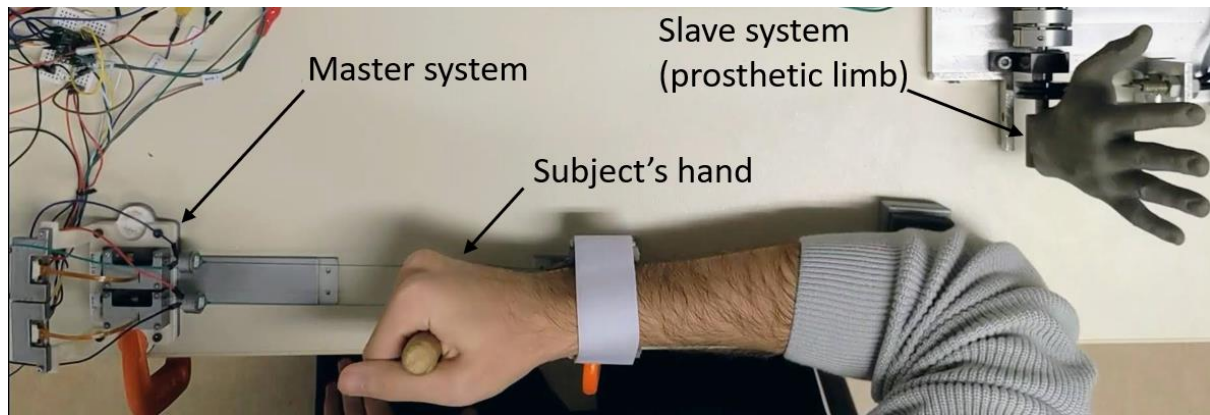
Figure 6-4.   Experimental setup integrated with DS1103 alongside the slave system.

It must be stated that, obviously, the workings of the setup described above cannot fully represent the real scenario of the implantable device. However, in terms of response demands solely from the master robot's point of view, the aforementioned setup can be considered a more challenging scenario than the real application. This is because for the pulley actually to rotate, the two separate master robots have to almost completely synchronize their responses; otherwise, the wrist motion will either not be smooth or not occur at all. On the other hand, in the real application, the residual muscles will be independent and therefore, slight discrepancies between the two master robots will probably not affect the overall outcome. This is, of course, an assumption that until tested cannot be evaluated.

Nevertheless, it should also be taken into account that the powerful DS1103 controller board was employed for the communication between the slave and master systems and the implementation of the control scheme. This fact greatly facilitates the system's overall operation, and most significantly, it eliminates the time delays that wireless communication would introduce. As mentioned in previous chapters, wireless communication was the topic of interest in a prior master thesis [7]. In this thesis, however, the focus is directed to the selected components that comprise the master mechanisms. The primary goals of the experiments are to determine whether the newly formed miniaturized master system can cope with the forces exerted by the wrist muscles and reliably and accurately follow the position of the prosthetic limb without significant deviations or steady-state errors. In addition, the power consumption of the system is also examined, while the last experiment, namely, the sense experiment, explores the ability of the Biomechatronic EPP control topology to provide feedback to the user regarding the forces applied from and to the prosthetic limb by objects in the surrounding environment.

6.2   Response - Transparency Experiment

The purpose of the first experiment was to examine the general response of the master system and the transparency of the Biomechatronic EPP control topology. As mentioned in the first chapter, a topology is called transparent only in the case where the impedance of the environment is the same for the user as if he or she was controlling the slave motor without the master [15]. Therefore, the aim was to determine whether correct information is transferred rapidly and reliably between the master and the slave and whether the miniaturized mechanical system, in combination with the closed-loop PV controller, can sufficiently track and follow the movement of the slave.

6.2.1 Procedure

During the response experiment, random wrist flexion and extension movements were performed using the experimental setup presented above. Simultaneously, using the dSPACE platform and the ControlDesk software, the following parameters were recorded:

- Angular position of the slave motor (prosthetic limb)
- Angular positions of the master motors
- FSRs circuit output voltage (thus, by extension, the forces applied to the FSRs)
- Master driver duty cycle (voltage command)
- Slave driver duty cycle (current command)

Figure 6-5 offers a glimpse of the ControDesk software environment, where some of the above parameters are shown to be recorded in real-time during the conduction of a test.
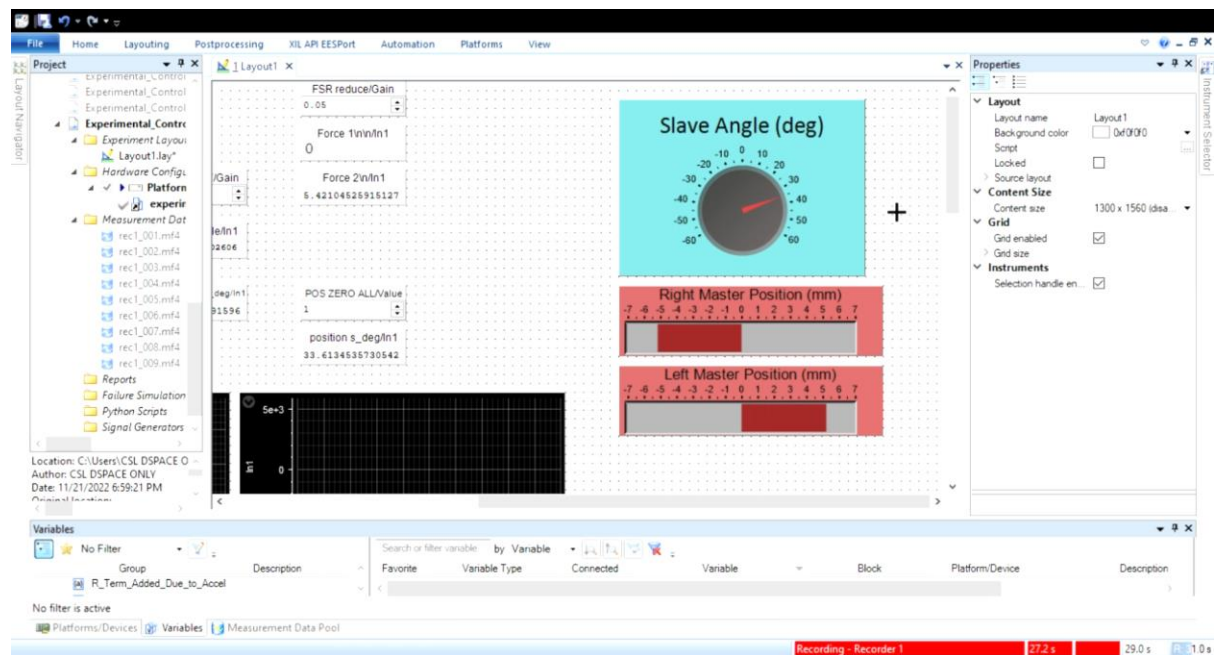
Figure 6-5.   ControlDesk environment recording parameters for the response test.

Over 50 trials of both slow and rapid movements were conducted. Since this constituted the first experiment, during the tests, multiple adjustments regarding the function of the master system were applied. The most notable ones were the following.

Adjustment 1: Slight changes to the closed-loop control scheme of the master motors and fine-tuning of the PV controller gains.

The control scheme presented in Section 4.2 had to undergo many changes before it was finalized. Initially, the force signals from the FSRs were inserted as a known disturbance to the closed-loop system, as conceptually displayed in Figure 6-6. This was done to enhance the voltage command directed to the master motors in cases where the forces applied to the mechanisms were significant.
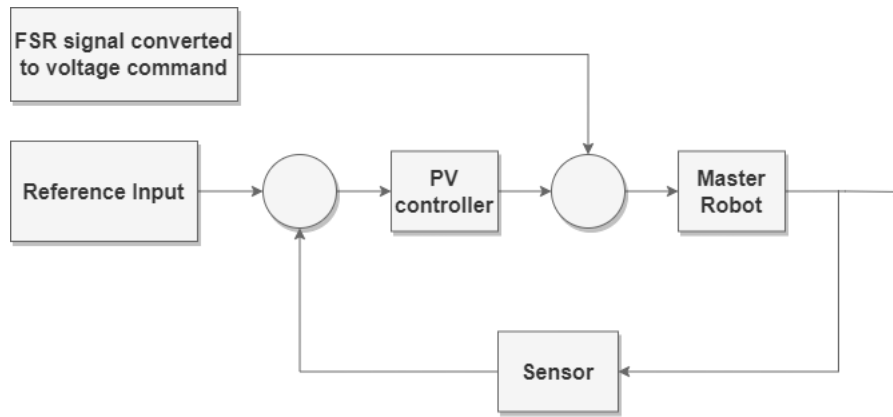
Figure 6-6. Block diagram representing the FSR disturbance integration to the master closed-loop control scheme.

However, the measured FSR signals proved to be quite noisy with sudden fluctuations (see Figure 6-7) and as a result, the voltage command was rapidly changing inside the control scheme. During the initial tests, this was also obvious by the erratic acceleration of the master motors that indicated abnormal functionality.
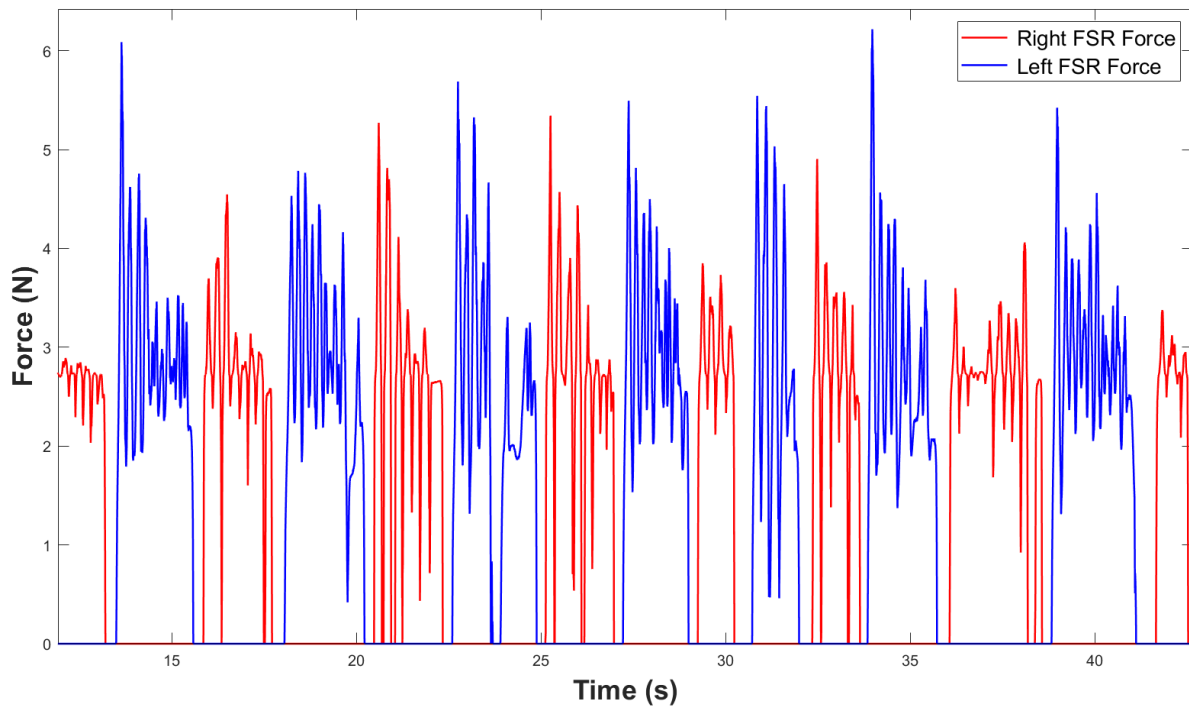
Figure 6-7. Force signals (after line fitting) received from the FSRs during a test.

To confront the issue, a possible solution would be to introduce appropriate filters in the Simulink model to obtain a better-quality signal. This strategy was extensively examined in [15] and the conclusion was that the use of filters would introduce considerable delays to the system, which would exacerbate the response instead of proving beneficial. Consequently, it was decided to remove the involvement of the FSR measurements from the master closed-loop control scheme (this means that the FSR measurements were used only for the open-loop control scheme of the slave motor). Rather, to achieve a more instantaneous response and boost the available torque provided to the master motors, the position gain K_p was slightly

increased while the velocity gain K_v was moderately reduced. The exact gains' values determined after fine-tuning were presented in Section 4.2.3.

Adjustment 2: Increase of the master motor driver's operating voltage. Ideally, the operating voltage of the driver corresponds to the maximum reference voltage for the master motors. In other words, if the duty cycle command of the driver is equal to 1, the voltage applied to the motors (reference voltage) should be equal to the operating voltage.

Initially, the driver's operating voltage was set to 6V. However, during the tests, it seemed that when high-magnitude forces were exerted, the master system was unable to overcome the external loading. After further inspection, it was observed that due to additional resistance introduced by the various jumper cables that intervened between the motors and the driver in the setup, and due to power losses from the motor driver, the maximum stall current drawn by the master motors could not produce sufficient torque to overcome the external loading with ease. By increasing the operating voltage to 8.3V, the response vastly improved, and it was decided to use this value as the reference voltage for all the experiments.

The master motors' stall current corresponding to the operating voltage of 8.3V was measured around 0.40 A. Even though this is beyond the maximum continuous current (0.20 A based on the motor's datasheet) it did not seem to cause the master motors to overheat. This can be attributed to the intermittent and short-term nature of the application and the fact that the stall current was rarely reached during the operation of the system.

6.2.2 Results

Following the implementation of the adjustments described above, in this section, the position response of the system and the various recorded parameters will be presented.

Figure 6-8 and Figure 6-9 display the linear position responses of the left and right master lead screw nuts, respectively, as recorded during one of the tests.
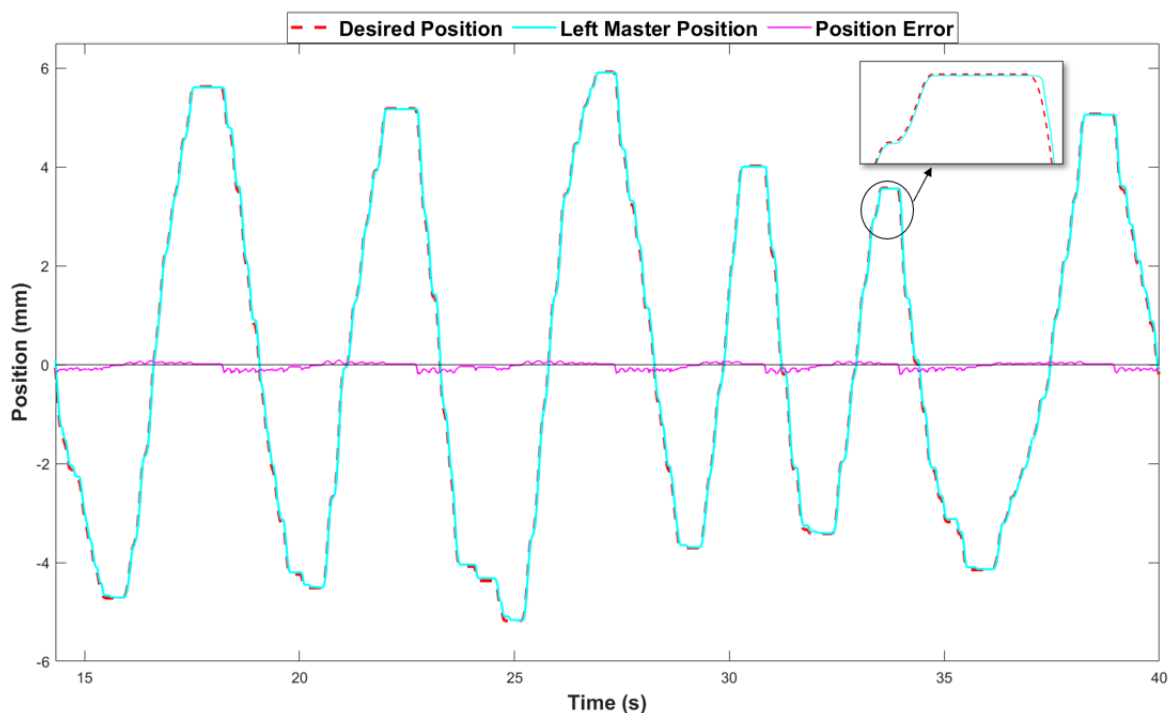
Figure 6-8.   Left Master Position Response.
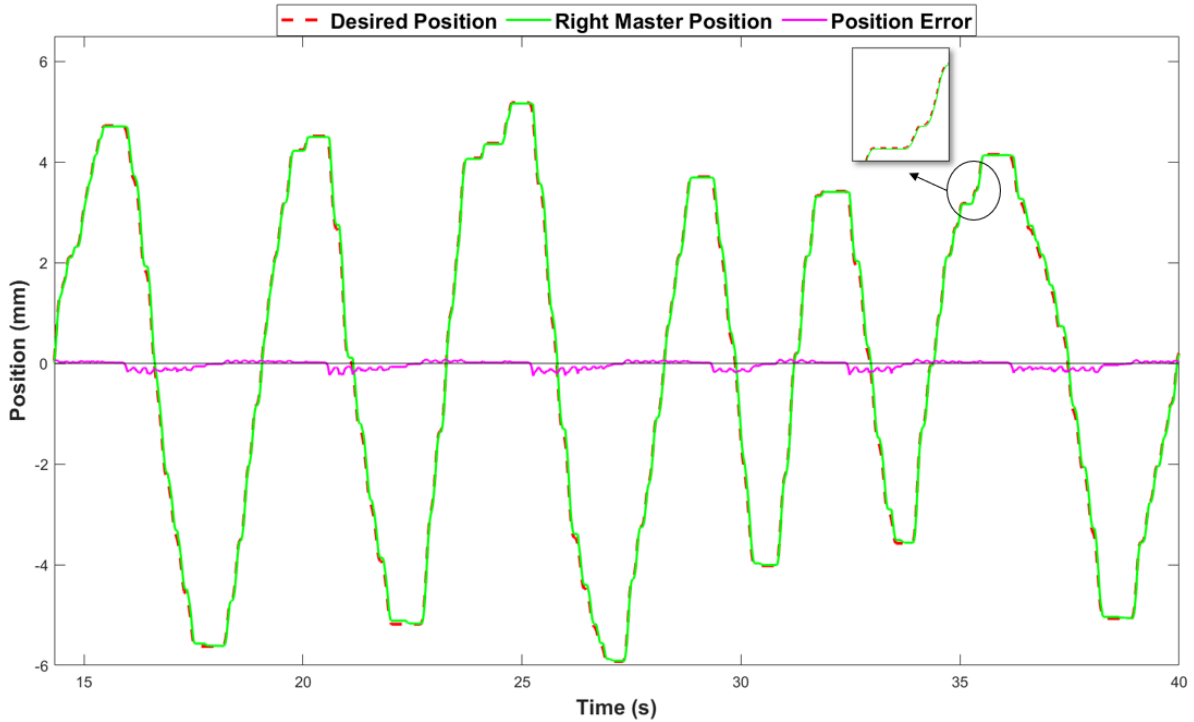
Figure 6-9.   Right Master Position Response.

The vertical axis indicates the linear displacement of the lead screw nut in millimetres, while the horizontal axis shows the elapsed time in seconds. As the legends of the Matlab graphs state, the cyan and green curves correspond to the positions of the left and right nuts. It is reminded that the correlation between the linear position x_n of the lead screw nut and the angular position θ_m of the master motor is given by the following equation.

$$x_n[mm] = \theta_m[rad]\frac{l}{2\pi}\frac{1}{n} \tag{4-28}$$

where l is the lead of the lead screw and n the gear ratio of the linear actuator.

Even though with the help of the motors' encoders the parameter measured and used in the control loop is the angular position of the motors, for the analysis of the responses, it is more sensible to study the linear position using Equation (4-28). Therefore, in both graphs, the red coloured dashed curve represents the position of the slave (prosthetic) converted to the corresponding desired linear position for the nuts. In other words, it constitutes the linear reference input for the closed-loop control for each motor. Lastly, the error between the desired and the actual position of the master robots is illustrated by the magenta coloured curve.

The maximum instant positional error during the tests was 0.15 mm, while the average positional error was around 0.08 mm. This result is considered more than satisfying for the needs of this particular application.

Figure 6-10 and Figure 6-11 show a close-up part of the previous position responses for further analysis.
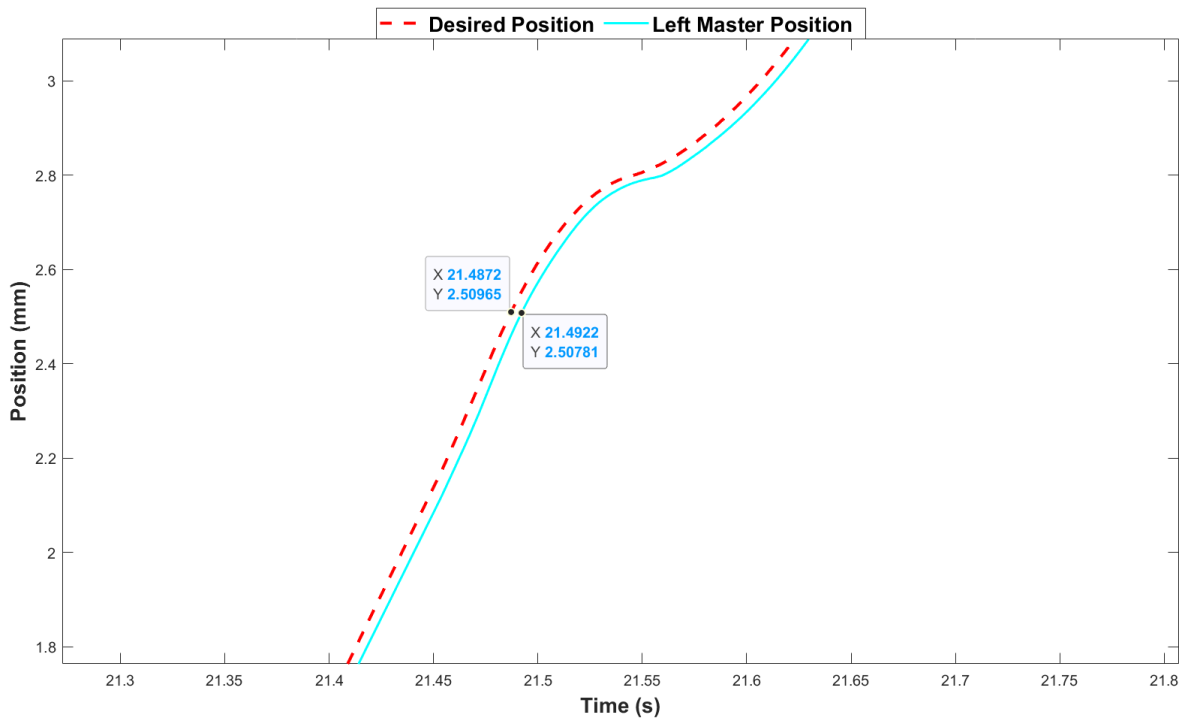
Figure 6-10. Left Master Position Response Close-up.
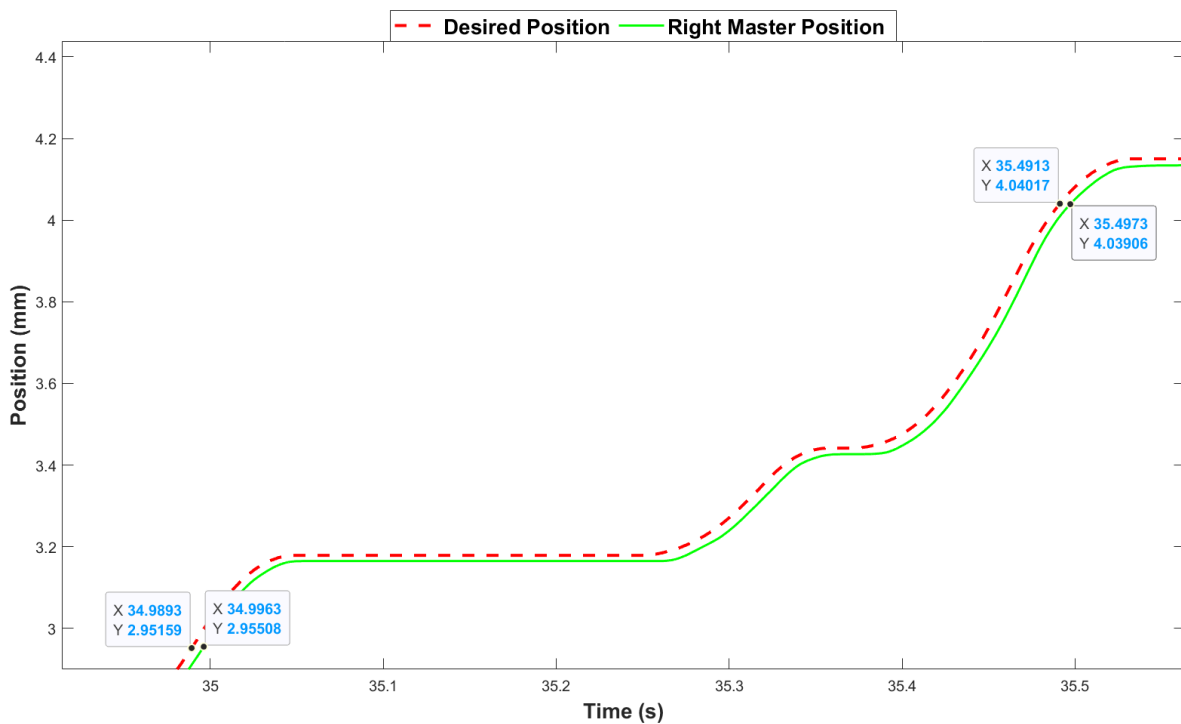
Figure 6-11. Right Master Position Response Close-up.

By gathering data from all the tests, it was determined that the average time elapsed until the actual position of the master robots reached the desired position command was around 6 ms for both motors. This fact can also be seen by the data tips in the close-up graphs shown above, where the elapsed time varied between 5 and 7 ms for the positions to match within less than a margin of ±0.01 mm. The elapsed time between desired and actual position

seemed to be reasonably increased only in cases where significant forces (over 5 N) were exerted on the force sensors or where rapid change of movement direction was performed.

In Figure 6-12, the recorded positions of both the left and right master motors are displayed in a single diagram. This figure illustrates that during the system's operation, the two master robots move linearly by the same amount in opposite directions. To accomplish smooth rotation of the pulley of the experimental setup, the two robots should be in complete coordination with one another.
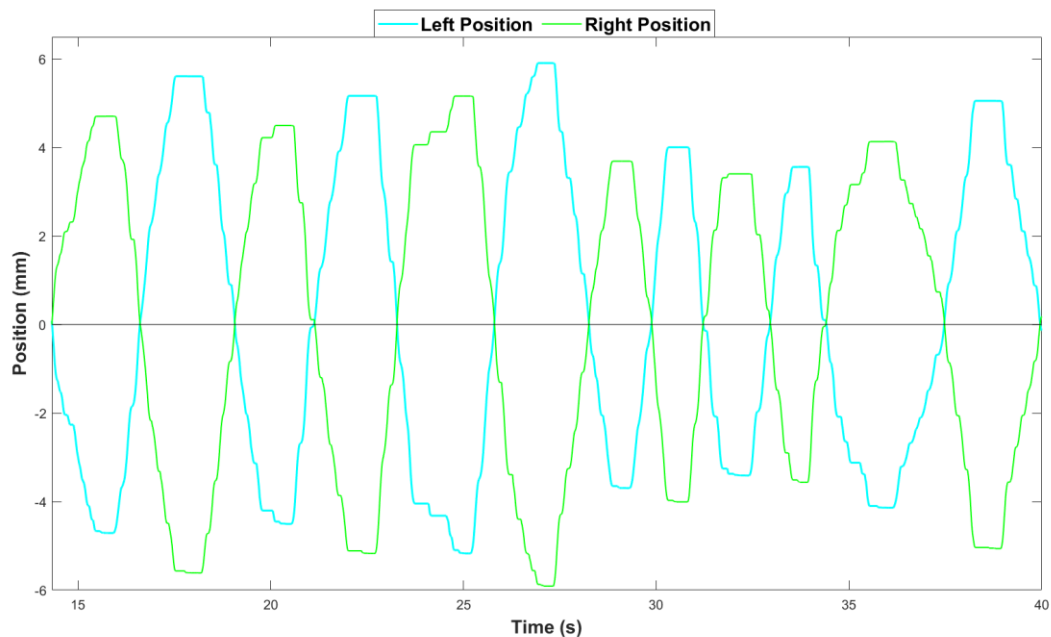
Figure 6-12. Left (cyan) and Right (green) Master Position Responses.

The above position responses were recorded during the conduction of a test where relatively rapid wrist movements were performed. Below, the position responses from a test involving slower movements are displayed.
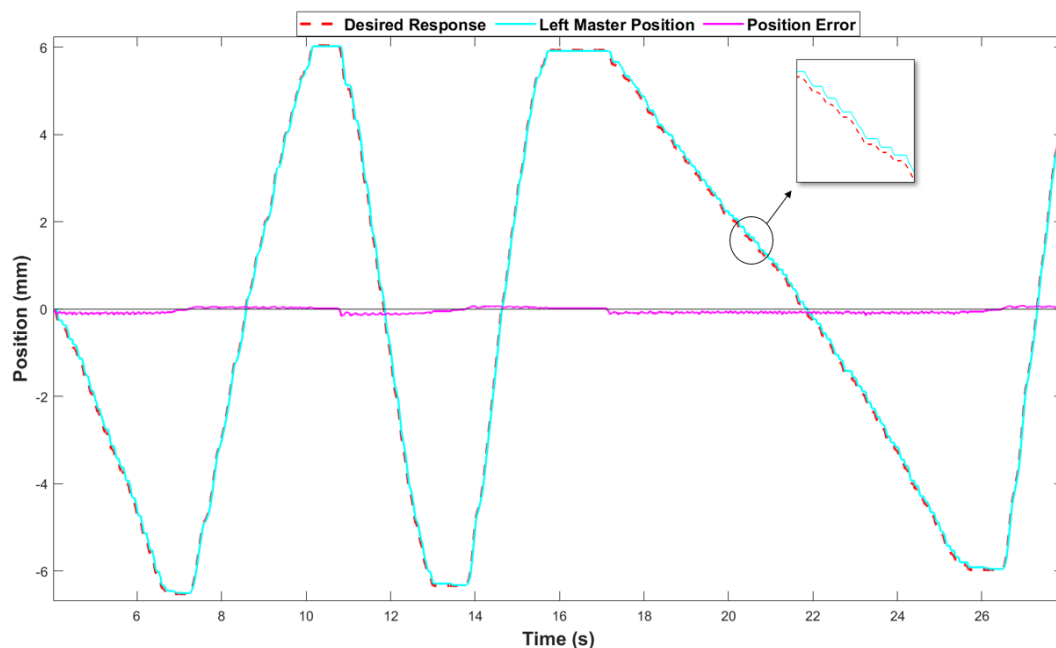
Figure 6-13. Left Master Position Response – Slow Wrist Movement.
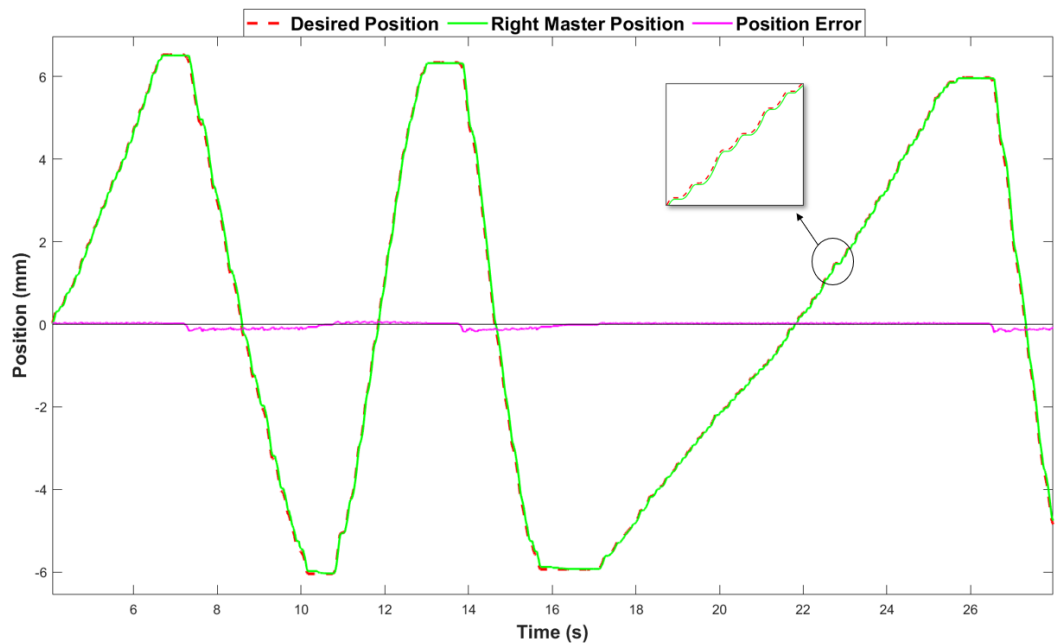
Figure 6-14. Right Master Position Response – Slow Wrist Movement.

It is worth noting that when the user performed very slow rotational movements of the wrist, in particular, slower than approximately 2 rpm, the system's response seemed to get less smooth (bumpier). In general, the system had the smoothest response when the angular velocity of the prosthetic ranged between 3-10 rpm, while for greater velocities, the quality of the response began to deteriorate. To identify the cause of this behaviour, further analysis is required which was not conducted in this thesis due to time limitations. Therefore, to interpret the results appropriately, this matter should be addressed in future work.

To give a complete picture of the system's operation, other parameters recorded during the experiments are presented next.

Figure 6-15 shows the output voltages from the FSRs' circuit (see Chapter 3.2.3), which are converted to force signals inside the slave's control loop.
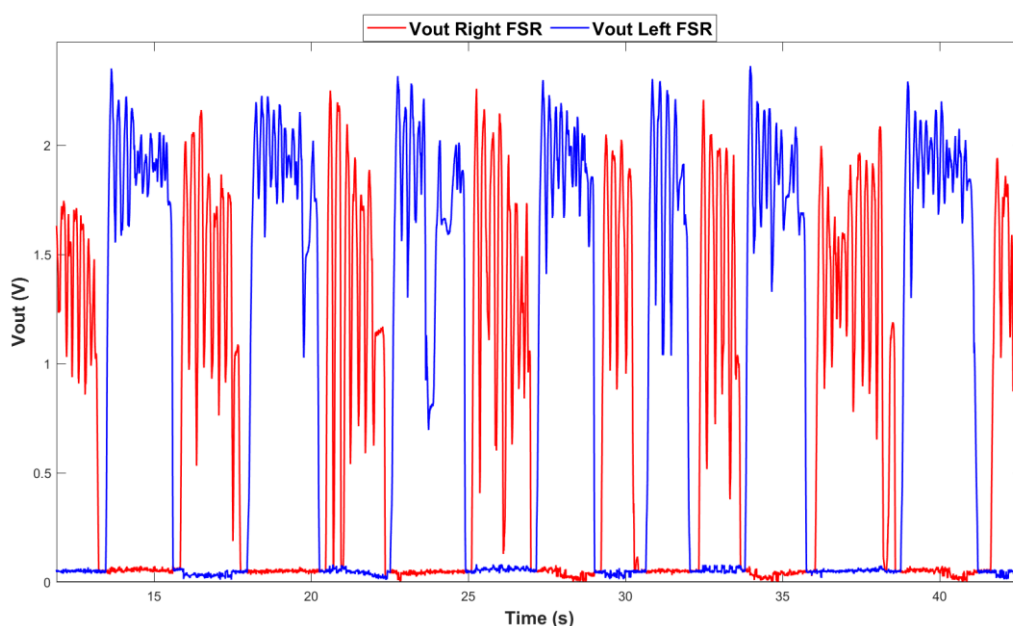
Figure 6-15. Output Voltages from the FSRs' circuit.

When the user attempts a wrist flexion, the left FSR is pressed, which increases the output voltage represented with the blue colour. Correspondingly, an extension of the user's wrist exerts forces to the right FSR (illustrated with red colour). It can be seen that even though the voltage signals fluctuate, they do not intertwine. Therefore, the user's intention regarding the motion he or she wants to perform with the prosthetic can be derived easily from the measured signals. Due to the quality of an FSR sensor, this fact is not self-evident and was only ensured by the correct design of the FSR housings that allow the proper loading of the FSRs without leaving any residual stresses when the pressure to the sensor is released. A close-up of Figure 6-15 is displayed in Figure 6-16 to demonstrate that when the force sensors are not pressed, the output voltage instantly drops to almost zero (the minor offset of approximately 0.05 V does not affect the system since it does not trigger the motion of the slave).
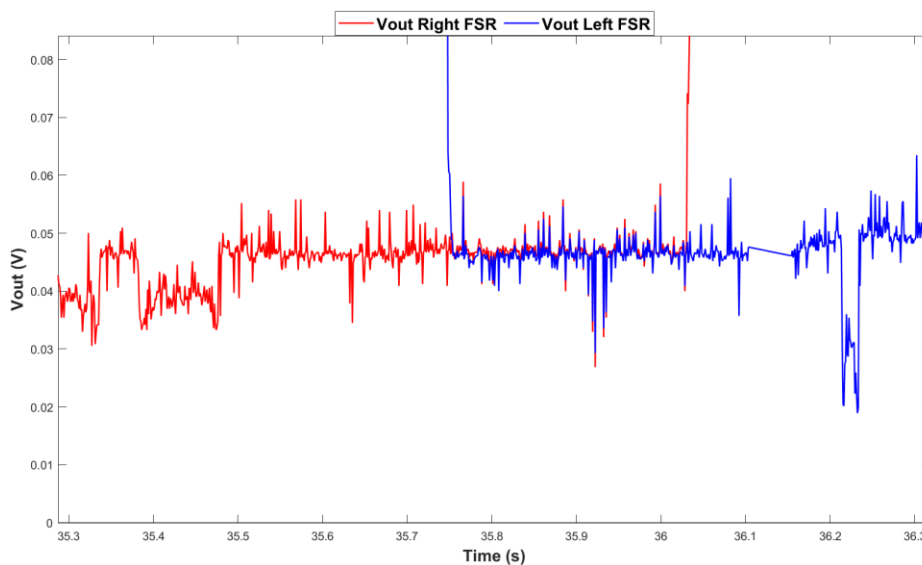
Figure 6-16. Close-up on the FSR output voltages when the sensors are not pressed.

Another interesting graph is given in Figure 6-17, which displays the duty cycle command calculated inside the closed-loop PV controller and directed to the master motor driver to set the voltages of the two motors appropriately.
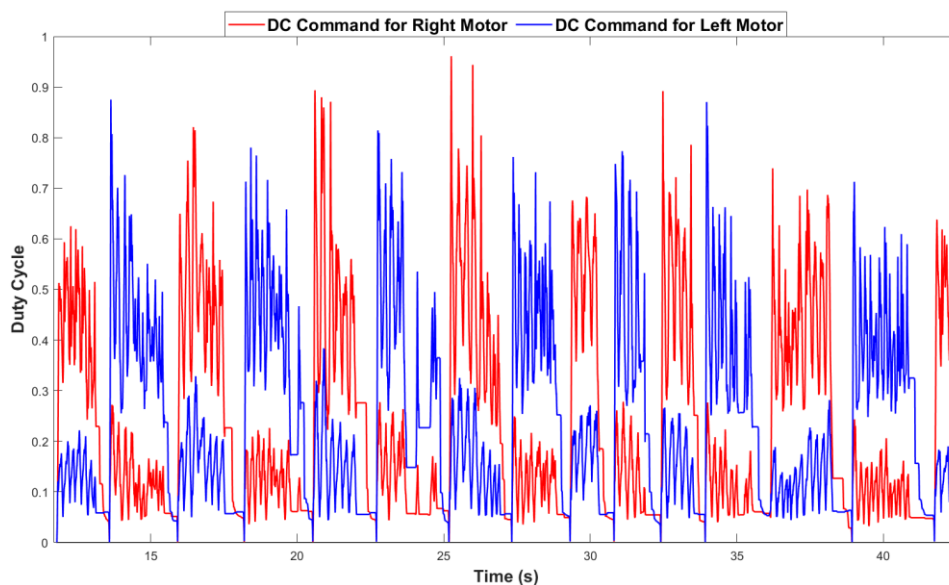
Figure 6-17. Duty Cycle command for the master motor driver.

As indicated by the legend of the figure, the blue and red coloured curves represent the DC commands directed to the driver for the left and right master motors, respectively. To interpret the diagram, the following must be considered.

Whenever the user wants to move the prosthetic limb, both master motors should move in opposite directions. However, in addition to simply linearly displacing the nut and depending on the direction of the motion, one of the two motors also has to overcome an external force that is applied to its FSR by the corresponding muscle. Therefore, at any given moment, the DC command towards one of the two motors has to be greater than the other since the loading scenarios differ. This is why, for example, between the time period of 25-27 s, the DC for the right master motor is greater. At that time, the user attempted to conduct a flexion of the wrist, thus loading the right FSR and as a consequence, the right motor required higher voltage to follow the position of the slave. On the other hand, the vice-versa is valid for the time period of 27-29 s which corresponds to an extension of the user's wrist. All the figures presented in this chapter so far (except Figure 6-13 and Figure 6-14) belong to the same experimental trial so that correlation between the measured parameters (FSR circuit output voltages, force signals, linear positions and duty cycles) can be observed.

In conclusion, from the data gathered during the response experiment, it can be inferred that the system's transparency is achieved. During normal operation, virtually no time delays were observed, while the linear positional errors between slave and master were kept below 0.15 mm for both master robots. At this point, it should be mentioned that the Simulink control loop solver and the sensors' sampling period were set to 1 ms. This was only possible due to the use of the DS1103 controller board. In the real application, where two less powerful microcontrollers will execute the communication and the control loop calculations, the sampling period would inevitably increase. Therefore, this and the following experiments must be repeated and evaluated with the wireless setup.

Nevertheless, regarding the hardware of the project which constitutes the focus of this thesis, based on the results, the adequacy of the selected miniature components was confirmed. The master mechanisms, despite their size and specifications, proved capable of dealing with reasonable muscle forces and movement velocities. The system's response can be characterized as smooth overall; however, there is room for improvement. In the cases of very slow movements or when significant forces were exerted, the master system eventually followed the position of the prosthetic limb, although, with obvious difficulties. Of course, these issues should be confronted either through hardware or software modifications. It should be noted though, that, having always in mind that the final system will depend on two small microcontrollers, no complex software solutions that require considerable processing power should be implemented.

6.3   Power Consumption Test

Following the response experiment, another aspect that examines the suitability of the selected mechanical components for this application is their power consumption. The necessity to determine the power consumed during the operation of the master system boils down to two main reasons.

Firstly, the fact that the master system is intended to be eventually implanted inside an amputated arm entails that it should comply with certain specifications. As mentioned in Section 3.1.2, based on initial findings from [11] regarding thermal losses, the Biomechatronic

EPP topology seemed to be safe and feasible, assuming that each master motor placed inside the amputated limb would have a power consumption equal to 0.5 W.

Secondly, since the concept of the Biomechatronic EPP implies that the implantable device would be wirelessly charged, an appropriate rechargeable battery should be identified. Therefore, this power consumption test could serve as the basis for conducting the wireless charging study in future works.

6.3.1 Procedure

In total, five tests were conducted to obtain an estimation of the motors' power consumption. During the tests, which lasted between 30-60 seconds each, the user made random flexion and extension movements that one might typically perform with their wrist.

The power P_m consumed by each master motor can be derived from the following equation:

$$P_m = V_a i_a \tag{4-29}$$

where V_a is the voltage applied to the motor and i_a the current running through the motor. Hence, the motors' voltage and current are the parameters that need to be measured during the experiments in the lab. However, this is easier said than done since the output of the master motor driver is a PWM signal. Accordingly, the voltage applied to the master motors and by extension the current are in PWM form. Unfortunately, the DS1103 controller board is not capable of measuring PWM voltage, thus, an alternative route was followed.

It was assumed that the voltage V_a applied to each motor could be obtained through the duty cycle command directed to the motor driver. Since a voltage mode control is implemented, in theory, the duty cycle command ranging from 0 to 1 should be directly proportional to the operating voltage of the driver (in this case, 8.3V). For instance, if the duty cycle command from the control loop was calculated equal to 0.5, ideally, the voltage applied to the motor should be 4.15V. This is, of course, a simplified assumption that only partially holds true in the real world, especially for duty cycle values near 0% and 100% and in dynamic cases where the DC command changes rapidly, as in this project. Nevertheless, the aim of this test is simply to get an estimation of the master motors' power consumption.

The current i_a of the motors was also acquired indirectly through Equation (4-30).

$$i_a = \frac{V_a - K_T \dot{\theta}_m}{R_a} \tag{4-30}$$

where the torque constant K_T and the resistance R_a of each motor are known since they were determined in Section 4.1 during the identification of the system's parameters. The only other parameter measured in this test is the angular velocity $\dot{\theta}_m$ of the motors with the help of their respective encoders and the dSPACE controller board.

6.3.2 Results

Figure 6-18 and Figure 6-19 give the power consumption calculated in one of the five tests. More specifically, Figure 6-18 shows the power consumed by the left master motor, while Figure 6-19 illustrates the corresponding consumption of the right motor.
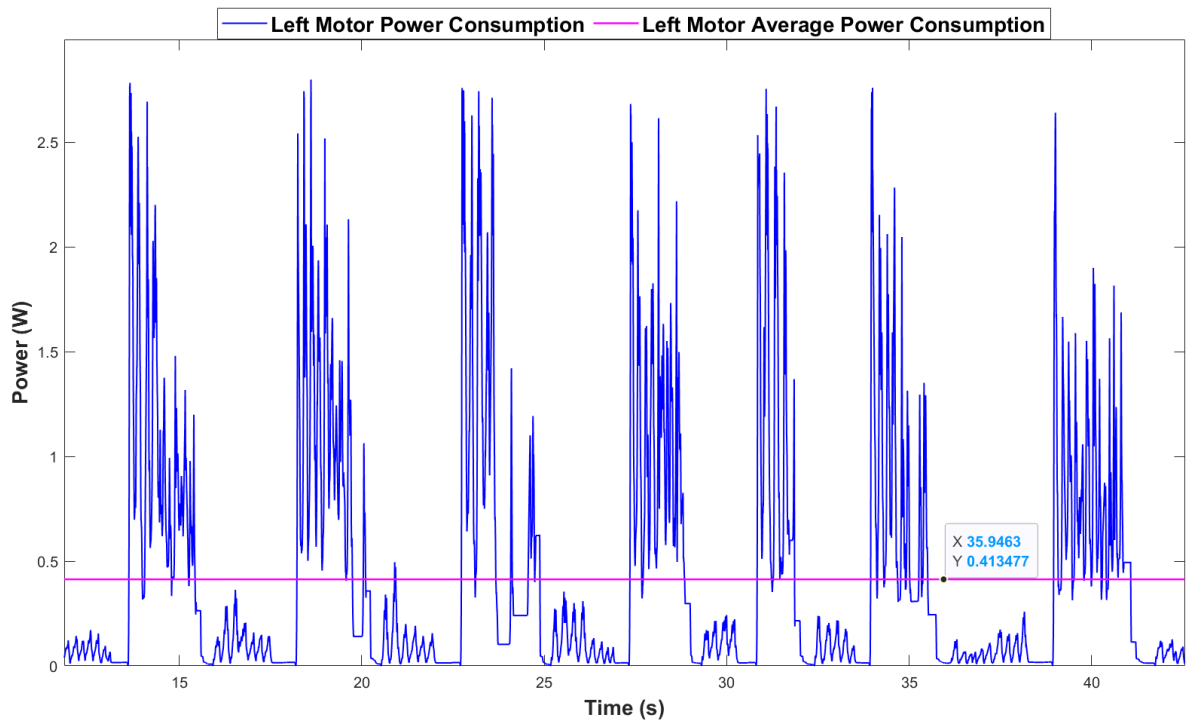
Figure 6-18. Left master motor power consumption test.
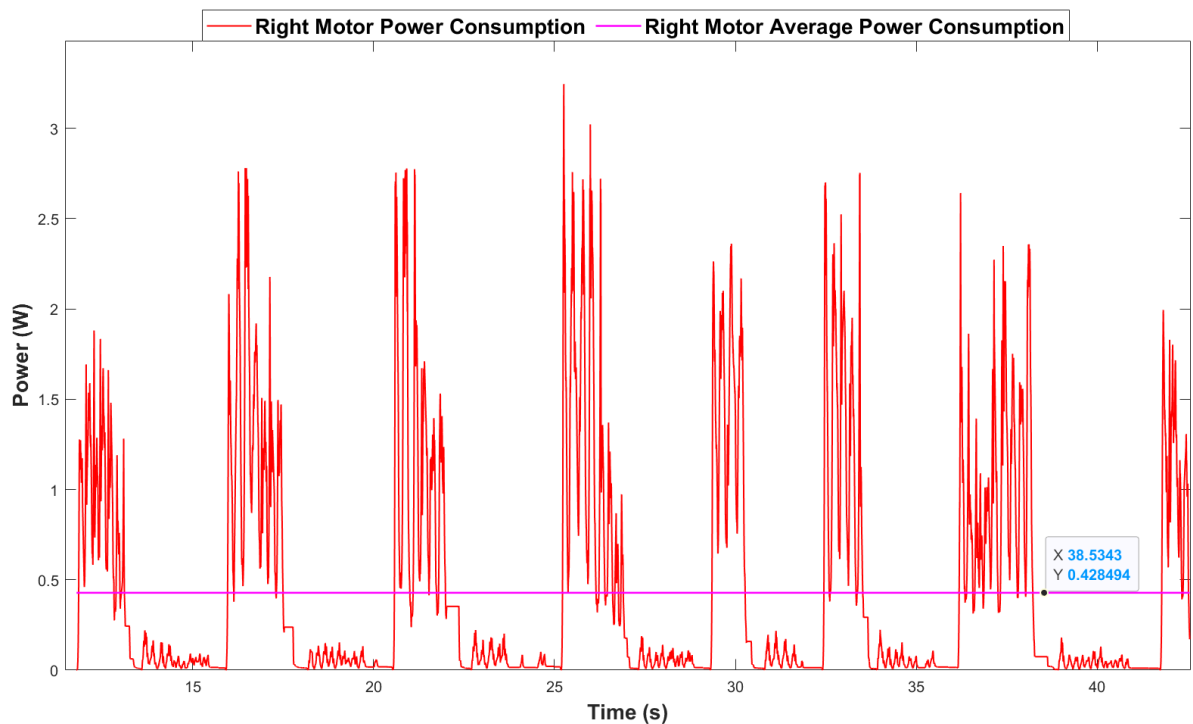
Figure 6-19. Right master motor power consumption test.

Since the forces applied to the master mechanisms change rapidly due to the dynamic nature of the application, there are significant fluctuations regarding the power needs of the motors. Consequently, it was sensible to extract the average power consumption for each motor which is displayed with the distinctive magenta colour.

As seen from the data tips in the figures, in that particular test, the average power consumptions of the left and right master motors were 413mW and 428mW, respectively. The

values obtained from the other four tests were quite similar. This consistency was an encouraging indication concerning the estimation accuracy regardless of the simplified assumptions made to obtain the result. Finally, considering all five tests, the overall average power consumptions were:

$$P_{mAV_{LEFT}} = 421mW \qquad P_{mAV_{RIGHT}} = 437mW$$

Of course, the combined average power consumption of the system was

$$P_{mAV_{TOTAL}} = P_{mAV_{LEFT}} + P_{mAV_{RIGHT}} = 858mW$$

Fortunately, the values estimated above satisfy the power restriction set in [11]. Yet, it must be pointed out that the result of this test greatly depends on the type of executed movement during the tests. In general, as expected, the faster the motions of the wrist or the greater the exerted forces, the greater the system's power consumption. For that reason, the figures displayed above were deliberately chosen to correspond to the figures given in the previous experiment. Therefore, the type of movement that caused the specific power consumptions of Figure 6-18 and Figure 6-19 can be seen in Figure 6-8 and Figure 6-9.

In the future, more precise power measurements should be taken with the final wireless system. In addition to the motors' consumption, these measurements should include the power consumed by the master microcontroller, the master motor driver and any other electronic component that would be part of the implantable device.

6.4　Target Experiment

The aim of the target experiment was to examine the subjects' ability to control the angular position of the slave motor and, essentially, the rotation of the prosthetic limb. In contrast with the response-transparency experiment that involved random movements, in this experiment, the subjects were given specific desired targets according to which they should position the prosthesis.

Before proceeding further, note that due to time limitations, the target and sense experiments were conducted only with two subjects. Therefore, the results of these tests should be considered more as an indication of the system's capabilities rather than undeniable facts. To obtain more reliable results it is essential that the experiments be repeated with more subjects and more trials.

6.4.1　Procedure

Initially, the subjects were given different tables, each containing a set of ten desired targets. The target values in each table were determined randomly and ranged between $\theta_f = -45^\circ$ and $\theta_e = 50^\circ$, which correspond to the prosthesis's movement boundaries for flexion and extension that were set in Section 4.2.2. The subjects were instructed to attempt to reach the desired targets by exerting appropriate forces on the FSRs using the experimental setup presented in Section 6.1 (see Figure 6-4). The attempt would be considered successful only if the subject managed to place the prosthetic limb within ±0.5 degrees from the specified target and remained in that error margin for at least 2 s. The subject would constantly be aware of the prosthetic's exact position by looking at a screen projecting the ControlDesk environment, which is capable of displaying the real-time angular position of the slave as received from the

slave's encoder (see Figure 6-20). A second person acting as a supervisor monitored the experimental procedure to ensure everything was executed as planned.

In total, four such trials were conducted by each subject and the metrics evaluated were the accuracy (error) with which the user could approach the target and the elapsed time between hitting two consecutive targets.
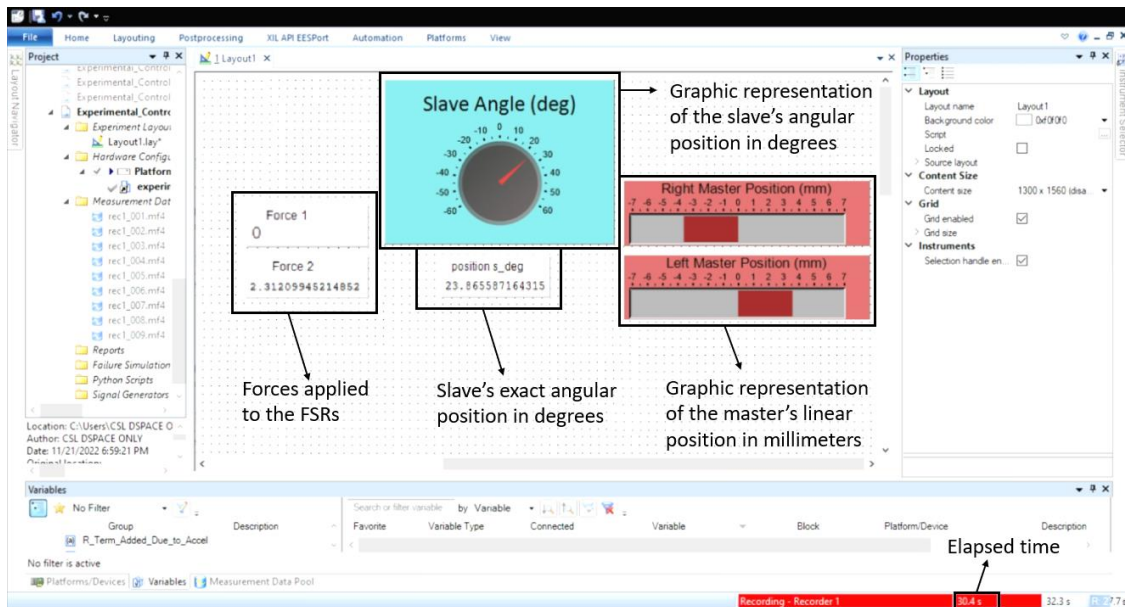
Figure 6-20. ControlDesk Environment displaying measurements in real-time during Target test.

During the tests, videos of the master system, the slave system and the ControlDesk were recorded simultaneously. Figure 6-21 presents a case of wrist flexion (left) and wrist extension (right) by taking individual screenshots from these videos and putting them together.
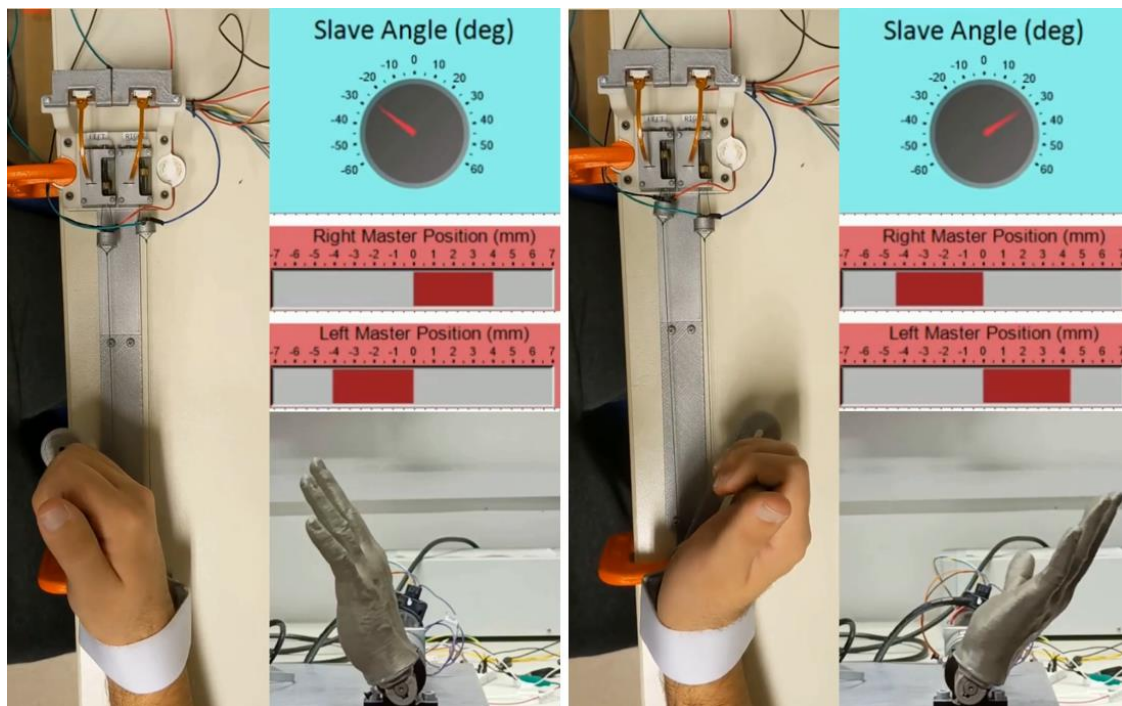
Figure 6-21. Case of wrist flexion (left) and wrist extension (right) performed by the subject.

Each case in Figure 6-21 is illustrated by three individual screenshots. On the left side, a screenshot of the master robots and the subject's upper limb can be seen. On the bottom right, a side view of the prosthesis (slave) is displayed, while in the top right corner, the positions of the master and slave systems are graphically represented by the ControlDesk instruments. During the experiments, it was observed that the prosthesis instantly responded to the user's intention to move and closely followed the angular position of the subject's wrist. This naked-eye observation can also be seen in Figure 6-21 and was later confirmed by comparing the master and slave position responses, as was also shown in the response-transparency experiment.

6.4.2 Results

An example of a target table (Table 6-1) given to one of the subjects is presented below.

Table 6-1. Desired target table given to one of the subjects during the target experiment.

Desired Target Positions	
Target №	**Position [deg]**
1	-21
2	30
3	-34
4	-15
5	-37
6	-13
7	-29
8	16
9	38
10	41

Next, the subject's trial corresponding to the above target table is displayed in Figure 6-22. The blue curve shows the angular position of the prosthetic limb, while the horizontal and vertical black lines represent how the value of the desired target changed as the experiment progressed. The red circles indicate the start and finish of the subject's attempt to reach each of the ten targets. The time periods Δt_i shown with black arrows illustrate the time required by the subject to approach the desired target within an error margin of ±0.5 degrees. On the other hand, the green-coloured time periods portray the time that the subject stayed on the target before moving to the next one.
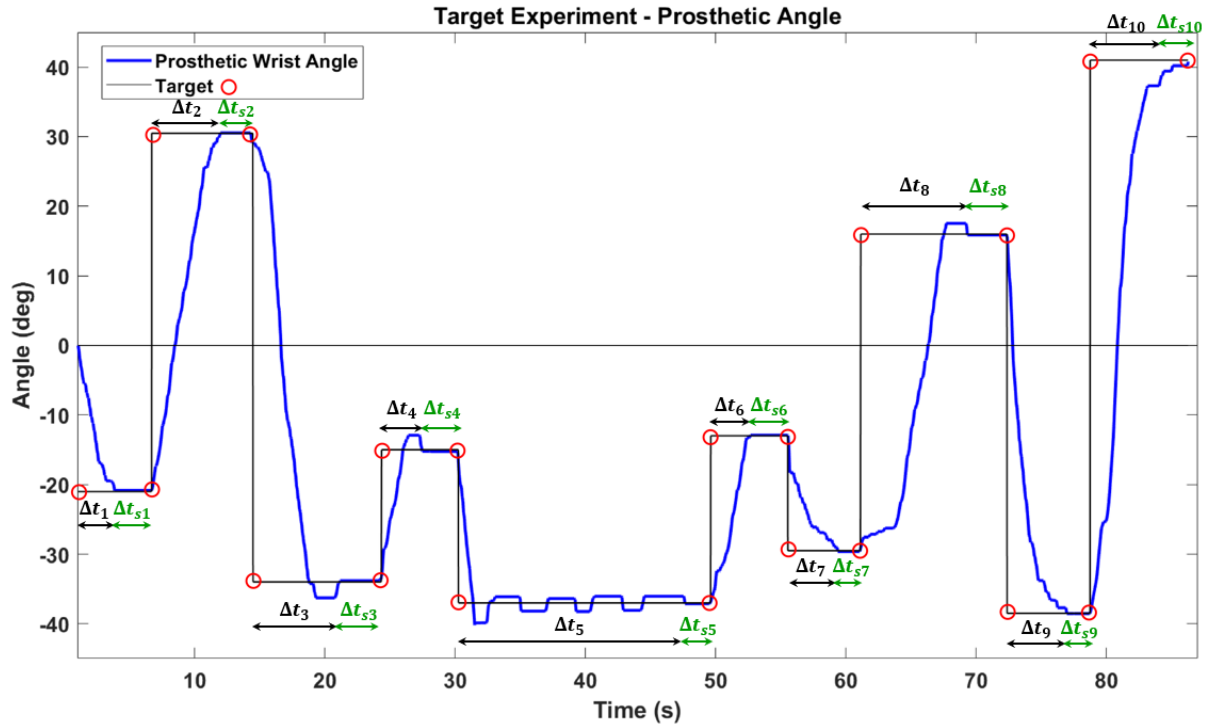
Figure 6-22. Prosthesis angular position [deg] recorded during a target experiment.

In all the trials, the two subjects managed to reach every single target within the ±0.5 degree error margin. This fact is a strong indication that the Biomechatronic EPP control topology enables the user to control the prosthesis with satisfying precision.

The average elapsed time needed by the subjects to reach a desired target was defined as:

$$\Delta t_{mean} = \frac{\sum_{j=1}^{h} \frac{\sum_{i=1}^{n} \Delta t_{j,i}}{n}}{h}$$

(4-31)

where $n=10$ is the number of desired targets in each trial and $h=8$ the number of trials. The metric Δt_{mean} was calculated equal to 5.8s and constitutes a simple average serving as a reference of the time required to precisely position the prosthetic using the specific experimental setup. It should be highlighted that a significant time portion of the time periods Δt_i was often devoted to positioning the prosthetic within the 1-degree error margin and not to the transition from one target value to another. A perfect example of this observation can be seen in Figure 6-22 during the attempt of the subject to reach target number 5. The subject approaches the target in close vicinity within 1-2 seconds; however, it takes another 15-16 seconds to precisely place the slave within the required margin. This implies that if the error margin was slightly wider, for example, ±1 degree, the average elapsed time Δt_{mean} would be expected to improve considerably.

Even though this experiment put the whole Biomechatronic EPP topology to the test, it should be mentioned that the final results heavily depended on the mechanical characteristics of the slave system. The slave system was inherited from previous works and was not meticulously studied in this thesis. It is believed that for this application, the slave motor currently used in the setup is oversized in terms of power and dimensions. Therefore,

especially when the subjects attempted short-quick movements to accurately position the prosthesis, the inertia of the slave assembly combined with the generated torque proved to be a challenging hindrance. This is also one of the reasons why only a tiny portion of the slave's driver output PWM duty cycle range was actually utilized ([0, 0.05] instead of [0, 1]). Duty cycle values over 0.05 were attempted, however, in that case, the acceleration of the motor was clearly surpassing that of an average human wrist.

The last thing that should be discussed concerns the benefit of proprioceptive feedback. As mentioned previously, the position of the subject's wrist was mirrored by the prosthetic with notable accuracy. Therefore, even though the subject was not looking at the prosthesis, he or she was constantly aware of its position since it corresponded to the linear displacement of the subject's actual wrist muscles. This fact alone demonstrates the superiority of a control topology that provides proprioceptive feedback to the user.

6.5   Sense Experiment

The last experiment conducted in this thesis, namely the sense experiment, investigates whether the Biomechatronic EPP control topology can provide the user with information about external forces exerted on the prosthetic limb (slave) during its interaction with objects from the surrounding environment. Essentially, the aim of the experiment is to examine the ability of the user to sense those external forces through the implantable device (master), hence the term 'sense'.

6.5.1   Procedure

In the experiment, only two subjects took part. One of the subjects was extensively familiar with the master-slave system and had been using the experimental setup regularly for about three weeks before the conduction of the experiment. The other subject was significantly less acquainted with the setup and had only tried to operate the system on a handful of occasions. Based on the above, the former subject would be referred to as the experienced subject while the latter as the inexperienced subject. This information would prove crucial regarding the interpretation of the results.

The experiment involved the placement of everyday objects with different stiffness levels in the movement path of the prosthesis. The task for the subjects was to move the prosthetic limb by exerting forces on the FSRs until they hit the object placed in the way of the movement. In each trial, the subjects were left free to move the prosthesis slowly or rapidly, to move it back and forth to repeat the collision with the object, or even to keep applying force to the object for an extended period of time. Afterward, the subjects had to report whether they sensed the existence of an object at all and, if yes, to estimate its stiffness level from a scale of 1 to 5.

The objects employed during the trials are listed below in descending stiffness levels.

Level 1 - Rigid 3D-printed block – (very stiff)
Level 2 - High density foam – (stiff)
Level 3 - Kitchen sponge – (flexible)
Level 4 - Low density foam – (very flexible)
Level 5 - Nothing – (no object)

Examples of objects with stiffness levels 2 and 3 can be seen in Figure 6-23. It should also be noted that in every trial, the selected object was attached with velcro strips on a wooden block which was positioned at a predetermined fixed angle in the range of motion of the prosthesis.
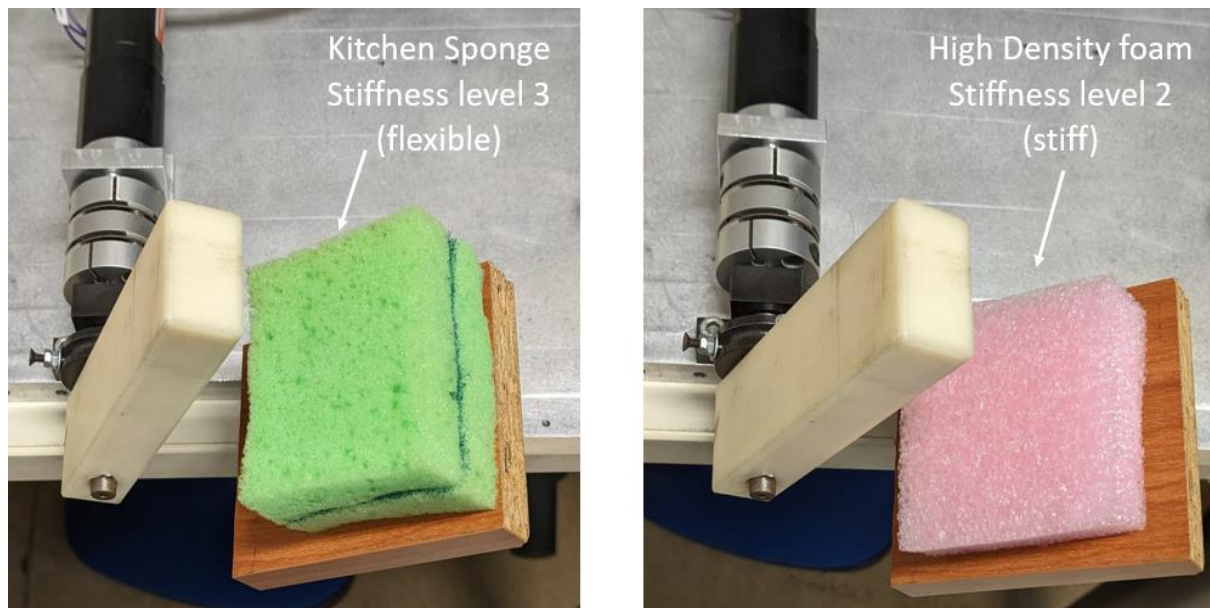
Figure 6-23. Objects placed in the movement path of the prosthesis (slave) – kitchen sponge (left) and high density foam (right).

As seen in the above figure, only for this experiment, the khaki-coloured 3D-printed hand that was seen in previous figures representing the prosthetic limb was replaced by a 3D-printed rectangular prism (see Figure 6-24). This was done to ensure that in each trial, due to its flat shape, the surface area of the prosthesis coming in contact with the object would be the same and to allow the forces to be uniformly spread on larger surface area.
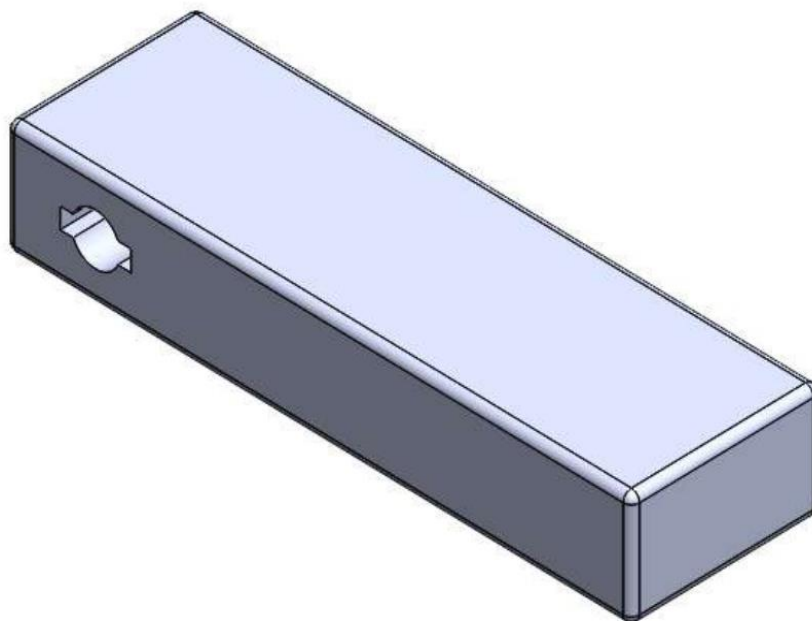
Figure 6-24. 3D-printed rectangular prism used as a prosthetic limb [8].

To have no visual of the prosthesis or the object, during the trials, the subjects were seated staring at a wall. In addition, the subjects had to wear earbuds playing loud music so they could not hear the collision sound generated when the prosthetic hit the object since this might hint at the object's nature.

It must be emphasized that the goal for the subjects was not to identify the object itself but instead to determine how stiff it «feels» compared to the others. The stiffness of an object can be defined as:

$$Stiffness = \frac{Load}{Deformation}$$

Therefore, if the loading configuration is identical, a stiffer object requires a greater load to deform equally compared to a less stiff object. Due to the different stiffness levels, the interaction of the prosthetic with each object felt different. For this reason, before the experiment, both subjects initially performed several mock trials with all the objects to get a sense of how each object behaves.

For example, no deformation could be observed in the case of the rigid 3D-printed block (stiffness level 1 – (very stiff)), no matter the magnitude of the force exerted by the user. In contrast, in the case of the low density foam (stiffness level 4 – (very flexible)), by exerting low magnitude forces, the subjects were able to deform the object significantly.

Just like a spring, a restoring force was exerted from the object to the prosthesis while an object was being compressed. As soon as a subject released the pressure upon the FSRs and, therefore, the object, this restoring force displaced the prosthesis (push back) in order to restore the object to its equilibrium condition. This restoring force varied from object to object and consequently, the prosthesis displacement varied as well. Since the position of the prosthesis is mirrored by the master system, both during the experiment's compression and release stages, the subjects were expected to «sense» the displacement and acceleration of the prosthesis, thus enabling them to distinguish the different stiffness levels.

In other words, since the subjects did not have visual or auditory feedback to identify the objects, they had to rely solely on the proprioceptive feedback that the Biomechatronic EPP control topology can provide to the user through the master system.

In total, fifty trials were conducted by each subject. Each object was placed ten times in random order in the way of the prosthesis and the subject was not informed about the results until after the experiment was completed.

6.5.2 Results

Table 6-2 shows the data collected during the conduction of the sense experiment. The fifty trials for both the experienced and the inexperienced subjects are listed in Table 6-2. As instructed, the subjects gave their estimations based on the scale of 1-5 presented previously, where each integer was represented by an everyday object and corresponded to a certain stiffness level. In the table, the successful estimations of the subjects are signified with green colour while the mistakes are indicated with red.

In total, the experienced subject successfully determined the stiffness level in 46 out of the 50 trials, while the inexperienced subject estimated correctly in 34 out of 50 tests.

Table 6-2.   **Sense experiment data.**

	Experienced Subject		Inexperienced Subject	
Trial №	**Object Placed**	**Subject Estimation**	**Object Placed**	**Subject Estimation**
1	2	2	2	2
2	4	4	3	3
3	5	5	1	1
4	2	2	1	1
5	1	1	1	1
6	1	1	3	4
7	4	3	5	5
8	2	2	3	3
9	1	1	4	4
10	4	4	2	2
11	1	1	4	2
12	3	3	2	1
13	5	5	1	1
14	1	1	5	5
15	2	2	5	5
16	4	4	3	2
17	1	1	2	1
18	4	4	1	1
19	1	1	3	3
20	5	5	1	1
21	5	5	4	4
22	3	3	5	5
23	3	4	4	4
24	2	2	3	3

25	2	2	3	4
26	4	3	5	5
27	5	5	5	5
28	3	3	1	1
29	3	3	2	1
30	2	2	5	5
31	3	3	2	1
32	4	4	3	4
33	1	1	5	5
34	5	5	4	3
35	3	3	3	3
36	2	1	2	1
37	3	3	2	1
38	5	5	1	1
39	4	4	2	2
40	3	3	3	3
41	1	1	4	4
42	5	5	1	1
43	4	4	2	2
44	1	1	4	3
45	2	2	5	5
46	2	2	4	3
47	4	4	5	5
48	5	5	4	3
49	3	3	4	3
50	5	5	1	1

Next, the results are presented more intuitively through bar charts. The bar chart in Figure 6-25 summarizes in percentages the data given in Table 6-2 regarding the ability of the subjects to separate the stiffness levels between all objects. The success rates were 92% and 68% for the experienced and the inexperienced subject, respectively.
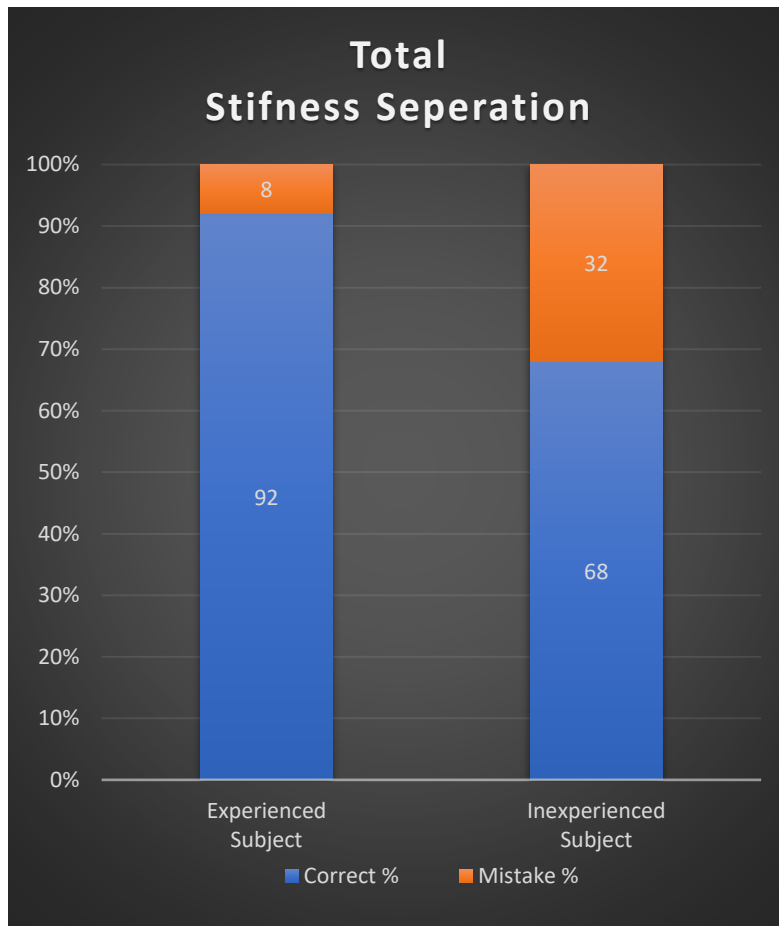
Figure 6-25. Bar chart illustration of the data given in Table 6-2 regarding the overall success rate for each subject.

Two main conclusions can derive from those results:

1) The overall success rates indicate that the Biomechatronic EPP control topology can indeed provide positional and force feedback to the users, informing them regarding the interaction of the prosthesis with the environment.

2) The success rate difference between the experienced and the inexperienced subject amounted to a non-negligible 24%. This fact could suggest the existence of a learning curve concerning the proposed control topology. That is to say that the user might initially have to go through an adjustment period of using the master-slave configuration before fully comprehending and perceiving the system's feedback signals. Simply put, the more accustomed the user is to the system, the better the interpretation of the system's feedback and, therefore, the better the success rate. This adjustment period is expected, especially in the field of prosthetics, where the users have to essentially integrate a foreign limb into the rest of their human body.

Taking a closer look at the unsuccessful attempts, another crucial observation was made. In the overwhelming majority of the mistakes, the subjects failed to answer correctly only by a difference of just one stiffness level. In other words, the mistakes involved objects with similar stiffness levels. For example, a very stiff object was never considered very flexible or vice-versa. The confusion was limited between levels 1 and 2 (category of stiff objects) and between levels 3 and 4 (category of flexible objects). In fact, only two mistakes by the

inexperienced subject involved the misconception that an object in the flexible category was considered a stiff object (trial no.11 and no.16). Figure 6-26 displays the success rate of the experienced and inexperienced subjects regarding their ability to separate the objects belonging to the stiff category (rigid 3D-printed block – (level 1), high density foam – (level 2)) from those characterized as flexible (kitchen sponge – (level 3), low density foam -– (level 4)).
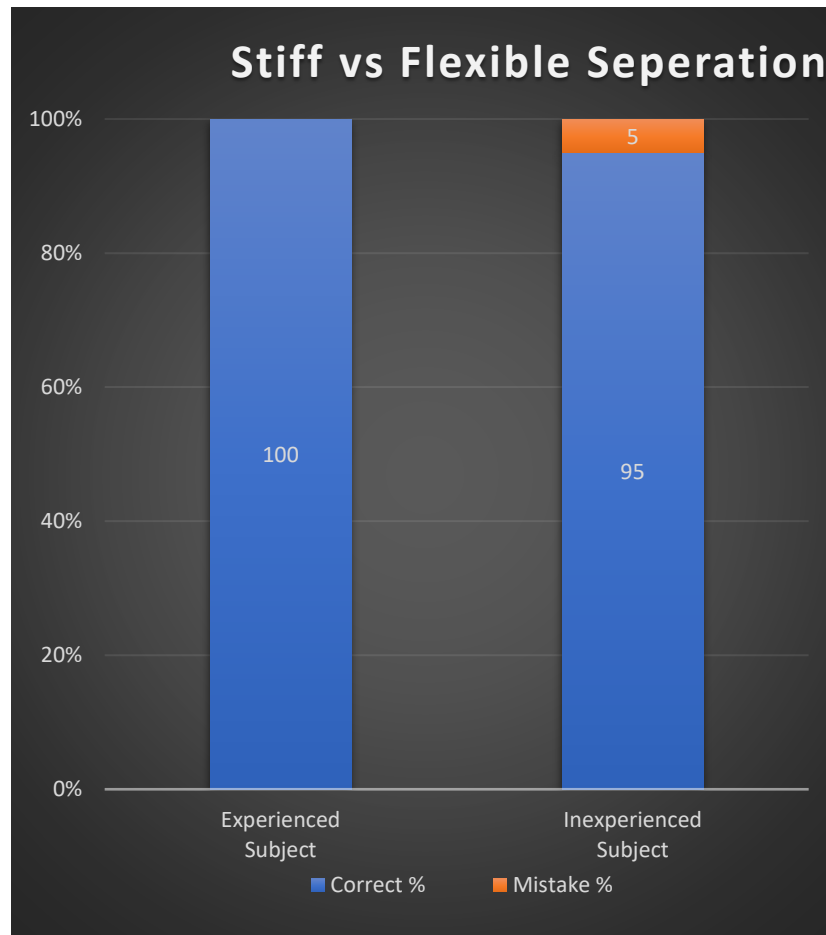
Figure 6-26. Bar chart illustration of the data given in Table 6-2 regarding the subjects' success rate in separating the stiff from the flexible objects.

As seen from the bar chart, the experienced subject distinguished the stiff from the flexible objects with a 100% success rate (40/40), while the inexperienced subject committed only two mistakes resulting in a 95% success rate (38/40). The main conclusions are that:

1) Both subjects could distinguish stiff from flexible objects with remarkable accuracy. However, considering that a few mistakes were made within those two categories (see Figure 6-25), there appears to be a limit to the stiffness identification 'resolution'. Consequently, the Biomechatronic EPP seems to offer the user the ability to distinguish among objects with considerable stiffness difference; however, the success rate declines as the stiffness of the objects is more similar.

2) The subjects' experiences once again seemed to have an impact on their ability to interpret the position and force feedback signals through the master mechanisms.

Lastly, a long-awaited explanation has to be given on how the non-backdrivability feature of the master linear actuator affects the system's functionality regarding the scenario where the prosthetic limb interacts with objects from the environment. As mentioned in Section 2.2.2, non-backdrivability constituted one of the main specifications during the design process of the

master linear mechanisms. In the sense experiment, the non-backdrivability feature played a decisive role in the outcome. The need for this feature derives from the fact that human muscles, in some cases, can exert high-magnitude forces that cannot be easily addressed by a mechanism with such small dimensions as the one used for the master system. More specifically, it was observed that when muscle forces with a magnitude over ~15 N were exerted on the FSRs, the master linear actuators could hardly move due to the increased friction forces. This fact, of course, was considered during the mechanism design stage, and it should be emphasized that it does not affect the system's regular operation where simple wrist movements are performed since those involve way lower-magnitude forces, usually up to 5-6 N (see Figure 6-7). The higher-magnitude muscle forces (>15 N) typically appear in cases where the amputee wants to deliberately exert significant force with the prosthetic limb, for instance, to lift or apply pressure to an object. The latter case of compressing an object was examined in the sense experiment. In particular, when the prosthesis collided with an object, the user had to increase the forces applied to the FSRs to compress it; thus, high-magnitude forces (>15 N) were developed on the FSRs. In this case, if the system was backdrivable, since the linear actuators cannot counteract the developed forces to neutralize them, the residual muscles would be able to drag and linearly displace the lead screw nut at will, regardless of the master position closed-loop control command. Therefore, in such a scenario, the control would be "broken" and the nut position would not correspond to the prosthetic limb's position. This issue could be confronted either by considering the use of a higher-power master mechanism that could counteract even the strongest muscle forces or by selecting a non-backdrivable one. The former solution was rejected during the design stage, as a higher-power mechanism would not qualify regarding the dimensional and power consumption specifications, constituting the system's implementation unfeasible. On the other hand, by selecting a non-backdrivable mechanism, the system self-locks when high-magnitude forces are applied. Consequently, the user is able to feel a reaction force that corresponds to the force that he/she is exerting with the residual muscles. As a result, the prosthetic limb can interact with objects from the environment depending on the force command given by the residual muscles, while the user will be able to sense this force through the master system due to the non-backdrivability feature. Another significant benefit of this feature concerns power consumption and conservation. This can be made clear by the following example. As soon as the prosthetic limb encounters an obstacle from the environment which prevents it from moving, the master mechanisms are also obliged to stop moving. That is because the master system has as input reference the position of the prosthesis, and, therefore, if the prosthesis is fixed (not moving), then the master system should also remain fixed (not moving). However, suppose the system was backdrivable and the user wanted to apply force to the object, for example, to compress it. In that case, the master system should have to devote power constantly to counteract the forces exerted by the muscles to prevent the nut from displacing. In fact, this scenario would also constitute the most power-demanding scenario of the system. Nevertheless, this unnecessary power consumption is completely averted since the system is self-locking and therefore the forces from the residual muscles cannot displace the nut. As a result, the master system can rest and power is conserved, while at the same time, dangerous overheating scenarios are avoided.

7   Conclusions and Future Work

7.1   Conclusions

This chapter summarizes the findings of this work. This thesis focused on developing the smallest possible mechanism prototype regarding dimensions and power consumption that satisfies the requirements set by the proposed Biomechatronic EPP control topology. Standing on the shoulders of previous works, the appropriate specifications were set during the mechanism design stage to achieve the desired level of prostheses control. Subsequently, all the components comprising the new master system were meticulously selected, ordered and assembled in the lab. Then, the parameters of the system were identified, and the Biomechatronic EPP control scheme was designed. The communication between master and slave was achieved through the dSPACE DS1103 PPC controller board and a new experimental setup was constructed in the lab to perform appropriate tests.

The response-transparency experiment showed that the prototype is functional and that the miniature electromechanical components can adequately cope with the expected forces and velocities of the application. Moreover, the transparency of the system was confirmed since, during normal operation, the desired position of the slave was reached in under 10 ms by the master mechanism, while the linear positional errors did not exceed 0.15 mm for both master robots. The overall response of the system was smooth; however, it was observed that for wrist movements with angular velocities less than 2 rpm or more than 10 rpm, the quality of the response began to decline.

From the power consumption tests, it was estimated that when the user performs random flexion or extension movements with the wrist, each master motor consumes, on average, around 400-450 mW. Consequently, the selected components seem to also comply with the desired power consumption goal of 500 mW per motor set in [11].

The target test indicated that the system enables the users to accurately place the prosthetic limb within ±0.5 degrees from a desired angular position.

Lastly, the results of the sense experiment suggested that the mechanical system through the Biomechatronic EPP control topology can provide users with information regarding the prosthesis's interaction with the environment. More specifically, the users successfully recognized the relative stiffness of everyday objects that the prosthetic limb interacted with during the experiments. In addition, the results indicated that new users might require to go through an adjustment learning period of getting familiar with the system before being able to interpret the system's feedback signals to their full extent.

Based on these findings, the proposed topology seems capable of reinstating the proprioception of the user through the master-slave configuration. Information regarding the position and external forces applied to the prosthetic limb was conveyed to the user without the need for visual feedback. More importantly though, the fact that all of the above were accomplished using the miniaturized master mechanism prototype demonstrates that the Biomechatronic EPP can be realistically implemented.

Concluding, even though there is a long way ahead and significant room for improvement, the results in this thesis reinforce the promising future of the Biomechatronic EPP control topology in the field of prosthetics.

7.2 Future Work

Following the construction of the miniaturized master system, the next step should be a complete and definitive transition to wireless communication between the master and the slave. This is practically already implemented in the lab; however, there are a few adjustments to be made so that the wireless setup is running satisfyingly compared to the wired setup. Even though the dSPACE platform proved to be an extremely helpful tool for real-time testing and measuring, a wireless implementation would pave the way toward realizing the concept of the proposed topology.

As soon as this is accomplished, the experiments performed in this thesis should be repeated methodically, employing more subjects and more trials to establish or dismiss the aforementioned findings. As mentioned previously, the conducted experimental tests had the form of a proof of concept, and the results should be interpreted only as indications of the system's capabilities. Therefore, experiments following strict protocols should be carried out in the future and statistical analysis of the data must be performed.

The implementation of wireless communication and the finalization of the selected electromechanical components will also allow the further miniaturization of the system by designing the complete circuitry on a tiny PCB board.

In addition, the slave system that was largely neglected in the current and previous works should be redesigned and its specifications must be set so that the whole system enters a final phase. For instance, even though until now, the examined degree of freedom was the flexion and extension of the wrist, it might be more sensible to transition to a form of grasping mechanism which also constitutes a single degree of freedom but has more utility to the amputee.

Finally, another significant area that has to be examined is the system's power supply. Following the determination of power requirements for both the master and slave systems, appropriate rechargeable batteries should be identified and, more importantly, the wireless charging circuit concerning the implantable master system must be designed.

8 References

[1]   Brigstocke, G., Hearnden, A., Holt, C.A., Whatling, G., "The functional range of movement of the human wrist. " *J Hand Surg Eur.* 2013, 38(5), pp. 554–556.

[2]   Bertos, Y.A., "A microprocessor-based E.P.P. position controller for electric-powered upper-limb prostheses," *Master of Science*, Electrical & Computer Engineering, Northwestern University, Evanston, IL, M A, 1999.

[3]   BBC Bitesize., KS3, Biology, Living Organisms, Skeletal muscles, www.bbc.co.uk/bitesize/topics/znyycdm/articles/zd7yydm, (accessed Jan. 28, 2023).

[4]   Childress, D.S., "Control of Limb Prostheses", Chapter 6D, *Atlas of Limb Prosthetics: Surgical, Prosthetic, and Rehabilitation Principles*, 2nd ed., Bowker, H.K. & Michael, J. W. (eds.), Mosby-Year Book, Inc., St. Louis MO, 1992, pp. 175-199.

[5]   Doubler, J.A. & Childress, D.S. (1984b), "Design and Evaluation of a Prosthesis Control System Based in the Concept of Extended Physiological Proprioception", *Journal of Rehabilitation Research and Development*, 21(1), pp.19-31.

[6]   Controzzi, M., Cipriani, C. and Carrozza M. C. "Miniaturized non-back-drivable mechanism for robotic applications." *Mechanism and Machine Theory* 45, 2010, pp.1395-1406.

[7]   Konstantineas, P., "Ασύρματος Βιομηχανοτρονικός Έλεγχος Προσθετικού Άνω Άκρου," *Master Thesis*, School of Mechanical Engineering, National Technical University of Athens, Athens, 2022.

[8]   Kontogiannopoulos, S., "Μια Βιομηχανοτρονική EPP Τοπολογία Ελέγχου Άνω Προσθετικού Άκρου και η Πειραματική Σύγκριση της Απόδοσης της με Άλλες Τοπολογίες Ελέγχου", *Diploma Thesis*, School of Mechanical Engineering, National Technical University of Athens, Athens, 2018.

[9]   Koukoulas, N., "Ασύρματος Βιομηχανοτρονικός Έλεγχος Προσθετικού Άνω Άκρου," *Master Thesis*, School of Mechanical Engineering, National Technical University of Athens, Athens, 2017.

[10]   Mablekos-Alexiou, A., "Design and Simulation of a Master Slave Architecture Biomechatronic EPP upper-limb prosthesis (Σχεδιασμός και Προσομοίωση Συστήματος Τηλεχειρισμού Προσθετικού Άκρου με Ιδιοδεκτική Αίσθηση)," *Diploma Thesis*, Mechanical Engineering, National Technical University of Athens, Athens, Greece, 2016.

[11]   Moutopoulou, E., Bertos, G.A., Mablekos-Alexiou, A., and Papadopoulos, E.G., "Feasibility of a Biomechatronic EPP Upper Limb Prosthesis Controller," in 2015 *37th Annual International Conference of the IEEE Engineering in Medicine and Biology Society (EMBC)*, 2015, pp. 2454-2457.

[12]   Vahid-Araghi, O., and Golnaraghi, F., "*Friction-Induced Vibration in Lead Screw Drives*", Springer, New York, 2011.

[13]   Orthofixar, Hand & Wrist Movements, https://orthofixar.com/special-test/hand-wrist-movements/, (accessed Jan. 28, 2023).

[14]   Simpson, D.C., "The choice of control system for the multimovement prosthesis: extended physiological proprioception (EPP)," in *The Control of Upper-Extremity Prostheses and Orthoses, e. a. Herberts*, Ed.: Springfield, IL: Thomas, 1974, pp. 146-150.

[15]   Vangelatos, Z., "Design of Upper limb prosthesis: Experimental Comparison of the Classic and Biomechatronic Extended Physiological Proprioception," *Diploma Thesis,* School of Mechanical Engineering, National Technical University of Athens, Athens, 2017.

[16]   Winters, J. M. and Stark, L. (1985a) "Analysis of fundamental movement patterns through the use of in-depth antagonistic muscle models." *IEEE Biomed. Engng.* BME-32, 826-839.

[17] Winters, J. M. and Stark, L. "Estimated mechanical properties of synergistic muscles involved in movements of a variety of human joints." *J.Biomechanics* Vol. 21, No. 12, 1988, pp. 1027-1041.

[18] Winters, J. M. and Stark, L. "Muscle Models: What Is Gained and What is Lost By Varying Model Complexity." *Biol. Cybern.* 55, 1999, 403-420.

[19] Yokokohji, Y. and Yoshikawa, T., "Bilateral control of master-slave manipulators for ideal kinesthetic coupling-formulation and experiment," *IEEE Trans. on Robotics and Automation*, vol. 10, no. 5, 1994, pp. 605-620.

[20] www.ondrivesus.com/wormwheel-gearboxes/miniature#1

[21] www.pololu.com/product/2130

[22] https://ghw-modellbau.de/Spur-gear-Polyacetal-Module-05-18-T

[23] https://www.skf.com/group/products/rolling-bearings/ball-bearings/deep-groove-ball-bearings/productid-W%20638%2F1.5-2Z

[24] https://www.helixlinear.com/blog/lead-screws/lead-screws-vs-ball-screws-which-will-work-best-for-your-application/

9 Appendix A Datasheets

Master Motor

DCX 8 M ∅8 mm, precious metal brushes, DC motor

Key Data: 0.5/1.0 W, 0.65 mNm, 17 300 rpm

M 5:2
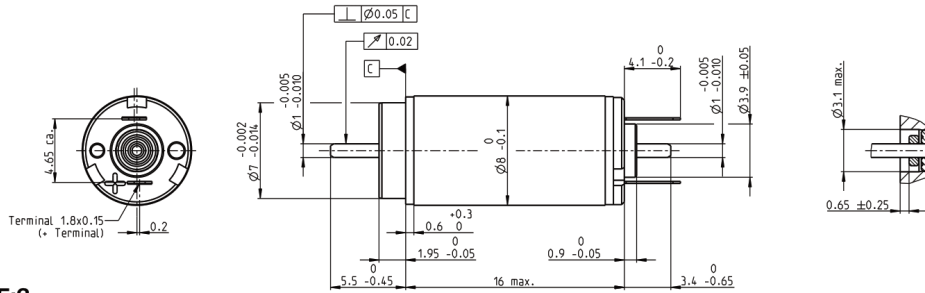
	Motor Data							
1_	Nominal voltage	V	2.4	4.2	6	7.2	9	12
2_	No load speed	rpm	11500	11700	11000	11900	11900	12900
3_	No load current	mA	11.9	6.93	4.51	4.12	3.3	2.74
4_	Nominal speed	rpm	4780	4950	4190	4820	5190	5800
5_	Nominal torque	mNm	0.653	0.649	0.641	0.62	0.652	0.614
6_	Nominal current (max. continuous current)	A	0.345	0.199	0.13	0.113	0.0949	0.0728
7_	Stall torque	mNm	1.13	1.14	1.05	1.06	1.17	1.13
8_	Stall current	A	0.581	0.34	0.207	0.187	0.166	0.13
9_	Max. efficiency	%	74	74	73	73	74	74
10_	Terminal resistance	Ω	4.13	12	29	38.5	54.3	92.2
11_	Terminal inductance	mH	0.014	0.0411	0.0941	0.117	0.183	0.276
12_	Torque constant	mNm/A	1.95	3.360	5.08	5.67	7.07	8.71
13_	Speed constant	rpm/V	4900	2850	1880	1680	1350	1100
14_	Speed/torque gradient	rpm/mNm	10400	10500	10700	11400	10400	11600
15_	Mechanical time constant	ms	4.17	4.15	4.18	4.24	4.15	4.28
16_	Rotor inertia	gcm^2	0.038	0.0379	0.0372	0.035	0.038	0.035

	Thermal data		
17_	Thermal resistance housing-ambient	K/W	101
18_	Thermal resistance winding-housing	K/W	16.9
19_	Thermal time constant winding	s	2.31
20_	Thermal time constant motor	s	162
21_	Ambient temperature ball bearings	°C	-30...+85
	Ambient temperature sleeve bearings	°C	-30...+85
22_	Max. winding temperature	°C	100

	Mechanical data ball bearings		
23_	Max. speed	rpm	17300
24_	Axial play	mm	0...0.1
	Preload	N	0.5
25_	Radial play	mm	0.012
26_	Max. axial load (dynamic)	N	0.1
27_	Max. force for press fits (static)	N	8.8
	(static, shaft supported)	N	100
28_	Max. radial load [mm from flange]	N	0.6 [5]
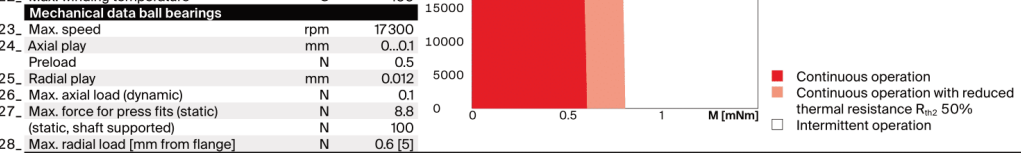
	Mechanical data sleeve bearings		
23_	Max. speed	rpm	17300
24_	Axial play	mm	0.02...0.1
	Preload	N	0
25_	Radial play	mm	0.012
26_	Max. axial load (dynamic)	N	0.1
27_	Max. force for press fits (static)	N	10
	(static, shaft supported)	N	100
28_	Max. radial load [mm from flange]	N	0.4 [5]

	Other specifications		
29_	Number of pole pairs		1
30_	Number of commutator segments		5
31_	Weight of motor	g	4.4
32_	Typical noise level	dBA	–

Operating Range

n [rpm]   Winding 6 V

■ Continuous operation
■ Continuous operation with reduced thermal resistance R$_{th2}$ 50%
□ Intermittent operation

Modular System Details on catalog page 36

Gear	Stages [opt.]	Sensor	Motor Control
358_GPX 8 A	1–5	470_ENX 8 MAG	532_ESCON Module 24/2
			532_ESCON 36/2 DC
			542_EPOS4 Module 24/1.5
			544_EPOS4 Compact 24/1.5

Configuration
Bearing: Sleeve bearings/ball bearings preloaded
Commutation: Precious metal brushes with or without CLL
Flange front/back: Standard flange
Shaft front/back: Length
Electric connection: Terminals or cables (encoder always with Flex)

xdrives.maxongroup.com

April 2022 edition / provisional data / subject to change

Master Motor Encoder

ENX 8 MAG Encoder ⌀8 mm, 1...256 CPT

ENX

Key Data		ENX 8 MAG Incremental	ENX 8 MAG Incremental, Commutation Signal
Number of channels		3	3
Max. counts per turn		256	256
Additional length at motor	mm	7.0	1.0
Ambient temperature	°C	-40...100	-40...100
Weight	g	1	1

Selection criteria	ENX 8 MAG Incremental	ENX 8 MAG Incremental, Commutation Signal
Speed and rotation direction detection	■	■
Speed and position control	■	■
Compact and robust design	■	■
High resolution	▲	▲
Cost effective	■	■

■ suitable   ▲ suitable to a limited extent   ● not suitable

Specifications		ENX 8 MAG Incremental	ENX 8 MAG Incremental, Commutation Signal
Supply voltage Vcc	V	3.0...3.6	3.0...3.6
Typical current draw	mA	13	13
Max. operating frequency	kHz	500	500
Max. Speed	rpm	100 000	100 000
Connection[3]		FPC, 12 pole, pitch 0.5 mm	FPC, 12 pole, pitch 0.5 mm
		Pin 1 Motor+	Pin 1 W1
		Pin 2 Motor-	Pin 2 W2
		Pin 3 Not connected	Pin 3 W3
		Pin 4 GND	Pin 4 GND
		Pin 5 V_{cc}	Pin 5 V_{cc}
		Pin 6 Channel A	Pin 6 Channel A
		Pin 7 Channel B	Pin 7 Channel B
		Pin 8 Channel I	Pin 8 Channel I
		Pin 9-12 Do not connect[1]	Pin 9 H1
		Output signal: CMOS compatible	Pin 10 H2
		Output current per channel: ±4 mA	Pin 11 H3
			Pin 12 Do not connect[1]
			Output signal: CMOS compatible
			Output current per channel: ±4 mA

Configuration	ENX 8 MAG Incremental	ENX 8 MAG Incremental, Commutation Signal
Counts per turn[2]	1...256	1...256

maxon Modular System	Page	Dimensions Standard Version	Notes
maxon DC motor			
DCX 8 M	86		
maxon EC motor			
ECX SPEED 8 M	185–186		

Notes

[1] Applying voltage to these pins may destroy the encoder.

[2] maxon controllers require a resolution of at least 16 pulses.

[3] H1, index and angle zero are aligned with angle commutation zero (see p. 56).

Compatible connector:
Molex 52745–1297, TE 1-1734839-2
Adapter 498157 required for all maxon controllers

Please note: max. continuous current 0.5 A

xdrives.maxongroup.com

Molex FPC Connector

molex
one company) a world of innovation

PLEASE CHECK WWW.MOLEX.COM FOR LATEST PART INFORMATION

Part Number:	**0527451297**
Status:	**Active**
Overview:	FFC-FPC (SMT)
Description:	0.50mm Pitch Easy-On FFC/FPC Connector, Right-Angle, Surface Mount, ZIF, Top Contact Style, 12 Circuits, Gold (Au) Contact Plating, High Barrier Packaging

Series image - Reference only

Documents:
3D Model
Drawing (PDF)
Product Specification PS-52745-051-001 (PDF)
Application Specification AS-52745-001-001 (PDF)
Packaging Specification SPK-52745-002-001 (PDF)
RoHS Certificate of Compliance (PDF)
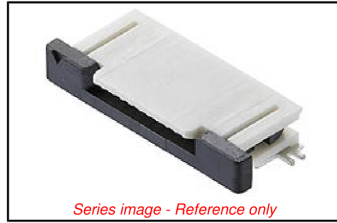
Agency Certification
UL   E29179

General
Product Family   FFC/FPC Connectors
Series   52745
Overview   FFC-FPC (SMT)
Product Name   Easy-On
UPC   822348250509

Physical
Actuator Type   Slider
Circuits (Loaded)   12
Color - Resin   Black, White
Contact Position   Top
Durability (mating cycles max)   20
Flammability   94V-0
Mated Height   2.00mm
Material - Metal   Phosphor Bronze
Material - Plating Mating   Gold
Material - Plating Termination   Gold
Net Weight   174.598/mg
Number of Rows   1
Orientation   Right Angle
PCB Locator   No
PCB Mounting   Surface Mount
PCB Retention   Yes
Packaging Type   Embossed Tape on Reel
Pitch - Mating Interface   0.50mm
Polarized to PCB   Yes
Stackable   No
Temperature Range - Operating   -40° to +85°C
Wire/Cable Type   FFC/FPC

Electrical
Current - Maximum per Contact   0.5A
Voltage - Maximum   50V

Material Info

Reference - Drawing Numbers
Application Specification   AS-52745-001-001
Packaging Specification   SPK-52745-002-001
Product Specification   PS-52745-051-001
Sales Drawing   SD-52745-050-001, SD-52745-051

EU ELV
Not Relevant

EU RoHS   **China RoHS**
Compliant
REACH SVHC
Not Contained Per -
ED/61/2018 (27 June 2018)
Halogen-Free Status
Not Low-Halogen

Need more information on product environmental compliance?

Email productcompliance@molex.com
Please visit the Contact Us section for any non-product compliance questions.

China ROHS   Green Image
ELV   Not Relevant
Prop65   Compliant
RoHS Phthalates   Not Contained

Search Parts in this Series
52745 Series

Master Motor Driver

TEXAS INSTRUMENTS

DRV8833

DRV8833 Dual H-Bridge Motor Driver

1 Features

- Dual-H-Bridge Current-Control Motor Driver
  - Can Drive Two DC Motors or One Stepper Motor
  - Low MOSFET ON-Resistance: HS + LS 360 mΩ
- Output Current (at V_M = 5 V, 25°C)
  - 1.5-A RMS, 2-A Peak per H-Bridge in PWP and RTY Package Options
  - 500-mA RMS, 2-A Peak per H-Bridge in PW Package Option
- Outputs can be in Parallel for
  - 3-A RMS, 4-A Peak (PWP and RTY)
  - 1-A RMS, 4-A Peak (PW)
- Wide Power Supply Voltage Range: 2.7 to 10.8 V
- PWM Winding Current Regulation and Current Limiting
- Thermally Enhanced Surface-Mount Packages

2 Applications

- Battery-Powered Toys
- POS Printers
- Video Security Cameras
- Office Automation Machines
- Gaming Machines
- Robotics

3 Description

The DRV8833 device provides a dual bridge motor driver solution for toys, printers, and other mechatronic applications.

The device has two H-bridge drivers, and can drive two DC brush motors, a bipolar stepper motor, solenoids, or other inductive loads.

The output driver block of each H-bridge consists of N-channel power MOSFETs configured as an H-bridge to drive the motor windings. Each H-bridge includes circuitry to regulate or limit the winding current.

Internal shutdown functions with a fault output pin are provided for overcurrent protection, short-circuit protection, undervoltage lockout, and overtemperature. A low-power sleep mode is also provided.

The DRV8833 is packaged in a 16-pin WQFN package with PowerPAD™ (Eco-friendly: RoHS & no Sb/Br).

Device Information[1]

PART NUMBER	PACKAGE	BODY SIZE (NOM)
DRV8833	TSSOP (16)	5.00 mm × 4.40 mm
	HTSSOP (16)	5.00 mm × 4.40 mm
	WQFN (16)	4.00 mm × 4.00 mm

(1) For all available packages, see the orderable addendum at the end of the data sheet.

Simplified Schematic
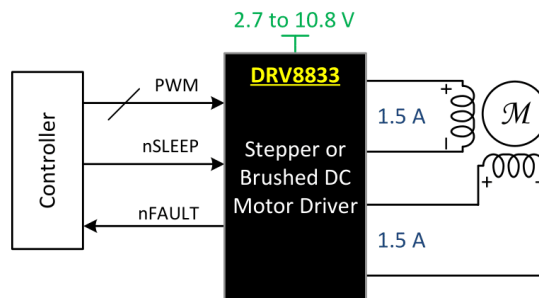
Force Sensitive Resistor

INTERLINK ELECTRONICS®

FSR® 400 Series Data Sheet

Force Sensing Resistors®

Device Characteristics

Actuation Force*	~0.2N min
Force Sensitivity Range*	~0.2N – 20N
Force Resolution	Continuous (analog)
Force Repeatability Single Part	+/- 2%
Force Repeatability Part to Part	+/- 6% (Single Batch)
Non-Actuated Resistance	>10 Mohms
Hysteresis	+10% Average (RF+ - RF-)/RF+
Device Rise Time	< 3 Microseconds

Long Term Drift
    1kg load, 35 days   < 5% log10(time)

Operating Temperature Performance
    Cold: -40ºC after 1 hour   -5% average resistance change
    Hot: +85ºC after 1 hour   -15% average resistance change
    Hot Humid: +85ºC 95RH after 1 hour   +10% average resistance change

Storage Temperature Performance
    Cold: -25ºC after 120 hours   -10% average resistance change
    Hot: +85ºC after 120 hours   -%5 average resistance change
    Hot Humid: +85ºC 95RH after 240 hours   +30% average resistance change

Tap Durability
    Tested to 10 Million actuations, 1kg, 4Hz   -10% average resistance change

Standing Load Durability
    2.5kg for 24 hours   -5% average resistance change

EMI	Generates no EMI
ESD	Not ESD Sensitive
UL	All materials UL grade 94 V-1 or better
RoHS	Compliant

Specifications are derived from measurements taken at 1000 grams, and are given as (one standard deviation/mean), unless otherwise noted.
*Typical value. Force dependent on actuation interface, mechanics, and measurement electronics.

INTERLINK
ELECTRONICS®

FSR® Model 400 Short Tail

Force Sensing Resistor®

Model 400 Short Tail:

Active Area: Ø5.62mm
Nominal Thickness: 0.30mm
Switch Travel: 0.05mm

Sensor Mechanical Data

Ø5.6
(ACTIVE AREA)
R3.8
15.8±0.15
6.35
T=0.30±0.03
0.10

Available Part Numbers:

PN: 34-47021 Model 400 Short Tail
 - No contacts or solder tabs
PN: 34-00005 Model 400 Short Tail
 - with female contacts
PN: 34-00006 Model 400 Short Tail
 - with female contacts and housing
PN: 34-00004 Model 400 Short Tail

 - with solder tabs

ADHESIVE
TOP SUBSTRATE
SPACER ADHESIVE
BOTTOM SUBSTRATE
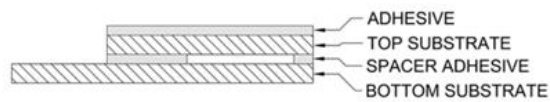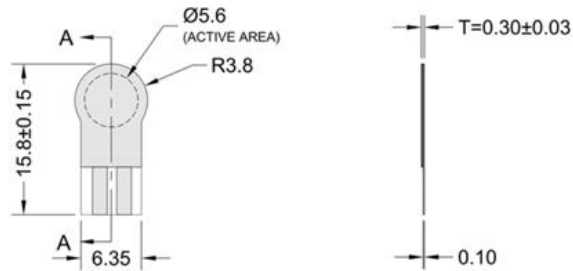
SECTION A-A
LAYER STACK-UP

Exploded View

Slave Motor

RE 30 ⌀30 mm, Graphite Brushes, 60 Watt

maxon DC motor
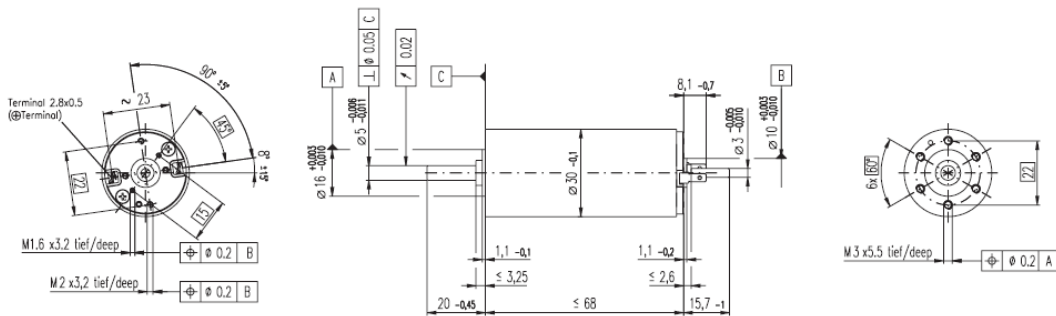
M 1:2

■ Stock program
□ Standard program
▨ Special program (on request)

		Order Number					
according to dimensional drawing		**310005**	310006	**310007**	310008	**310009**	
shaft length 15.7 shortened to 8.7 mm		268193	268213	268214	268215	268216	

Motor Data

	Values at nominal voltage						
1	Nominal voltage	V	12.0	18.0	24.0	36.0	48.0
2	No load speed	rpm	8170	8590	8810	8590	8490
3	No load current	mA	300	212	164	106	78.5
4	Nominal speed	rpm	7630	7900	8050	7810	7750
5	Nominal torque (max. continuous torque)	mNm	51.7	75.5	85.0	83.4	88.2
6	Nominal current (max. continuous current)	A	4.00	4.00	3.44	2.20	1.72
7	Stall torque	mNm	844	991	1020	936	1020
8	Starting current	A	60.5	49.8	39.3	23.5	19.0
9	Max. efficiency	%	86	87	87	87	88
	Characteristics						
10	Terminal resistance	Ω	0.198	0.362	0.611	1.53	2.52
11	Terminal inductance	mH	0.0345	0.0703	0.119	0.281	0.513
12	Torque constant	mNm / A	13.9	19.9	25.9	39.8	53.8
13	Speed constant	rpm / V	685	479	369	240	178
14	Speed / torque gradient	rpm / mNm	9.74	8.71	8.69	9.22	8.33
15	Mechanical time constant	ms	3.42	3.25	3.03	3.17	3.01
16	Rotor inertia	gcm²	33.5	35.7	33.3	32.9	34.5

Specifications

Thermal data
17 Thermal resistance housing-ambient 6.0 K / W
18 Thermal resistance winding-housing 1.7 K / W
19 Thermal time constant winding 16.2 s
20 Thermal time constant motor 714 s
21 Ambient temperature -30 ... +100°C
22 Max. permissible winding temperature +125°C

Mechanical data (ball bearings)
23 Max. permissible speed 12000 rpm
24 Axial play 0.05 - 0.15 mm
25 Radial play 0.025 mm
26 Max. axial load (dynamic) 5.6 N
27 Max. force for press fits (static) 110 N
(static, shaft supported) 1200 N
28 Max. radial loading, 5 mm from flange 28 N

Other specifications
29 Number of pole pairs 1
30 Number of commutator segments 13
31 Weight of motor 238 g

Values listed in the table are nominal.
Explanation of the figures on page 49.

⚠ Tolerances may vary from the standard
specification.

Option
Preloaded ball bearings

Operating Range

n [rpm]

60 W

310007
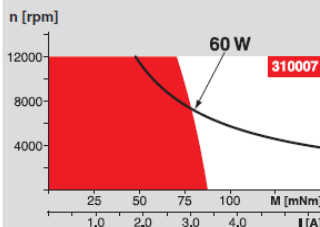
Comments

■ **Continuous operation**
In observation of above listed thermal resistance
(lines 17 and 18) the maximum permissible winding
temperature will be reached during continuous
operation at 25°C ambient.
= Thermal limit.

□ **Short term operation**
The motor may be briefly overloaded (recurring).

— **Assigned power rating**

maxon Modular System   Overview on page 16 - 21

Planetary Gearhead
⌀32 mm
0.75 - 4.5 Nm
Page 239
Planetary Gearhead
⌀32 mm
1.0 - 6.0 Nm
Page 240

Encoder MR
256 - 1024 CPT
3 channels
Page 259

Recommended Electronics:
ADS 50/5   Page 276
ADS_E 50/5   277
EPOS 24/5   294
EPOS2 50/5   295
EPOS P 24/5   297
Notes   18

May 2008 edition / subject to change

maxon DC motor 81

112/117
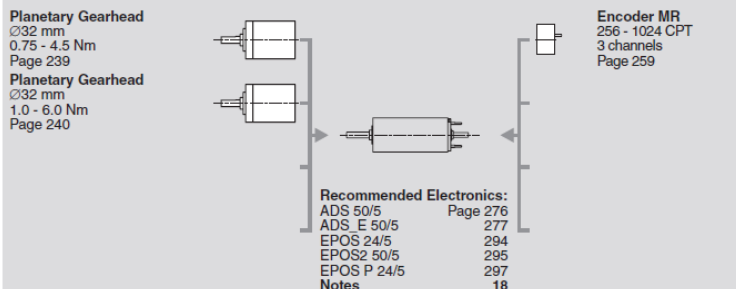
Slave Encoder

Encoder HEDS 5540, 500 Counts per turn, 3 Channels

	Cycle C = 360°e
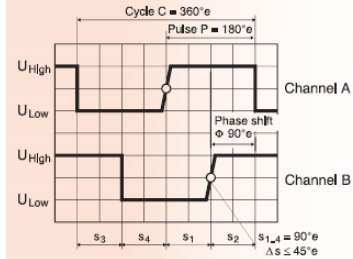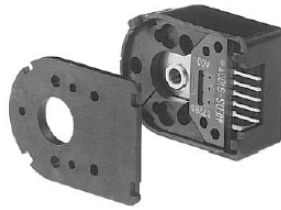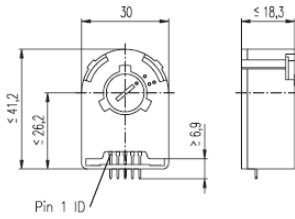
- Stock program
- Standard program
- Special program (on request)

Order Number

	110511	110513	110515		
Type					
Counts per turn	500	500	500		
Number of channels	3	3	3		
Max. operating frequency (kHz)	100	100	100		
Shaft diameter (mm)	3	4	6		

Combination

+ Motor	Page	+ Gearhead	Page	+ Brake	Page	Overall length [mm] / ● see: + Gearhead
RE 25, 10 W	77					75.3
RE 25, 10 W	77	GP 26, 0.5 - 2.0 Nm	235			●
RE 25, 10 W	77	GP 32, 0.4 - 2.0 Nm	237			●
RE 25, 10 W	77	GP 32, 0.75 - 6.0 Nm	238/240			●
RE 25, 20 W	79					75.3
RE 25, 20 W	79	GP 26, 0.5 - 2.0 Nm	235			●
RE 25, 20 W	79	GP 32, 0.4 - 2.0 Nm	237			●
RE 25, 20 W	79	GP 32, 0.75 - 6.0 Nm	238/240			●
RE 25, 20 W	79			AB 28	308	105.7
RE 25, 20 W	79	GP 26, 0.5 - 2.0 Nm	235	AB 28	308	●
RE 25, 20 W	79	GP 32, 0.4 - 2.0 Nm	237	AB 28	308	●
RE 25, 20 W	79	GP 32, 0.75 - 6.0 Nm	238/240	AB 28	308	●
RE 26, 18 W	80					77.2
RE 26, 18 W	80	GP 26, 0.5 - 2.0 Nm	235			●
RE 26, 18 W	80	GP 32, 0.4 - 2.0 Nm	237			●
RE 26, 18 W	80	GP 32, 0.75 - 6.0 Nm	238/240			●
RE 35, 90 W	82					91.9
RE 35, 90 W	82	GP 32, 0.75 - 6.0 Nm	239/240			●
RE 35, 90 W	82	GP 32, 8 Nm	242			●
RE 35, 90 W	82	GP 42, 3.0 - 15 Nm	244			●
RE 35, 90 W	82			AB 28	308	124.1
RE 35, 90 W	82	GP 32, 0.75 - 6.0 Nm	239/240	AB 28	308	●
RE 35, 90 W	82	GP 42, 3.0 - 15 Nm	244	AB 28	308	●
RE 36, 70 W	83					92.2
RE 36, 70 W	83	GP 32, 0.4 - 2.0 Nm	237			●
RE 36, 70 W	83	GP 32, 0.75 - 6.0 Nm	239/240			●
RE 36, 70 W	83	GP 42, 3.0 - 15 Nm	244			●
RE 40, 150 W	84					91.7
RE 40, 150 W	84	GP 42, 3.0 - 15 Nm	244			●
RE 40, 150 W	84	GP 52, 4.0 - 30 Nm	247			●
RE 40, 150 W	84			AB 28	308	124.2
RE 40, 150 W	84	GP 42, 3.0 - 15 Nm	244	AB 28	308	●
RE 40, 150 W	84	GP 52, 4.0 - 30 Nm	247	AB 28	308	●

Technical Data

Supply voltage	5 V ± 10 %
Output signal	TTL compatible
Phase shift F (nominal)	90°e ± 45°e
Signal rise time (typical at C_L = 25 pF, R_L = 2.7 kΩ, 25°C)	180 ns
Signal fall time (typical at C_L = 25 pF, R_L = 2.7 kΩ, 25°C)	40 ns
Index pulse width (nominal)	90°e
Operating temperature range	-40 ... +100°C
Moment of inertia of code wheel	≤ 0.6 gcm²
Max. angular acceleration	250 000 rad s⁻²
Output current per channel	min. -1 mA, max. 5 mA

Pin Allocation

Encoder	Description	Pin no. from 3409.506
Pin 5	Channel B	1
Pin 4	V_{CC}	2
Pin 3	Channel A	3
Pin 2	Channel I	4
Pin 1	GND	5

Cable with plug:
maxon Art. No. 3409.506
The plug (Harting 09185066803) can be fixed in the required position.

600×12

Cable with plug: (compatible with Encoder HEDS5010)
maxon Art. No. 3409.504
The plug (3M 89110-0101) can be fixed in the required position.

40±5   600×12

Connection example

Ambient temperature range δ_U = 25°C

May 2008 edition / subject to change

Slave Motor Gearhead

maxon gear

Planetary Gearhead GP 32 C ⌀32 mm, 1.0 - 6.0 Nm
Ceramic Version

M 1:2

Option: Low-noise version

Technical Data

Planetary Gearhead	straight teeth
Output shaft	stainless steel
Shaft diameter as option	8 mm
Bearing at output	ball bearing
Radial play, 5 mm from flange	max. 0.14 mm
Axial play	max. 0.4 mm
Max. radial load, 10 mm from flange	140 N
Max. permissible axial load	120 N
Max. permissible force for press fits	120 N
Sense of rotation, drive to output	=
Recommended input speed	< 8000 rpm
Recommended temperature range	-20 ... +100°C
Extended area as option	-35 ... +100°C

■ Stock program
□ Standard program
▨ Special program (on request)

Gearhead Data

| Order Number			166930	166933	166938	166939	**166944**	**166949**	166954	166959	**166962**	**166967**	166972	166977
1 Reduction			3.7 : 1	14 : 1	33 : 1	51 : 1	111 : 1	246 : 1	492 : 1	762 : 1	1181 : 1	1972 : 1	2829 : 1	4380 : 1
2 Reduction absolute			26/7	676/49	529/16	17576/343	13824/125	421824/1715	86112/175	19044/25	10123776/8575	8626176/4375	495144/175	109503/25
3 Max. motor shaft diameter		mm	6	6	3	6	4	4	4	3	4	4	3	3
Order Number			**166931**	**166934**		**166940**	166945	166950	**166955**	166960	166963	166968	166973	166978
1 Reduction			4.8 : 1	18 : 1		66 : 1	123 : 1	295 : 1	531 : 1	913 : 1	1414 : 1	2189 : 1	3052 : 1	5247 : 1
2 Reduction absolute			24/5	624/35		16224/245	6877/56	101062/343	331776/625	36501/40	2425488/1715	536406/245	1907712/625	839523/160
3 Max. motor shaft diameter		mm	4	4		4	3	3	4	3	3	3	3	3
Order Number			166932	166935		166941	166946	**166951**	166956	166961	**166964**	166969	166974	166979
1 Reduction			5.8 : 1	21 : 1		79 : 1	132 : 1	318 : 1	589 : 1	1093 : 1	1526 : 1	2362 : 1	3389 : 1	6285 : 1
2 Reduction absolute			23/4	299/14		3887/49	3312/25	389376/1225	20631/35	279841/256	9345024/6125	2066688/875	474513/140	6436343/1024
3 Max. motor shaft diameter		mm	3	3		3	3	4	3	4	3	3	3	3
Order Number				166936		166942	166947	**166952**	166957			166965	**166970**	166975
1 Reduction				23 : 1		86 : 1	159 : 1	411 : 1	636 : 1			1694 : 1	2548 : 1	3656 : 1
2 Reduction absolute				576/25		14976/175	1587/10	359424/875	79488/125			1162213/686	7962624/3125	457056/125
3 Max. motor shaft diameter		mm		4		4	3	4	3			3	4	3
Order Number				166937		166943	166948	166953	166958			166966	166971	166976
1 Reduction				28 : 1		103 : 1	190 : 1	456 : 1	706 : 1			1828 : 1	2623 : 1	4060 : 1
2 Reduction absolute				138/5		3588/35	12167/64	89401/196	158171/224			2238912/1225	2056223/784	3637933/896
3 Max. motor shaft diameter		mm		3		3	3	3	3			3	3	3
4 Number of stages			1	2	2	3	3	4	4	4	5	5	5	5
5 Max. continuous torque		Nm	1	3	3	6	6	6	6	6	6	6	6	6
6 Intermittently permissible torque at gear output		Nm	1.25	3.75	3.75	7.5	7.5	7.5	7.5	7.5	7.5	7.5	7.5	7.5
7 Max. efficiency		%	80	75	75	70	70	60	60	60	50	50	50	50
8 Weight		g	118	162	162	194	194	226	226	226	258	258	258	258
9 Average backlash no load		°	0.7	0.8	0.8	1.0	1.0	1.0	1.0	1.0	1.0	1.0	1.0	1.0
10 Mass inertia		gcm²	1.5	0.8	0.8	0.7	0.7	0.7	0.7	0.7	0.7	0.7	0.7	0.7
11 Gearhead length L1		mm	26.4	36.3	36.3	43.0	43.0	49.7	49.7	49.7	56.4	56.4	56.4	56.4

overall length   overall length
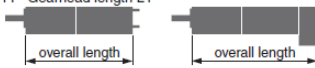
Combination

+ Motor	Page	+ Tacho / Brake	Page	Overall length [mm] = Motor length + gearhead length + (tacho / brake) + assembly parts										
RE 25, 10 W	77			81.0	90.9	90.9	97.6	97.6	104.3	104.3	104.3	111.0	111.0	111.0	111.0
RE 25, 10 W	77	MR	258	92.0	101.9	101.9	108.6	108.6	115.3	115.3	115.3	122.0	122.0	122.0	122.0
RE 25, 10 W	77	Enc 22	260	95.1	105.0	105.0	111.7	111.7	118.4	118.4	118.4	125.1	125.1	125.1	125.1
RE 25, 10 W	77	HED_ 5540	262/264	101.8	111.7	111.7	118.4	118.4	125.1	125.1	125.1	131.8	131.8	131.8	131.8
RE 25, 10 W	77	DCT 22	271	103.3	113.2	113.2	119.9	119.9	126.6	126.6	126.6	133.3	133.3	133.3	133.3
RE 25, 20 W	78			69.5	79.4	79.4	86.1	86.1	92.8	92.8	92.8	99.5	99.5	99.5	99.5
RE 25, 20 W	79			81.0	90.9	90.9	97.6	97.6	104.3	104.3	104.3	111.0	111.0	111.0	111.0
RE 25, 20 W	79	MR	258	92.0	101.9	101.9	108.6	108.6	115.3	115.3	115.3	122.0	122.0	122.0	122.0
RE 25, 20 W	79	Enc 22	260	95.1	105.0	105.0	111.7	111.7	118.4	118.4	118.4	125.1	125.1	125.1	125.1
RE 25, 20 W	79	HED_ 5540	262/264	101.8	111.7	111.7	118.4	118.4	125.1	125.1	125.1	131.8	131.8	131.8	131.8
RE 25, 20 W	79	DCT 22	271	103.3	113.2	113.2	119.9	119.9	126.6	126.6	126.6	133.3	133.3	133.3	133.3
RE 25, 20 W	79	HED_5540 / AB 28	308	132.2	142.1	142.1	148.8	148.8	155.5	155.5	155.5	162.2	162.2	162.2	162.2
RE 26, 18 W	80			85.3	95.2	95.2	101.9	101.9	108.6	108.6	108.6	115.3	115.3	115.3	115.3
RE 26, 18 W	80	MR	258	96.3	106.2	106.2	112.9	112.9	119.6	119.6	119.6	126.3	126.3	126.3	126.3
RE 26, 18 W	80	Enc 22	260	102.7	112.6	112.6	119.3	119.3	126.0	126.0	126.0	132.7	132.7	132.7	132.7
RE 26, 18 W	80	HED_ 5540	262/264	103.7	113.6	113.6	120.3	120.3	127.0	127.0	127.0	133.7	133.7	133.7	133.7
RE 26, 18 W	80	DCT 22	271	106.3	116.2	116.2	122.9	122.9	129.6	129.6	129.6	136.3	136.3	136.3	136.3
RE 30, 60 W	81			94.5	104.4	104.4	111.1	111.1	117.8	117.8	117.8	124.5	124.5	124.5	124.5
RE 30, 60 W	81	MR	259	105.9	115.8	115.8	122.5	122.5	129.2	129.2	129.2	135.9	135.9	135.9	135.9
RE 35, 90 W	82			97.4	107.3	107.3	114.0	114.0	120.7	120.7	120.7	127.4	127.4	127.4	127.4
RE 35, 90 W	82	MR	259	108.8	118.7	118.7	125.4	125.4	132.1	132.1	132.1	138.8	138.8	138.8	138.8
RE 35, 90 W	82	HED_ 5540	262/264	118.4	128.3	128.3	135.0	135.0	141.7	141.7	141.7	148.4	148.4	148.4	148.4
RE 35, 90 W	82	DCT 22	271	115.5	125.4	125.4	132.1	132.1	138.8	138.8	138.8	145.5	145.5	145.5	145.5
RE 35, 90 W	82	AB 28	308	133.5	143.4	143.4	150.1	150.1	156.8	156.8	156.8	163.5	163.5	163.5	163.5
RE 35, 90 W	82	HEDS 5540 / AB 28	262/308	150.6	160.5	160.5	167.2	167.2	173.9	173.9	173.9	180.6	180.6	180.6	180.6
RE 36, 70 W	83			97.7	107.6	107.6	114.3	114.3	121.0	121.0	121.0	127.7	127.7	127.7	127.7
RE 36, 70 W	83	MR	259	109.1	119.0	119.0	125.7	125.7	132.4	132.4	132.4	139.1	139.1	139.1	139.1
RE 36, 70 W	83	HED_ 5540	262/264	118.7	128.6	128.6	135.3	135.3	142.0	142.0	142.0	148.7	148.7	148.7	148.7
RE 36, 70 W	83	DCT 22	271	115.8	125.7	125.7	132.4	132.4	139.1	139.1	139.1	145.8	145.8	145.8	145.8

May 2008 edition / subject to change

Slave Motor Driver

ADVANCED MOTION CONTROLS

Analog Servo Drive

AZBDC10A4

Description

The AZBDC10A4 PWM servo drive is designed to drive brushless and brushed DC motors at a high switching frequency. To increase system reliability and to reduce cabling costs, the drive is designed for direct integration into your PCB. The AZBDC10A4 is fully protected against over-voltage, under-voltage, over-current, over-heating, and short-circuits. A single digital output indicates operating status. The drive interfaces with digital controllers that have digital PWM output. The PWM IN duty cycle determines the output current and DIR input determines the direction of rotation. This servo drive requires only a single unregulated isolated DC power supply, and is fully RoHS (Reduction of Hazardous Substances) compliant.

See Part Numbering Information on last page of datasheet for additional ordering options.

Power Range

Peak Current	10 A
Continuous Current	5 A
Supply Voltage	10 - 36 VDC

Features

- Four Quadrant Regenerative Operation
- Direct Board-to-Board Integration
- Lightweight
- High Switching Frequency
- Wide Temperature Range
- Differential Input Command

- Digital Fault Output Monitor
- Current Monitor Output
- Single Supply Operation
- Compact Size
- High Power Density
- 12VDC Operation

HARDWARE PROTECTION
- Over-Voltage
- Under-Voltage
- Over-Current
- Over-Temperature
- Short-circuit (phase-phase)
- Short-circuit (phase-ground)

INPUTS/OUTPUTS
- Digital Fault Output
- Digital Inhibit Input
- Analog Current Monitor
- Analog Command Input

FEEDBACK SUPPORTED
- Hall Sensors

MODES OF OPERATION
- Current

COMMUTATION
- Trapezoidal

MOTORS SUPPORTED
- Three Phase (Brushless)
- Single Phase (Brushed, Voice Coil, Inductive Load)

COMMAND SOURCE
- PWM

COMPLIANCES & AGENCY APPROVALS
- RoHS
- UL/cUL Pending
- CE Pending

SPECIFICATIONS

Power Specifications		
Description	Units	Value
DC Supply Voltage Range	VDC	10 - 36
DC Bus Under Voltage Limit	VDC	8
DC Bus Over Voltage Limit	VDC	40
Maximum Peak Output Current[1]	A	10
Maximum Continuous Output Current	A	5
Maximum Continuous Output Power	W	171
Maximum Power Dissipation at Continuous Current	W	9
Minimum Load Inductance (Line-To-Line)[2]	µH	100
Internal Bus Capacitance[3]	µF	23.5
Low Voltage Supply Outputs	-	+5 VDC (30 mA)
Switching Frequency	kHz	40

Control Specifications		
Description	Units	Value
Command Sources	-	PWM
PWM Input Frequency Range	-	10 - 25
Feedback Supported	-	Halls
Commutation Methods	-	Trapezoidal
Modes of Operation	-	Current
Motors Supported	-	Three Phase (Brushless), Single Phase (Brushed, Voice Coil, Inductive Load)
Hardware Protection	-	Invalid Commutation Feedback, Over Current, Over Temperature, Over Voltage, Under Voltage, Short Circuit (Phase-Phase & Phase-Ground)

Mechanical Specifications		
Description	Units	Value
Agency Approvals	-	RoHS, UL/cUL Pending, CE Pending
Size (H x W x D)	mm (in)	38.1 x 38.1 x 7.34 (1.50 x 1.50 x 0.29)
Weight	g (oz)	8.5 (0.3)
Operating Temperature Range[4]	°C (°F)	0 - 85 (32 - 185)
Storage Temperature Range	°C (°F)	-40 - 85 (-40 - 185)
Relative Humidity	-	0 - 90% Non-Condensing
Form Factor	-	PCB Mounted
P1 Connector	-	12-pin, 1.27 mm spaced header
P2 Connector	-	12-pin, 1.27 mm spaced header

Notes

1. Maximum duration of peak current is ~2 seconds. Peak RMS value must not exceed continuous current rating of the drive.
2. Lower inductance is acceptable for bus voltages well below maximum. Use external inductance to meet requirements.
3. Requires a minimum of 47 µF external bus capacitance between the DC Supply and Power Ground.
4. Additional cooling and/or heatsink may be required to achieve rated performance.

Release Date: Status: ADVANCED Motion Controls · 3805 Calle Tecate, Camarillo, CA, 93012   Page 3 of 7
4/10/2015   Active   ph# 805-389-1935 · fx# 805-389-1165· www.a-m-c.com

116/117

PIN FUNCTIONS

P1 - Signal Connector

Pin	Name	Description / Notes	I/O
1	DIRECTION	Direction Input (+5V)	I
2	PWM / IN	10 – 25 kHz pulse width modulated digital input command (+5V). Input duty cycle commands the output current.	I
3	SIGNAL GND	Signal Ground (Common With Power Ground).	GND
4	FAULT OUT	TTL level (+5 V) output becomes high when power devices are disabled due to at least one of the following conditions: inhibit, invalid Hall state, output short circuit, over voltage, over temperature, power-up reset.	O
5	INHIBIT IN	TTL level (+5 V) inhibit/enable input. Leave open to enable drive. Pull to ground to inhibit drive. Inhibit turns off all power devices.	I
6	CURRENT MONITOR	Current Monitor. Analog output signal proportional to the actual current output. Scaling is 2 A/V. Measure relative to signal ground.	O
7	HALL 3		I
8	HALL 2*	Single-ended Hall/Commutation Sensor Inputs (+5 V logic level)	I
9	HALL 1		I
10	+V HALL OUT	Low Power Supply For Hall Sensors (+5 V @ 30 mA). Referenced to signal ground. Short circuit protected.	O
11	SIGNAL GND	Signal Ground (Common With Power Ground).	GND
12	RESERVED	Reserved	-

P2 - Power Connector

Pin	Name	Description / Notes	I/O
1	MOTOR A		O
2	MOTOR A		O
3	MOTOR B	Motor Phase Outputs. Current output distributed equally across 2 pins per motor phase, 3A continuous current carrying capacity per pin.	O
4	MOTOR B		O
5	MOTOR C		O
6	MOTOR C		O
7	NC (KEY)	No Connection. Keyed pin.	-
8	PWR GND	Power Ground (Common With Signal Ground). 3A Continuous Current Rating Per Pin	GND
9	PWR GND		GND
10	HV IN	DC Power Input. 3A Continuous Current Rating Per Pin. Requires a minimum of 47 µF external capacitance between HV IN and PWR GND pins.	I
11	HV IN		I
12	RESERVED	Reserved	-

*For use with Single Phase (Brushed) motors, ground Hall 2 and only connect motor leads to Motor A and Motor B.

Note: P1 and P2 are identical 12-pin headers. To avoid damage to the drive, be sure when plugging or soldering the drive into a PCB or interface card that the drive orientation is correct. P1 and P2 are labeled on the PCB silkscreen. Pin 7 on P2 is keyed to differentiate it from P1. Consult the mounting dimension drawing on page 6 of this datasheet for an illustration of the locations of P1 and P2.

HARDWARE SETTINGS

Jumper Settings

Jumpers are SMT, 0 ohm resistors located on the underside of the drive PCB. By default, the drive is configured with the jumpers installed. Typical drive operation will not require the jumpers to be removed. Please contact the factory before jumper removal.

Jumper	Description SMT Jumper (0Ω Resistor)	Configuration	
		Not Installed	Installed
JE1	Inhibit logic. Sets the logic level of inhibit pins. Labeled JE1 on the PCB of the drive.	Low Enable	Low Inhibit
JE2	Hall sensor phasing. Selects 120 or 60 degree commutation phasing. Labeled JE2 on the PCB of the drive.	60 degree	120 degree